**Experiment 817**
**$\beta$-NMR investigation of type-II superconductors**
*(Z. Salman, Oxford; D. Wang, R.F. Kiefl, UBC)*

One of the most remarkable properties of a superconductor is the vortex lattice, which is formed in the presence of an applied magnetic field. Much has been learned about vortices and the vortex lattice since it was first predicted by Abrikosov in 1957. Nevertheless, vortices are complex objects with properties that are still not fully understood. In recent years muon spin rotation ($\mu$SR) has been used extensively to measure the magnetic field distribution in the vortex state, which is a sensitive probe of vortex structure and the vortex lattice. For example $\mu$SR results in $NbSe_2$ have shown that the vortex core shrinks due to depopulation of the core bound states but the low temperature core radius is still significantly larger than predicted in the quantum limit. Recently there has been considerable work on the role of delocalized quasiparticles associated with the cores and the interaction between vortices, particularly in multiband superconductors such as $NbSe_2$, where there is more than one superconducting gap.

In this experiment we are investigating the vortex state of $NbSe_2$ ($T_c$ = 7.0 K) and other superconductors using depth resolved $\beta$-detected NMR of $^8$Li. While $\mu$SR is primarily a bulk probe, $\beta$-NMR can be used to investigate the vortex lattice much closer to the surface, i.e. on the scale of the vortex lattice spacing $a_0 = 1546/\sqrt{B_{ext}[mT]}$ nm. In general, we expect vortices and vortex interactions to be different near a surface or interface due the discontinuous nature of the superconductor.

Figure 1a shows the $\beta$-NMR spectrum in the normal state of $NbSe_2$ in a magnetic field of 300 mT applied along the $c$-axis. Above $T_c$ the lineshape is nearly independent of magnetic field, temperature and implantation depth. After field-cooling below $T_c$, the resonance broadens asymmetrically (Fig. 1b) and exhibits all the characteristic features of a triangular vortex lattice. In particular, note the most probable frequency, or cusp frequency, shifts by an amount $\Delta_c$ below the normal state frequency. The cusp frequency (or magnetic field) arises from Li located midway between two adjacent vortices. In addition, there is also a high frequency tail which corresponds to the magnetic field distribution near the vortex core. The high frequency cutoff, which is shifted by an amount $\Delta_v$ above the normal state frequency, corresponds to the field at the vortex core. The curve in Fig. 1b is a fit to the vortex lineshape model taking into account the close proximity to the surface. The best fit gives a London penetration depth $\lambda = 230(30)$ nm and a vortex core radius $\rho = 13(1)$ nm. These parameters are close to what is observed from $\mu$SR in the bulk $NbSe_2$ at the same temperature and field, indicating at this field the vortex lattice is similar to that deeper inside the sample.

Figure 2 shows the $\beta$-NMR lineshape in a much lower magnetic field of 10.8 mT. Note the line is slightly narrower in Fig. 2b compared to 2c. This is predicted in a simple model of vortices near a surface. The most surprising result is the remarkable similarity of lineshapes in Figs. 1 and 2, given the magnetic fields differ by a factor of 27. In particular, in Fig. 2, note the observed cutoff at a frequency $\Delta_v$ above the normal state frequency, corresponding to the frequency at the vortex. The small value of $\Delta_v$ in Figs. 2b and 2c can only be explained by a very extended vortex. The curves are a fit to the vortex lineshape model assuming a depth independent $\lambda$ nm and $\rho$ nm. The best fit is with $\lambda$ = 167(15) nm and $\rho$ = 77(10) nm. Thus the core size at this field is much larger than the coherence length and what is measured in high field. A plausible explanation is that in a lower field the vortices are further apart and thus interact more weakly. This would lead to enhanced thermal vibrations in low field. It is likely that multiband effects also contribute to the giant vortices we observe in $NbSe_2$. These results point to the need for a comprehensive theory of the vortices and their interactions, which includes both electronic and vibrational excitations.

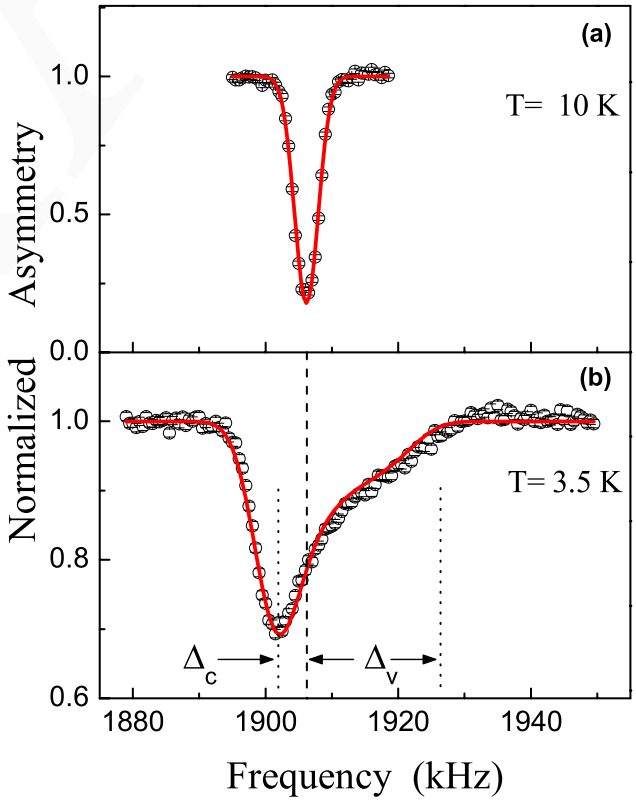

Fig. 1. (a) The $\beta$-NMR spectrum in the normal state of $NbSe_2$ at 10 K in a magnetic field of 300 mT applied along the $c$-axis. The beam energy of 20 keV corresponds to a mean implantation depth $\langle z \rangle = 85$ nm. The observed Gaussian line broadening is attributed to $^{93}$Nb nuclear moments. (b) The same conditions as (a) except field cooled to 3.5 K or 0.5 $T_c$. The asymmetric lineshape is characteristic of a triangular lattice of magnetic vortices.

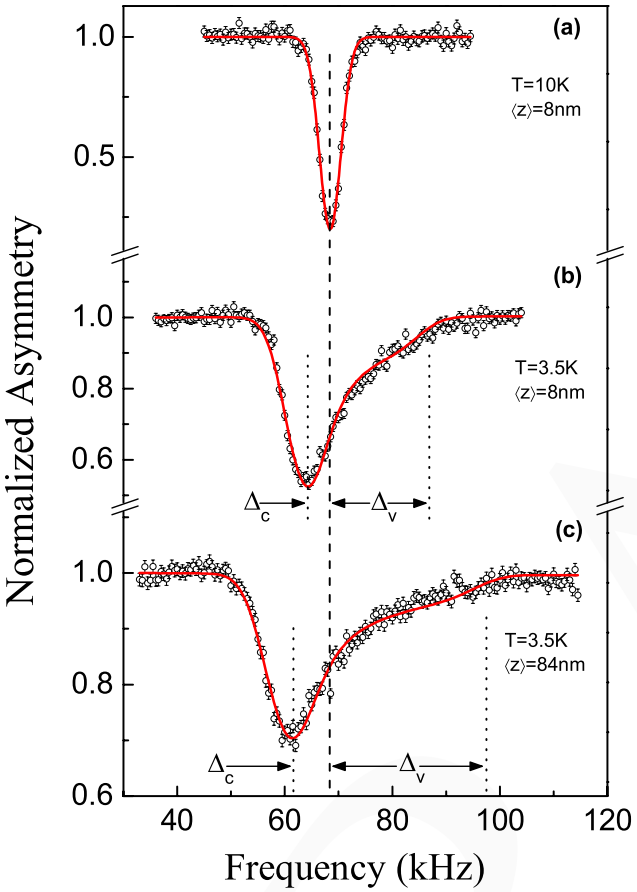


Fig. 2 $\beta$-NMR resonances in $NbSe_2$ in a low magnetic field of 10.8 mT. (a) In the normal state at 10 K with a beam energy corresponding to a mean implantation depth $\langle z \rangle = 8$ nm. (b) The same conditions as (a) except field cooled to 0.5 $T_c$. (c) The same temperature and magnetic field as (b) but the mean implantation depth is about 10 times larger.

**Experiment 891**
**Superconductivity and magnetism in $Ce_nT_mIn_{3n+2m}$**
*(K. Ohishi, R.H. Heffner, JAEA-ASRC)*

Heavy fermion compounds possess a characteristic temperature $T^*$ signifying a crossover from localized behaviour at high temperatures to coherent behaviour at low temperatures. This behaviour is explained as the onset of coherent conduction electron scattering by the Kondo lattice of $f$ spins; at high temperatures the $f$ electrons scatter the conduction electrons independently as local impurities.

It is observed that heavy-fermion Knight shift anomalies, which are a deviation from a linear relation between the shift $K$ and the magnetic susceptibility $\chi$, occur at low temperatures. Such behaviour is attributed to local phenomena associated with the $f$ electrons. Quite generally, $K = A\chi/(N_A\mu_B)$, where $A$ is the hyperfine coupling, $N_A$ is Avogadro's number and $\mu_B$ is the Bohr magneton. One cause of such an anomaly is low-lying crystal field levels, where the hyperfine coupling $A$ changes as the $4f$ electron states become depopulated from the excited states of the crystal-field split multiplets [Ohama *et al.*, J. Phys. Soc. Jpn. **64**, 2628 (1995)]. In another scenario, the local susceptibility rather than the hyperfine coupling changes. Here the susceptibility can be decomposed into a high-temperature component $\chi_{ff}$, corresponding to non-interacting local moments, and a low-temperature component $\chi_{cf}$, which is characteristic of the coherent state below $T^*$ [Nakatsuji *et al.*, Phys. Rev. Lett. **92**, 016401 (2004); Curro *et al.*, Phys. Rev. **B70**, 235117 (2004)]. Curro *et al.* reported that this heavy-electron component scales universally as $\chi_{cf} \propto (1 - T/T^*)\ln(T^*/T)$ for some Ce, Yb and U based materials. Note that a Knight shift anomaly caused by crystal fields is not expected to display such a temperature dependence. In a previous muon Knight shift study of $Ce_2IrIn_8$ [Heffner *et al.*, Physica **B374-375**, 184 (2006)], a deviation from the linear behaviour of $K$ versus $\chi$ was observed below $T^* = 24(1)$ K for applied field $H_0 \parallel c$-axis, and $\chi_{cf}$ proportional to $(1 - T/T^*)\ln(T^*/T)$ below $T^*$ was extracted.

In order to elucidate the effects of Ce dilution on the heavy electron state in $Ce_2IrIn_8$, we have performed muon Knight shift measurements in single crystalline samples of $(Ce_{1-x}La_x)_2IrIn_8$ ($x = 0.1, 0.25, 0.5, 0.7$ and 0.9). Here we report the data for $x = 0.1$.

In the present experiments we used single crystalline samples grown by the In-flux method at Los Alamos National Laboratory [Macaluso *et al.*, Chem. Mater. **15**, 1394 (2003)]. Transverse-field (TF-) $\mu$SR experiments were performed at the M20 beam line. The external field was applied along the $c$-axis of the crystals and parallel to the beam direction. The crystals were mounted on a silver sheet, which served as a reference material to calibrate the applied field. The signals which came from muons stopping in the sample and the silver were separated electronically and accumulated individually.

The observed muon Knight shift is defined as follows: $K_{exp} = \frac{f_i - f_0}{f_0} = K_\mu + K_{dem}$, where $f_i$ is the measured precession frequency of the $i$-th signal component, and $f_0 = \gamma_\mu H_0/2\pi$ is the muon frequency in the external field $H_0$, with $\gamma_\mu$ as the muon gyromagnetic ratio ($= 2\pi \times 135.54$ MHz/T). $K_{dem} =$

$4\pi(1/3-N)\rho_{\rm mol}\chi$ is the contribution from the Lorentz and demagnetization terms, where $N \sim 1$ is the demagnetization factor in this experiment and $\rho_{\rm mol}$ is the molar density.

According to the report of Curro *et al.* [*op. cit.*], the uniform susceptibility is written as $\chi(T) = \chi_{\rm ff}(T) + 2\chi_{\rm cf}(T) + \chi_0$, where $\chi_0$ is a temperature-independent component. The muon Knight shift from the $i$-th frequency component $K_{\mu i}$, including the contribution from $\chi_{\rm cf}$, is summarized as follows:

$$\begin{aligned} K_{\mu i} &= K^i_{\rm exp} - K_{\rm dem} \\ &= K^i_o + \frac{(A^i_{\rm cf} - A^i_{\rm hyp})\chi_{\rm cf} + A^i_{\rm hyp}(\chi - \chi_0)}{N_{\rm A}\mu_{\rm B}}, \end{aligned}$$

where $A^i_{\rm cf}$ and $A^i_{\rm hyp}$ are the couplings between the muon and $\chi_{\rm cf}$ and $\chi_{\rm ff}$, respectively, and $K^i_o$ is a temperature-independent shift.

Figure 1 shows the fast Fourier transform spectrum of $\mu$SR signals at 20 K. The dashed line shows the $K = 0$ frequency. Clearly, four frequencies are observed in the La-doped sample, i.e., La doping induces a splitting of the lines, likely due to muons stopping in a local environment either rich in Ce atoms ($K_{\mu 1}$) or depleted in Ce atoms ($K_{\mu 1'}$). Here we focus on the lowest frequency peak $K_{\mu 1}$.

The shift $K_{\mu 1}$ is shown versus the bulk susceptibility $\chi$ in Fig. 2; for comparison, the shift of the unsplit line in $Ce_2IrIn_8$ is also shown. We find that the shifts scale with $\chi$ below $\chi \sim 0.014$ emu/mol-Ce. A clear deviation from linear behaviour is also observed for $\chi > 0.014$ emu/mol-Ce. The $A_{\rm hyp}$ value from the high-temperature fits to the data (where $T > T^*$ and, hence, $\chi_{\rm cf} = 0$) is –805(9) Oe/$\mu_{\rm B}$. As seen in Fig. 2, the values of $A_{\rm hyp}$ for $K_{\mu 1}$ in both samples are almost the same.

Using the derived values of $A_{\rm hyp}$ and $\chi$, the term containing $\chi_{\rm cf}(T)$ in the above equation was obtained. Figure 3 shows that these data are well described by

$$K^i_{\rm cf} = K^{i0}_{\rm cf}\left(1 - \frac{T}{T^*}\right)\ln\left(\frac{T^*}{T}\right),$$

where $K_{\rm cf} = K^0_{\rm cf}$ for $T/T^* = 0.259$. The solid line in Fig. 3 is the fitting result using this equation with parameter $T^* = 20.1(8)$ K. It is obvious that the $K_{\rm cf}$ scales with the universal relationship $\propto (1 - T/T^*)\ln(T^*/T)$, even in the La-doped sample. The reduction of $T^*$ indicates that the intersite interaction between $4f$ electrons becomes weaker in the La-doped system. The analysis of the samples with $x > 0.1$ is under way.

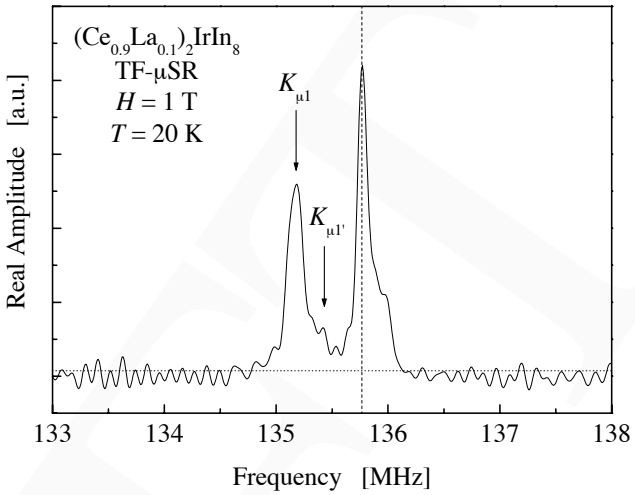


Fig. 1. The fast Fourier transform spectra of $\mu$SR signals at 20 K. The dashed line shows the $K = 0$ frequency.

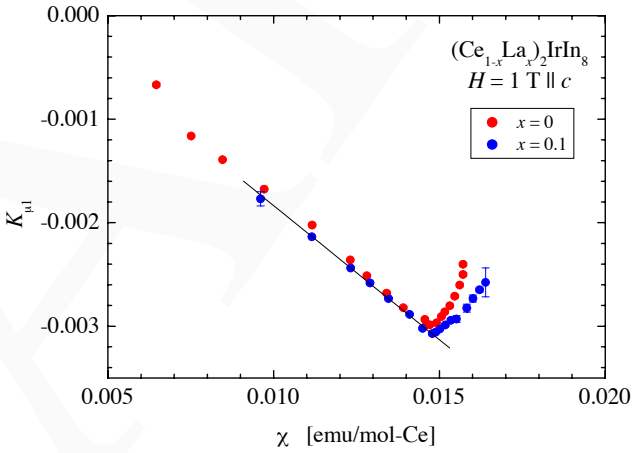


Fig. 2. Knight shift $K_{\mu 1}$ vs. susceptibility $\chi$ plots in $(Ce_{0.9}La_{0.1})_2IrIn_8$. Knight shift in $Ce_2IrIn_8$ [Heffner *et al.*, *op. cit.*] is also plotted for comparison.

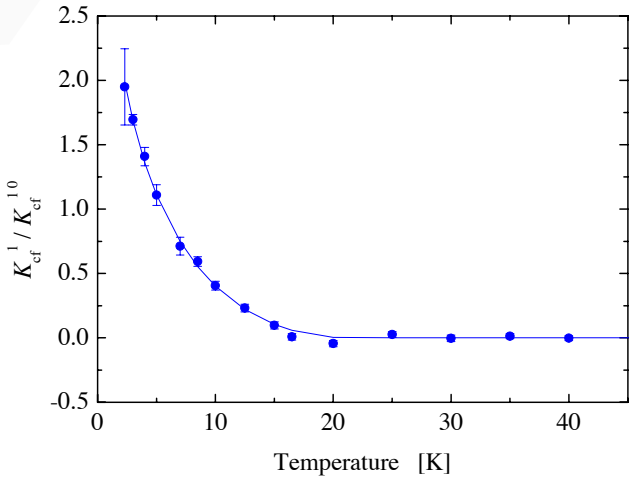


Fig. 3. Temperature dependence of the normalized Knight shift $K^1_{\rm cf}/K^{10}_{\rm cf}$ in $(Ce_{0.9}La_{0.1})_2IrIn_8$. The solid line is a fit to the equation with parameter $T^* = 20.1(8)$ K.

**Experiment 895**
**The vortex structure and magnetism of electron-doped cuprate superconductors**
*(K.H. Satoh, Graduate Univ. for Advanced Studies; R. Kadono, KEK-IMSS)*

The question whether or not the mechanism of superconductivity in electron-doped ($n$-type) cuprates is common to that in hole-doped ($p$-type) cuprates is one of the most interesting issues in the field of cuprate superconductors, which is yet to be answered. Unfortunately, the study of flux line lattice (FLL) state in $n$-type cuprates such as T′-phase $RE_2CuO_4$ compounds ($RE$ = Nd, Pr, Sm, etc.) is far behind that in $p$-type cuprates because of strong random local fields from rare-earth ions which mask information from $CuO_2$ planes for magnetic probes such as muon. In this regard, infinite-layer structured $Sr_{1-x}La_xCuO_2$ (SLCO) is a suitable compound for detailed $\mu$SR study of electron-doped systems, as it is free from magnetic rare-earth ions.

In 2005 and 2006, we made $\mu$SR measurements under zero/longitudinal field (ZF/LF) and a high transverse field (HTF) on SLCO with $x$ = 0.1, 0.125, and 0.15 using the HiTime spectrometer. Here we report a preliminary result on the sample with $x$ = 0.125. The SLCO sample was prepared with the high-pressure technique using a cubic anvil press, and the obtained polycrystalline sample was confirmed to exhibit superconductivity below 42 K by magnetic susceptibility measurement. Figure 1 shows fast Fourier transform (FFT) of some HTF-$\mu$SR spectra under 60 kG. A small satellite peak (labelled as B) appears on the positive side of the central sharp peak (labelled as A), where the satellite exhibits no appreciable shift at lower temperatures. With decreasing temperature, the linewidth of the satellite peak becomes broader, and its volume fraction increases to nearly 50% at 50 K. The appearance of the satellite peak in the normal state clearly indicates occurrence of a phase separation irrespective of superconductivity. It is inferred from ZF/LF-$\mu$SR measurements that the corresponding magnetic phase is spin glass-like and quasi-static in the $\mu$SR time window.

Taking this result into consideration, we deduced the magnetic penetration depth $\lambda$ from the $\mu$SR spectra below $T_c$ using the modified London model. In the London model, $B(r)$ is approximated as the sum of magnetic inductions from isolated vortices to yield

$$B(r) = B_0 \sum \frac{e^{-iK\cdot r}}{1+K^2\lambda^2} F(K,\xi_V)$$

$$F(K,\xi_V) = e^{-(K^2\xi_V^2)/2}$$

where $K$ are the vortex reciprocal lattice vectors, $B_0 (\simeq H)$ is the average internal field, $\lambda$ is the *effective* London penetration depth, and $F(K,\xi_v)$ is a non-local correction term with $\xi_v$ being the cut-off parameter for the magnetic field distribution; the Gaussian cut-off generally provides satisfactory agreement with data. As a result, $\lambda$ for SLCO($x$ = 0.125) is estimated to be ∼87 nm. This value is much shorter than that previously reported for $p$-type cuprates, where the corresponding "Gaussian linewidth" $\sigma$ vs. $T_c$ point falls far off the Uemura line. This is in line with the recent result on SLCO by A. Shengelaya *et al.* [Phys. Rev. lett. **94**, 127001 (2005)], although the occurrence of phase separation and associated magnetic phase is not considered in their data analysis.

We also found that the dimensionless parameter $\eta$, corresponding to the normalized slope of $\lambda(h)$ against an external field, is positive in this compound. This behaviour is commonly found in the materials whose superconducting order parameter has a nodal structure, and the magnitude of $\eta$ is a good measure for the degree of anisotropy in the superconducting order parameter. However, the deduced value of $\eta$ (∼1.9) is smaller than that of typical $d$-wave superconductors at lower fields, e.g., $YBa_2Cu_3O_{6.95}$ (YBCO, where $\eta \sim$ 5.6–6) [Sonier *et al.*, Phys. Rev. **B55**, 11789 (1997)]. Recently, a difference in the superconducting order parameter between $p$-type and $n$-type cuprates has been suggested by ARPES measurement [Matsui, *et al.*, Phys. Rev. Lett. **95**, 017003 (2005)]. The observed difference of $\eta$ between SLCO and YBCO might be further evidence for such difference.

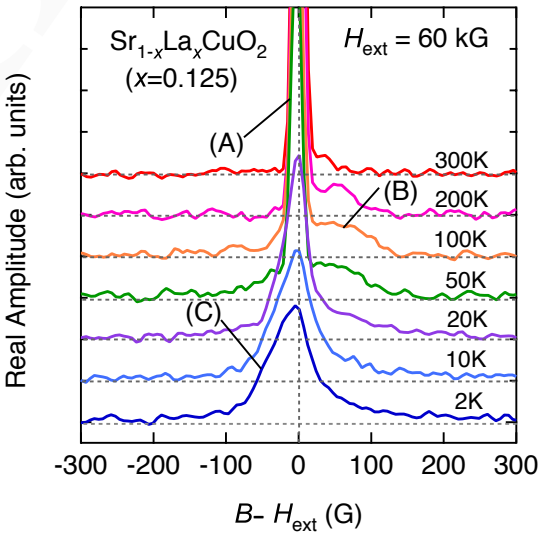


Fig. 1. Fourier transform of HTF-$\mu$SR spectra at $H_{ext}$ = 60 kG. The peaks labelled as (A), (B), and (C) correspond to non-magnetic phase, magnetic phase, and FLL phase, respectively.

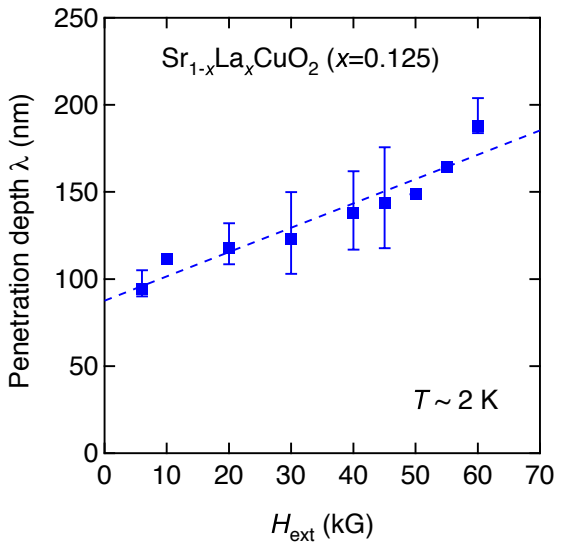


Fig. 2. Field dependence of magnetic penetration depth $\lambda$ at 2 K. Dashed line is a linear fit.

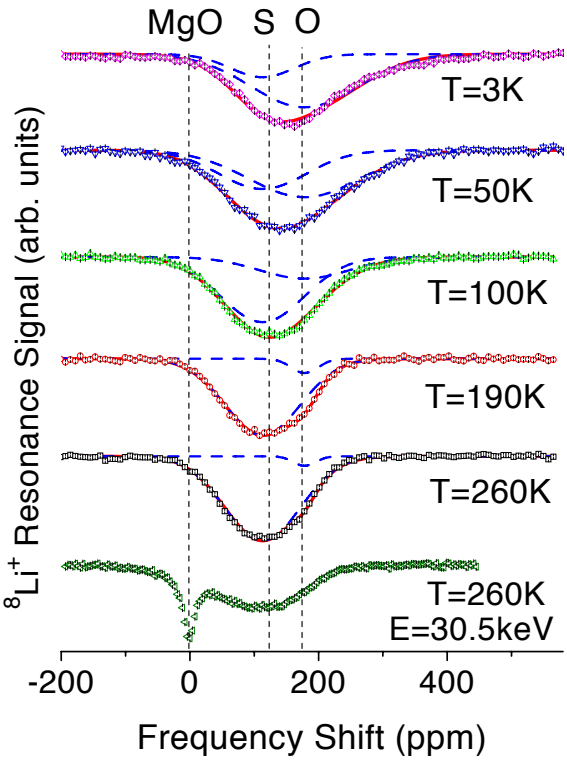


Fig. 1. Representative resonance signals of $^8$Li in the Cu/MgO sample in an applied field of 4.1 T. Each spectrum was obtained at an implantation energy of 10.6 keV, except the bottommost one, which was obtained at the full implantation energy of 30.6 keV. The three vertical dashed lines indicate the peak frequencies of the MgO, *S* and *O* signals. The zero shift in frequency is taken to be that in MgO at room temperature. The long-dashed lines indicate the *S* and *O* contributions of the signal at each temperature.

**Experiment 913**
**Photo-induced dynamics and reactivity of spin polarized $^8$Li in semiconductors**
*A. Mansour, K.H. Chow (Alberta); Z. Salman (Oxford)*

In order to understand the dynamics and reactivity of spin-polarized $^8$Li in semiconductors, it is important to be able to establish the microscopic site of the probe. In order to accomplish this goal, we recently initiated studies in a prototypical metal, the face centred cubic copper to learn how to obtain site-sensitive information. The sample used is a 50 nm film evaporated on a MgO substrate (see Figs. 1 and 2).

In metals, there is an abundance of free electrons in the system and hence certain interactions are present that are otherwise not there in a semiconductor. Of particular interest to us is the $^8$Li Knight shift, i.e. the normalized frequency shift compared to that expected for $^8$Li in vacuum. In Cu, this quantity is shown to be different for $^8$Li located in different sites in the lattice (see Fig. 1). Note that there is a change of site starting at about 50 K from the *O* (octahedral) to the *S* (substitutional) site.

The next step is to build upon this information and develop the technique of level crossing resonance, a powerful technique for providing site-sensitive information. This method can be applied to many solid-state systems, including metals and semiconductors.

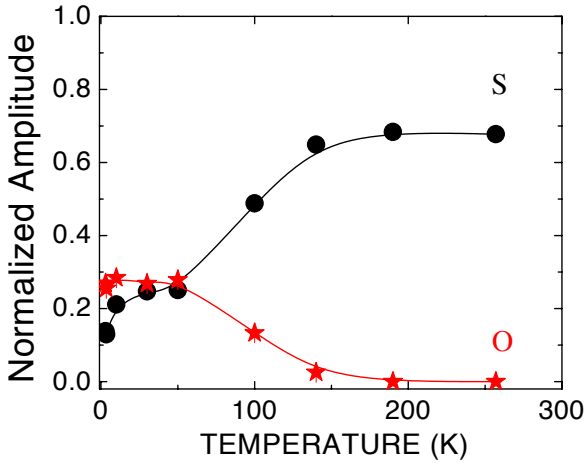


Fig. 2. Temperature dependences of the normalized amplitudes for an applied field of 4.1 T.

**Experiment 917**
**Correlation between magnetism and transport properties of thermoelectric oxides**
*(J. Sugiyama, Toyota CRDL Inc.; J.H. Brewer, UBC-TRIUMF)*

The antiferromagnetic (AF) nature of the normal spinel $Co_3O_4$ with Néel temperature ($T_N$) = 30 K [Khriplovich *et al.*, J. Chem. Thermodyn. **14**, 207 (1982)] was investigated by means of positive muon spin rotation and relaxation ($\mu^+$SR) techniques using the surface muon beam line of M20. Here, the crystal structure of $Co_3O_4$ is a cubic normal spinel with a space group $O_h^7$-$Fd\bar{3}m$, lattice constant $a = 8.084$ Å at ambient temperature [Smith *et al.*, Acta Crystallogr., Sect. B: Struct. Crystallogr. Cryst. Chem. **29**, 362 (1973)]. The charge distribution for $Co_3O_4$ is represented by $[Co^{2+}]_{8a}[Co_2^{3+}]_{16d}[O_4^{2-}]_{32e}$, in which 8a denotes the tetrahedral site and 16d the octahedral site surrounded by $O^{2-}$ ions at 32e sites. $d_{Co^{3+}-O}$ is ∼1.92 Å and $d_{Co^{2+}-O}$ ∼ 1.93 Å. The spinel $Co_3O_4$ is considered to be a cation-deficient rocksalt, that is, $O^{2-}$ ions at the 32e site and $Co^{3+}$ ions at the 16d site form an RS lattice together with the vacant 16c site, while $Co^{2+}$ ions locate at the interstitial 8a site. By comparison with the layered cobalt oxides, $Co_3O_4$ possesses a simple structure with a well-known charge distribution in the lattice.

The wTF-$\mu^+$SR spectra for $Co_3O_4$ were well fitted in the time domain using a combination of an exponentially relaxing cosine oscillation, due to the external field, and an exponentially relaxing non-oscillatory signal caused by the appearance of random internal fields in the ordered state:

$$\begin{aligned} A_0P(t) &= A_{\rm TF}\exp(-\lambda_{\rm TF}t)\cos(\omega_\mu t+\phi) \\ &\quad + A_{\rm slow}\exp(-\lambda_{\rm slow}t), \end{aligned} \tag{1}$$

where $A_0$ is the total initial asymmetry, $P(t)$ is the muon spin polarization function, $\omega_\mu$ is the muon Larmor frequency, $\phi$ is the initial phase of the muon precession and $A_n$ and $\lambda_n$ ($n$ = TF and slow) are asymmetries and relaxation rates of the two signals.

Figures 1(a) and 1(b) show the $T$ dependence of $A_n$ and $\lambda_n$ for $Co_3O_4$ below 60 K. Above 30 K, $A_{\rm TF}$ is almost constant at its maximum value (∼0.24), showing that the whole sample is paramagnetic. As $T$ decreases from 30 K, $A_{\rm TF}$ suddenly decreases and vanishes below 29 K, while $A_{\rm slow}$ appears at 30 K and seems to level off to the constant value (∼0.075) below 20 K. As $T$ decreases from 60 K, $\lambda_{\rm TF}$ is also independent of $T$ down to 40 K, then slightly increases, leaps by 0.1 $\mu s^{-1}$ at 30 K and then disappears with further lowering $T$ below 30 K. $\lambda_{\rm TF}$ above 40 K is mainly due to the nuclear magnetic moments of $^{59}$Co nuclei in the paramagnetic state, while the slight increase below 40 K would imply the formation of short-range AF order of Co ionic moments. On the other hand, $\lambda_{\rm slow}$ decreases monotonically with decreasing $T$ below the transition, showing typical critical behaviour for a transition at $T_N$.

These indicate a sharp transition to a long-range AF order which completes below 30 K, that is, $T_N$ = 30 K, which is very consistent with the result of the $C_p$ measurement. Moreover, $A_{\rm slow}$(5 K) corresponds to 1/3 of the maximum value of $A_{\rm TF}$, as expected for a powder sample since 1/3 of the muons experience the internal field component parallel to $\vec{S}_\mu$ (part of the signal known as the "1/3 tail"). Since $A_{\rm TF}$ is proportional to the volume fraction of paramagnetic phases in the sample, the wTF results show that the whole sample volume enters into the AF phase.

In order to investigate the internal magnetic field ($\vec{H}_{\rm int}$) of the AF phase for $Co_3O_4$ in detail, ZF-$\mu^+$SR experiments were performed below 31 K. Figure 2 shows ZF-$\mu^+$SR time spectra at 30.5 K (top), 29.7 K (middle) and 8.1 K (bottom). A clear spontaneous muon spin oscillatory signal due to a quasi-static $\vec{H}_{\rm int}$ is observed below 29.7 K ("quasi-static" means static at least within the time scale of $\mu^+$SR, i.e. up to ∼10 $\mu$s), whereas there is no oscillation signal at 30.5 K, further indicating the appearance of a long-range AF ordered state below 29.7 K.

The Fourier transforms of ZF-$\mu^+$SR time spectra clearly show two distinct frequency components in each spectrum (see Fig. 3). The spectrum at 8 K consists of a main peak at $\nu_2$ = 51.6 MHz and a second broad weaker maximum at $\nu_1$ = 72.7 MHz, corresponding to $H_{\rm int,2}$ = 3.8 kOe and $H_{\rm int,1}$ = 5.4 kOe, respectively. Both $\nu_1$ and $\nu_2$ monotonically decrease with increasing $T$ and disappear simultaneously at 30 K.

The ZF time spectra were well fitted with the following formula [Sugiyama *et al.*, Phys. Rev. **B73**, 224437 (2006)]:

$$\begin{aligned} A_0P(t) &= A_1J_0(2\pi\nu_1 t)\exp(-\lambda_1 t) \\ &\quad + A_2\exp(-\lambda_2 t)\cos(2\pi\nu_2 t+\phi) \\ &\quad + A_{\rm slow1}\exp(-\lambda_{\rm slow1}t) \\ &\quad + A_{\rm slow2}\exp(-\lambda_{\rm slow2}t), \\ &\quad \nu_1 > \nu_2, \end{aligned} \tag{2}$$

where $A_0$ is the total initial asymmetry, $P(t)$ is the muon polarization function, $A_n$, $\lambda_n$ and $\nu_n$ ($n$ = 1 and 2) are the asymmetries, relaxation rates and oscillation frequencies of the two oscillating signals, respectively, $\phi$ is the initial phase of the exponentially damped term, $A_{{\rm slow},n}$ and $\lambda_{{\rm slow},n}$ ($n$ = 1 and 2) are the asymmetries and relaxation rates of the non-oscillating signals, respectively. $J_0(2\pi\nu_1 t)$ is the zeroth-order Bessel function of the first kind. This fitting function represents

presence of incommensurate (IC) magnetic order in the AF phase of $Co_3O_4$. This is because according to the lattice sum calculation, a generalized IC field distribution at the muon site $H$ is given by [Sugiyama *et al., op. cit.*]:

$$P(H) = \frac{2}{\pi}\frac{H}{\sqrt{(H_1^2-H^2)(H^2-H_2^2)}}, \quad H_2 < H < H_1, \qquad (3)$$

where $2\pi\nu_1 = \gamma_\mu H_1$ and $2\pi\nu_2 = \gamma_\mu H_2$ ($\gamma_\mu$: muon gyromagnetic ratio). Since Eq. 3 represents the field distribution in a frequency domain, Eq. 3 is unavailable to fit ZF-$\mu^+$SR time spectra. On the other hand, the sum of $J_0(2\pi\nu t)$ and cosine function, which corresponds to the first two terms in Eq. 2, is known to well represent the fine spectrum of $P(H)$. We thus used Eq. 2 to fit the ZF-$\mu^+$SR spectra of $Co_3O_4$. The two non-oscillating components in Eq. 2 correspond to the "1/3 tail", as described in the previous section on wTF-$\mu^+$SR results.

Figure 4 shows the $T$ dependences of (a) $\lambda_n$, (b) $A_1 + A_2$ and $A_{\rm slow1} + A_{\rm slow2}$, and (c) $\nu_n$ and $\Delta\nu = \nu_1 - \nu_2$ of the two oscillating signals ($n$ = 1 and 2) obtained by the fitting results using Eq. 2. As $T$ decreases from 30 K, both $\lambda_1$ and $\lambda_2$ rapidly decrease with decreasing slope and reach their minima below ~15 K. This is reasonably explained by the critical phenomenon in the magnetically ordered system at the vicinity of $T_{\rm N}$.

$A_1 + A_2$ is almost $T$-independent below $T_{\rm N}$ and levels off to its maximum value (~0.15) for a magnetic powder sample. $A_{\rm slow1} + A_{\rm slow2}$ is also $T$-independent below $T_{\rm N}$ and levels off to half value of $A_1+A_2$ (~0.08). This indicates that $A_{\rm slow1} + A_{\rm slow2}$ represents the 1/3 tail, which is consistent with the result of wTF-$\mu$SR. The result is further evidence supporting that the whole sample enters into the IC-AF order phase below $T_{\rm N}$.

The two $\nu_n(T)$ curves exhibit a similar $T$ dependence (see Fig. 4(c)). As $T$ decreases from 31 K, both $\nu_1$ and $\nu_2$ suddenly appear at 30 K and increase with decreasing $T$, and with decreasing slope. At the vicinity of $T_{\rm N}$, $\Delta\nu$ rapidly increases with decreasing $T$, and seems to level off to ~20 MHz below 20 K. Since $\Delta\nu$ measures the field distribution of the IC order, this implies that the IC AF structure of $Co_3O_4$ is completed at 20 K. This is consistent with the result of the $T$ dependences of the $\lambda_n$ as described above.

The other parameters, $A_{\rm slow1}$, $A_{\rm slow2}$, $\lambda_{\rm slow1}$ and $\lambda_{\rm slow2}$, lack $T$ dependence below $T_{\rm N}$, indicating that the implanted muon does not change the site at least in the time scale of the muon life. The $\phi(T)$ curve is independent of $T$ with $\phi \sim 10^\circ$ at whole temperatures measured. This phase shift is due to the rotation of the initial muon spin direction by 10° to avoid direct positrons from the muon source.

In earlier $\mu^+$SR work, two major precessing signals with $\nu_n$(0 K) = 54 and 78 MHz, plus a minor signal at 150 MHz, were observed in a rocksalt-type CoO ($Co^{2+}O^{2-}$) crystal [Nishiyama *et al.*, Hyp. Int. **104**, 349 (1997)], comparable to the present experimental values of $\nu_n$(0 K) = 60 and 80 MHz for the $[Co^{2+}]_{8a}[Co_2^{3+}]_{16d}[O_4^{2-}]_{32e}$ spinel. In the AF phase of CoO below $T_{\rm N}$ = 290 K, the spins of $Co^{2+}$ ions align parallel to each other on (111) planes, but with anti-parallel spin directions in alternate (111) planes. It is therefore very surprising that $H_{\rm int}$ detected by $\mu^+$ for CoO are almost the same as for $Co_3O_4$, in spite of the fact that the magnetic structure of CoO is so different from that of $Co_3O_4$. This could suggest the existence of $Co^{2+}$ ions in the 16d site in $Co_3O_4$, as in the case for the well-known $Fe_3O_4 = [Fe^{3+}]_{8a}[Fe^{2+}Fe^{3+}]_{16d}[O_4^{2-}]_{32e}$ case.

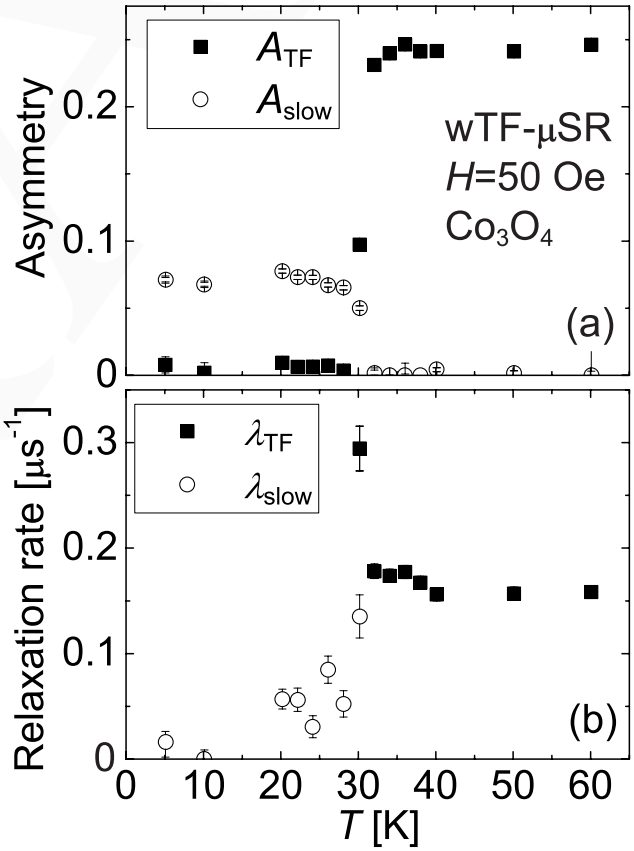


Fig. 1. Temperature dependences of (a) asymmetries ($A_{\rm TF}$ and $A_{\rm slow}$) and (b) relaxation rates ($\lambda_{\rm TF}$ and $\lambda_{\rm slow}$) for $Co_3O_4$. The data were obtained by fitting the wTF-$\mu^+$SR spectra using Eq. 1.

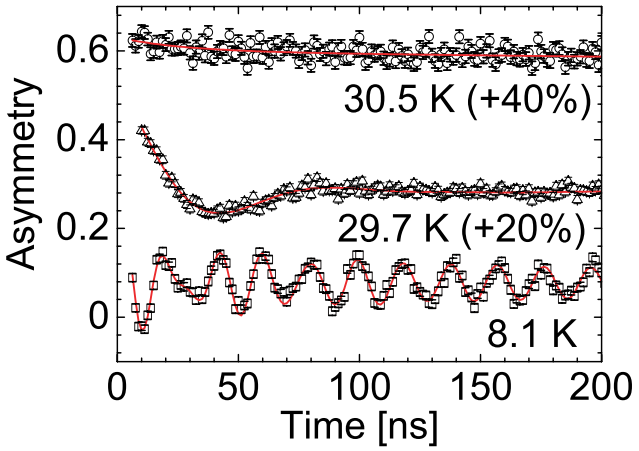


Fig. 2. Early ZF-$\mu^+$SR time spectra for $Co_3O_4$ above and below $T_N = 30$ K. The full spectra extend up to 10 $\mu$s. Solid lines represent fits using Eq. 2.

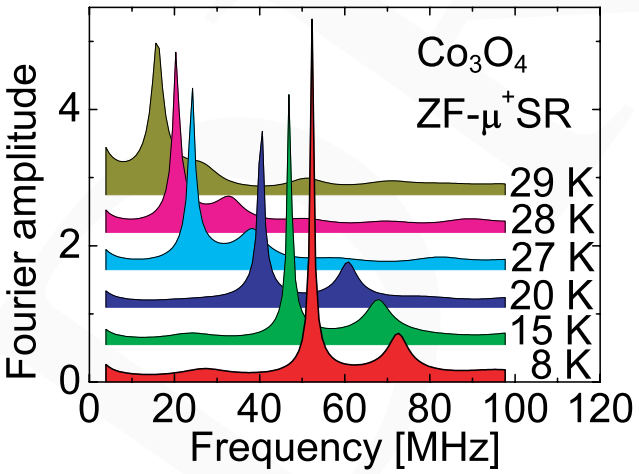


Fig. 3. Fourier amplitude of ZF-$\mu^+$SR spectra at several temperatures below $T_N$.

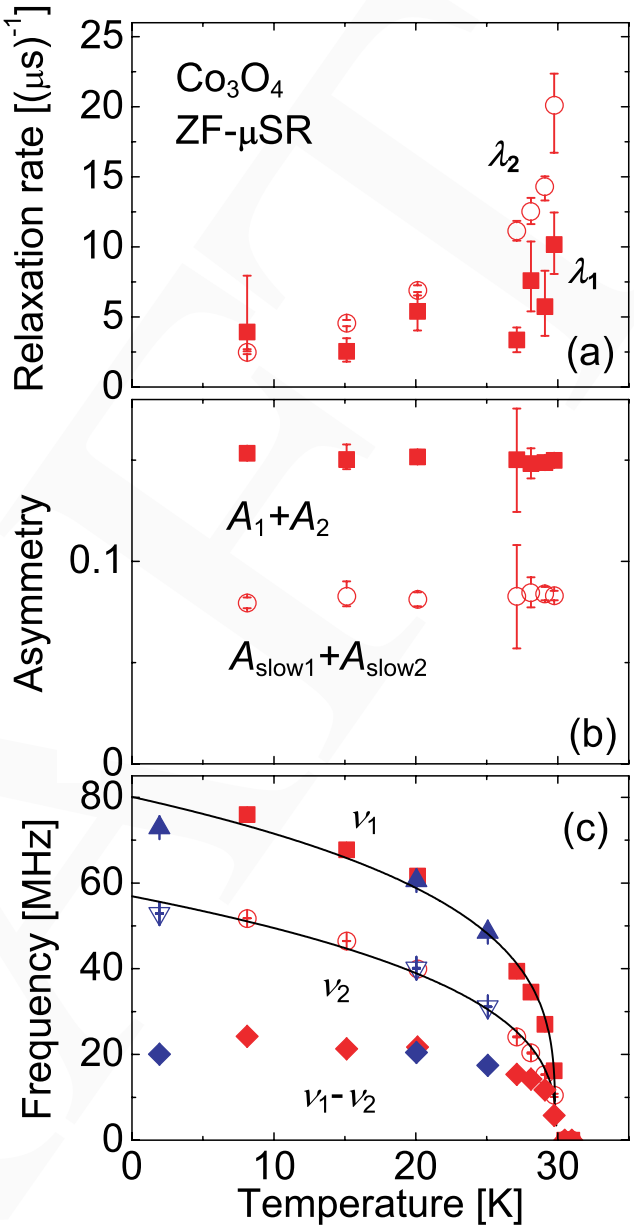


Fig. 4. Temperature dependences of (a) $\lambda_n$, (b) $A_1$+$A_2$ and $A_{slow1}$+$A_{slow2}$, and (c) $\nu_n$ ($n$=1 and 2) and $\Delta\nu = \nu_1 - \nu_2$. These results were obtained by fitting the ZF-$\mu^+$SR spectra with Eq. 2. Solid curves are a guide to the eye.

**Experiment 931**
**Magnetic properties of multinuclear, open-shell coordination complexes and polymers probed by $\mu$SR**
*(J.E. Sonier, J. Lefebvre, D. Leznoff, SFU)*

**Scientific motivation**

The intense interest in metal-organic coordination polymer research can be attributed to the potential to design functional materials with specific physical properties by choosing the appropriate building blocks. A series of isostructural coordination polymers with the

general formula $M(\mu\text{-OH}_2)_2[\text{Au(CN)}_2]_2$ ($M$ = $\text{Cu}^{\text{II}}$, $\text{Ni}^{\text{II}}$, $\text{Co}^{\text{II}}$, and $\text{Fe}^{\text{II}}$) were prepared in the Department of Chemistry at SFU. These compounds have an unusual basic structural motif in which the water molecules play the key structural role; the structure type is unique both with respect to cyanometallate-based polymers and, more broadly, is rare in aqueous coordination chemistry. In these polymers, double aqua-bridges, $M(\mu\text{-OH}_2)_2M$, are found between the metal centres and generate infinite chains.

Since the structural motif often defines the physical properties (e.g. magnetism) of a particular compound, the magnetic behaviour of each analogue was investigated. In addition to SQUID magnetometry experiments, muon spin relaxation ($\mu$SR) studies were carried out. In contrast to bulk magnetic susceptibility measurements, $\mu$SR is a local magnetic probe that is highly sensitive to weak internal magnetic fields, short-range magnetic order and disordered magnetism. Furthermore, $\mu$SR is sensitive to spin fluctuation rates that are beyond the range accessible with ac-susceptibility magnetometry. Using this technique we obtain information on the spin order and dynamics in these compounds, which we correlate to the magnetic interactions mediated along this uncommon bridge and through weak bonding that exists between the chains. Through previous $\mu$SR experiments, we were able to determine that long-range magnetic order was present in the copper analogue below 0.2 K, while the nickel analogue undergoes a transition from a paramagnetic state to a spin-glass state in zero-field at 3.6 K. We concluded that the different magnetic behaviour for these two polymers could be explained by the differences in magnetic interaction pathways, which arise from differences in the structures and the magnetic orbitals involved. To pursue our magneto-structural correlation studies, we investigated the cobalt and iron(II) $M(\mu\text{-OH}_2)_2[\text{Au(CN)}_2]_2$ analogues. We also prepared a similar compound, $\text{Fe}(\mu\text{-OH}_2)(\mu\text{-OH})[\text{Au(CN)}_2]_2$. In this compound, a bridging water molecule has been replaced by a bridging hydroxide group (OH). The effect on the magnetic properties incurred by disrupting the aqua bridge, with only minor structural changes, is of importance to these studies.

**Experimental results**

In 2006, we performed zero-field (ZF) $\mu$SR measurements on $M(\mu\text{-OH}_2)_2[\text{Au(CN)}_2]_2$ with $M$ = Co and Fe and $\text{Fe}(\mu\text{-OH}_2)(\mu\text{-OH})[\text{Au(CN)}_2]_2$. The ZF-$\mu$SR signals for all compounds are well described by a function of the form

$$A(t) = A_1 e^{-\lambda_1 t} + A_2 e^{-\lambda_2 t} + A_{\text{bg}}\,,$$

where the first two terms are contributions from muons stopping in the sample, and the third term comes from muons that stop outside the sample.

Figures 1, 2 and 3 show the temperature dependences of the exponential relaxation rates $\lambda_1$ and $\lambda_2$. Since $\lambda_1(T)$ and $\lambda_2(T)$ exhibit qualitatively similar behaviour in both $\text{Co}(\mu\text{-OH}_2)_2[\text{Au(CN)}_2]_2$ and $\text{Fe}(\mu\text{-OH}_2)_2[\text{Au(CN)}_2]_2$, we associate the two different relaxation rates with two different muon stopping sites. In $\text{Co}(\mu\text{-OH}_2)_2[\text{Au(CN)}_2]_2$, twice as many muons stop at the first site ($A_1 \approx 2A_2$), whereas the same number of muons stop at the two sites in $\text{Fe}(\mu\text{-OH}_2)_2[\text{Au(CN)}_2]_2$ ($A_1 \approx A_2$). In both compounds the increase of $\lambda_1$ and $\lambda_2$ with decreasing temperature indicates a slowing down of spin fluctuations, that essentially saturate below $T = 1$ K. However, no magnetic transition of any kind is observed.

In contrast, the ZF-$\mu$SR relaxation rates behave very differently in $\text{Fe}(\mu\text{-OH}_2)(\mu\text{-OH})[\text{Au(CN)}_2]_2$. Approximately three quarters of the sample signal ($A_1 \approx 3A_2$) is characterized by a slow temperature-independent relaxation rate $\lambda_1$. The remainder of the sample signal is described by an exponential relaxation rate $\lambda_2$ that exhibits cusp-like behaviour near $T = 2$ K, indicative of a magnetic phase transition. Although the large value of $\lambda_2$ at $T = 0.02$ K indicates that the spins do not completely freeze, this analysis of the data is preliminary, and a static component to the ZF-$\mu$SR signal has not been ruled out. The very different behaviours of $\lambda_1(T)$ and $\lambda_2(T)$ may be due to phase separation in the sample. Consequently, further $\mu$SR studies of different $\text{Fe}(\mu\text{-OH}_2)(\mu\text{-OH})[\text{Au(CN)}_2]_2$ samples are being planned to identify the intrinsic magnetic properties of this system.

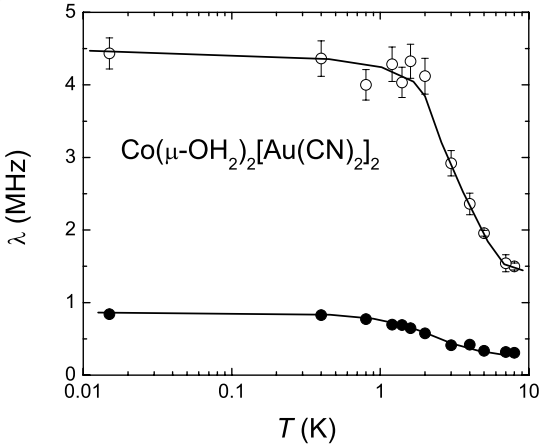


Fig. 1. Temperature dependence of the exponential relaxation rates $\lambda_1$ (open circles) and $\lambda_2$ (solid circles) that describe the ZF-$\mu$SR signal from $\text{Co}(\mu\text{-OH}_2)_2[\text{Au(CN)}_2]_2$.

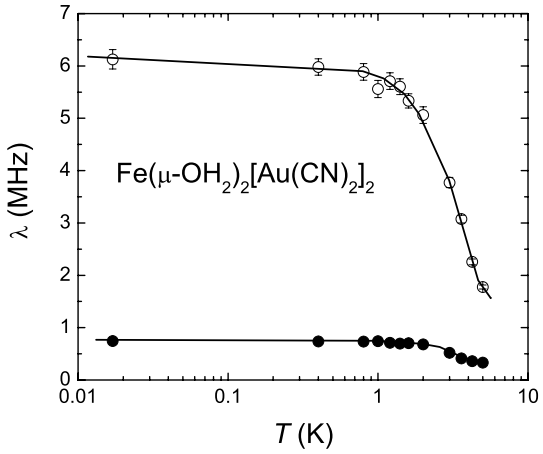


Fig. 2. Temperature dependence of the exponential relaxation rates $\lambda_1$ (open circles) and $\lambda_2$ (solid circles) that describe the ZF-$\mu$SR signal from $Fe(\mu\text{-}OH_2)_2[Au(CN)_2]_2$.

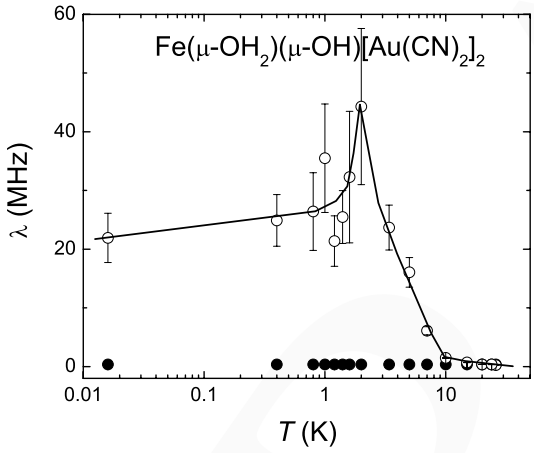


Fig. 3. Temperature dependence of the exponential relaxation rates $\lambda_1$ (open circles) and $\lambda_2$ (solid circles) that describe the ZF-$\mu$SR signal from $Fe(\mu\text{-}OH_2)(\mu\text{-}OH)[Au(CN)_2]_2$.

**Experiment 939**
**Guest-host interactions and Hfcs of Mu-radicals in zeolites**
*(D.G. Fleming, UBC)*

Experiment 939 is concerned with the $\mu$SR measurements of Mu-substituted alkyl radicals in zeolites, primarily Mu-ethyl and Mu-butyl radicals in faujasites. An important motivation of the work is to assess the possible importance of free radical intermediates in these industrially important heterogeneous catalysts, for which there is essentially no ESR data.

This experiment was brought to a close in one final week of M20 beam time in August, with additional data obtained for trans-butene and iso-butene in NaY as well as further data obtained in neat iso-butene and trans-butene. A publication has been submitted to J. Phys. Chem., "Hyperfine interactions and molecular motion of the Mu-ethyl radical in NaY, HY and USY", by M.D. Bridges (2004 UBC Chemistry M.Sc. thesis), D.J. Arseneau, D.G. Fleming and K. Ghandi, which is currently in the refereeing stage. The data analysis for the Mu-butyl radicals is ongoing with the expectation of 2–3 additional papers being published.

**Experiment 944**
**Muonium in silicon carbide**
*(R.L. Lichti, Texas Tech; K.H. Chow, Alberta)*

In previous reports on the Mu defect centres in SiC we characterized two neutral states in the 4H crystal structure and a total of four $Mu^0$ centres in the 6H structure. All of these $Mu^0$ signals show isotropic hyperfine interactions. The $Mu^0$ centre with $A_{hf} = 3029.9$ MHz in 4H-SiC has acceptor properties, thus we assigned it to the expected low energy $T_{Si}$ acceptor site in the cubic-like regions of the 4H structure. Based on that result we also assigned $Mu^0$ states with $A_{hf} \geq 3000$ MHz in 6H-SiC to the two nearly equivalent $T_{Si}$ sites in that structure. The other $Mu^0$ states, all having $A_{hf}$ near 2800 MHz, were then tentatively assigned to various anticipated sites within the 2H-like regions of the more complex hexagonal structures. However, serious questions remain regarding these preliminary $Mu^0$ site assignments.

We have been investigating the muonium charge-state transitions in n-type and p-type samples to make a stronger argument regarding the $Mu^0$ site assignments, specifically to assign donor or acceptor character to each neutral signal. Figure 1 shows the temperature dependence of the diamagnetic amplitude associated with the $Mu^+$ and $Mu^-$ ionic charge states in each electrical type of 6H-SiC from a combination of TRIUMF Expt. 944 data plus results from associated measurements at ISIS. No direct experimental label exists to assign specific features to $Mu^-$ or to $Mu^+$.

The initial assignment of transition processes for steps below 350 K is electron capture to form $Mu^-$ at acceptor sites in n-type and hole capture at donor sites to give $Mu^+$ in p-type samples, based on expectations and correlation of the activation energies with known dopant ionization energies for the N donor (85 meV) and Al acceptor (230 meV). The 400 K step in low-$T$ data on the high-resistivity sample is tentatively assigned to ionization of the $Mu^0$ donor at $AB_C$, the carbon anti-bonding site, while the more complicated result for high-$T$ data taken in an optical furnace looks like a combination of hole capture and ionization.

The high-temperature transition in high-resistivity

and p-type 6H-SiC appears to be the same process, perhaps hole ionization of $Mu^0$ in the low-energy acceptor site, $T_{Si}$. The transition above 300 K in the n-type sample is controlled by a different process, perhaps a $Mu^0$ donor to acceptor site transition followed by rapid electron capture. If correct, these assignments give a Mu donor energy of about 0.28 eV relative to the conduction band and a Mu acceptor energy of roughly 0.87 eV relative to the top of the valence band. However, correlations with disappearance of the appropriate $Mu^0$ signals have not yet convincingly confirmed most of these tentative transition assignments.

Much of the most recent Expt. 944 time was dedicated to examining the behaviour of the $Mu^0$ centres using microwave resonance techniques. Figure 2 shows results for a high-resistivity 6H-SiC sample. These data show that the two signals with $A_{hf} \geq 3000$ MHz ($Mu_1$ and $Mu_{1b}$), tentatively assigned to the $T_{Si}$ acceptor sites, show identical dynamics but disappear with no change in their linewidth, suggesting a shut off of the formation channel rather than a transition out of that state. This conclusion would seem to be problematic for some of the other transition and site assignments. The second signal ($Mu_2$) shows the increase in linewidth expected for a transition out of that $Mu^0$ state. This signal was initially assigned to a metastable acceptor site, $AB_{Si}$, in the short 2H-like channel regions of the structure. We suggest that this transition might be a $Mu^0$ site change.

The energy obtained for $Mu_2$ from the microwave resonance linewidth increase is close to the result for the high-temperature transition in n-type 6H-SiC (Fig. 1). If we are correct that the energy of ~550 meV may be the barrier for a $Mu^0$ site transition, then assignment of $Mu_2$ ($A_2 = 2768$ MHz in 6H-SiC) to the expected donor site, $AB_C$ in the channel regions, makes more sense than the metastable acceptor location. These two results then fit together in a manner consistent with general expectations. The decrease in diamagnetic amplitude for the p-type sample gives ~460 eV (energy not shown in Fig. 1), which appears to correlate well with the result from the resonance amplitude decreases (Fig. 2). A donor to acceptor site transition for the $Mu^0$ precursor thus may also survive consistency checks as an explanation for that feature.

We have obtained similar but less conclusive resonance data for both $Mu^0$ signals from the high-resistivity 4H sample, however the full temperature dependence for the diamagnetic signals in 4H-SiC is not yet available for comparison.

Over the course of this experiment we have collected a fairly large amount of data related to the quite complicated charge-state and site transition dynamics in the two common hexagonal structures of SiC. Although significant progress has been made, a consistent model of these dynamics supported by strong correlations among the various transition features has not yet fully emerged. Consistency with theoretical expectations across the three electrical types is required, and may dictate re-assessment of some additional site and transition assignments, based on arguments similar to those briefly presented above for $Mu_2$.

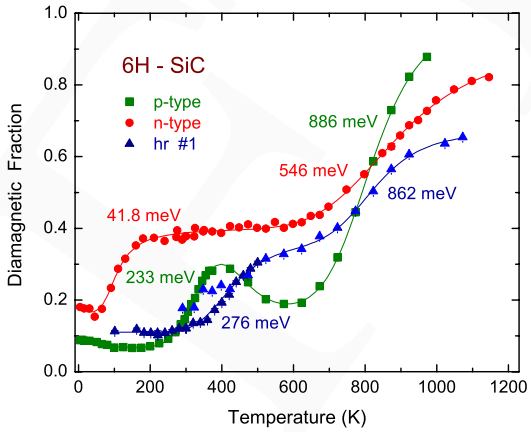


Fig. 1. Temperature dependence of the diamagnetic muon spin-precession amplitudes for the three electrical types of 6H-SiC. Data are a composite from Expt. 944 and various measurements at ISIS.

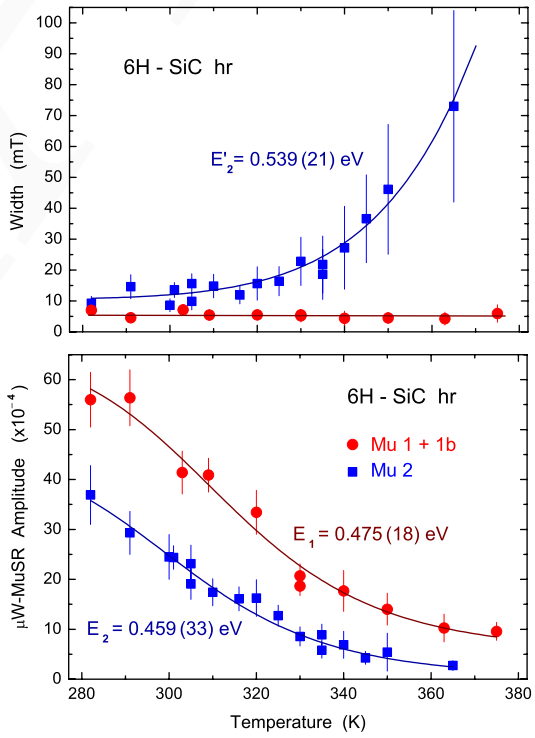


Fig. 2. Linewidths and amplitudes from microwave resonance data on the $\nu_{12}$ lines from the main $Mu^0$ signals in high-resistivity 6H-SiC extend the hyperfine spectroscopy results (HiTime data) to above 300 K.

**Experiment 945**
**Muoniated radicals formed from carbenes and carbene analogues**
*(P.W. Percival, SFU)*

Carbenes (R2C:) are molecules that possess a neutral dicoordinate carbon atom with six valence electrons, which generally results in high reactivity, so that carbenes tend to be considered only as reaction intermediates. However, over the past decade several singlet carbenes have been synthesized and isolated. The addition of a hydrogen atom to a dicoordinate carbon corresponds to a very significant chemical process – the isolated creation of a new chemical bond – and Expt. 945 has been focused on exploring this fundamental chemistry.

Our initial work on the detection and characterization of novel imidazolyl radicals [McKenzie *et al.*, J. Am. Chem. Soc. **125**, 11565 (2003); McKenzie, Ph.D. thesis, SFU (2004)] developed into a study of the temperature dependence of the muon hyperfine constant [Expt. 945, TRIUMF Annual Report 2005]. The goal was to understand how substituents (Ad in Fig. 1) on the imidazole N atoms affect the unpaired spin density on the C radical centre. The muon hyperfine constant provides a measure of the latter, and its temperature dependence is sensitive to various molecular vibrations, in particular the inversion mode at the radical centre, which is in turn coupled to inversion at the N atoms. To test our model and the associated computational predictions we have extended our series of measurements to the Mu adduct of 1,3-bis(adamantyl)imidazol-2-ylidene, which has particularly bulky substituents (see Fig. 1). The results (Fig. 2) are close to expectations and will be combined with the 2005 data in a forthcoming publication.

Another aspect of Expt. 945 involves Mu addition to carbene analogues in which the carbene carbon has been replaced by other Group 14 elements: silicon or germanium. Such novel silylene and germylene compounds have only been synthesized in the past few years, and we are fortunate indeed in having captured the interest and active collaboration of Prof. Robert West (University of Wisconsin), a world leader in this field. His group has recently published the first electron spin resonance spectra of radical adducts of a N-heterocyclic silylene and a germylene [Tumanskii *et al.*, J. Am. Chem. Soc. **126**, 7786 (2004); Tumanskii *et al.*, J. Am. Chem. Soc. **127**, 8248 (2005)]. Relatively large radicals were chosen so that the silyl (or germyl) radical products are stabilized by electron delocalization. Our own experiments with muonium complement this work since instead of creating a Si–C (or Ge–C) bond at the reaction site, we form a Si–Mu (or Ge–Mu) bond. Since Mu is considered an isotopic substitute for H, the radicals that we study are closer to the transient intermediates postulated in various thermal and photochemical reactions of organosilicon and organogermanium compounds.

To date, we have been successful in detecting the muoniated radical formed from a silylene [Expt. 945, TRIUMF Annual Report 2004] and we have continued to study this and other silyl radicals by both transverse-field $\mu$SR and muon level-crossing resonance. Our most recent success is detection of the Mu adduct of an unsaturated germylene. Its transverse-field $\mu$SR spectrum is shown in Fig. 3.

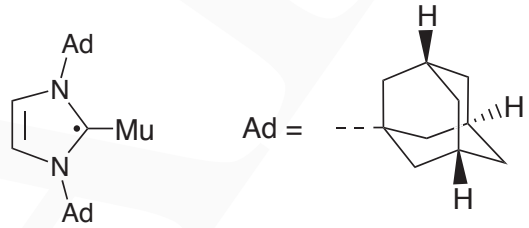


Fig. 1. Formation of a muoniated radical by addition of muonium to 1,3-bis(adamantyl)imidazol-2-ylidene.

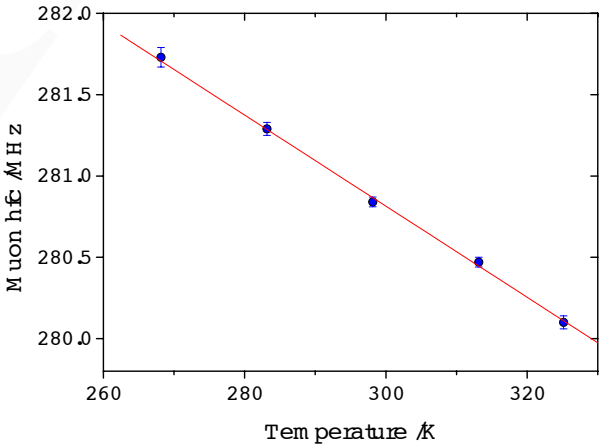


Fig. 2. Temperature dependence of the muon hyperfine constant of the radical shown in Fig. 1.

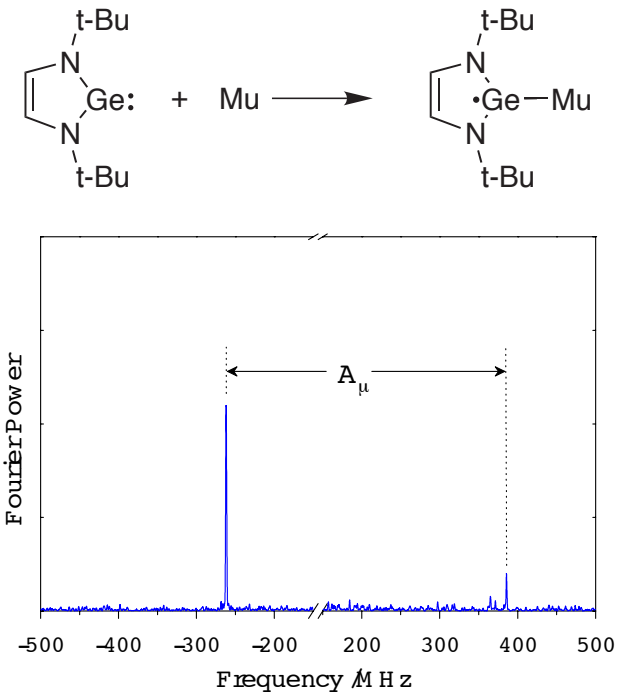


Fig. 3. Upper: Muonium addition to a N-heterocyclic germylene. Lower: Fourier power TF-$\mu$SR spectrum showing the pair of muon precession signals from the germyl radical product. The break in the frequency axis hides the uninteresting but much stronger diamagnetic precession signal.

**Experiment 949**

**$\mu$SR study of magnetic order in high-$T_c$ superconductor under high pressure**

*(T. Goko, J. Arai, Tokyo Univ. of Science)*

In La-214 high-$T_c$ superconductors, suppression of superconducting temperature $T_c$ and a one-dimensional SDW-like magnetic order are observed in the vicinity of $x \sim 1/8$. Until recently, it was widely believed that these anomalies are closely related to the low-temperature tetragonal (LTT) structure. However, recently, we have carried out zero-field $\mu$SR measurements in $La_{2-x}Ba_xCuO_4$ with $x = 0.125$ under pressure up to 1.5 GPa, and have found that $T_m$ increases by applying pressure. The LTT structure is suppressed by pressure and vanishes above ~0.6 GPa [Katano *et al.*, Phys. Rev. **B48**, 6569 (1993)]. We therefore conclude that the LTT structure is dispensable for the magnetic order. On the other hand, it is reported that $T_m$ decreases by applying pressure in $La_{2-x-y}Eu_ySr_xCuO_4$ with $x = 0.15$ and $y = 0.20$ [Klauss *et al.*, Physica **B326**, 325 (2003)]. This pressure dependence is opposite to that for $La_{2-x}Ba_xCuO_4$ with $x = 0.125$. Furthermore, we have revealed that $T_m$ has a negative pressure dependence also in $La_{2-x-y}Eu_ySr_xCuO_4$ with $x = 0.125$ and $y = 0.10$. In order to clarify the origin of the magnetic order, we have performed zero-field $\mu$SR measurements in $La_{2-x-y}Eu_ySr_xCuO_4$ with $x = 0.125$ and $y = 0.025$ under high pressure.

First we exhibited the Eu concentration dependence of the magnetic ordering temperature $T_m$ in $La_{2-x-y}Eu_ySr_xCuO_4$ with $x = 0.125$ in Fig. 1. This experiment had been done at KEK several years ago. The Eu substitution up to $y \sim 0.05$ induces the magnetic order and rapidly increases $T_m$. The Eu substitution shrinks a lattice and enhances a disorder in the A-site ion radii. On the other hand, the Ba substitution for Sr in $La_{2-x}Sr_xCuO_4$ with $x = 0.125$ causes a lattice expansion and an enhancement of the A-site disorder, and increases $T_m$. These results, therefore, indicate that the A-site disorder is one of the most important factors for $T_m$. Above $y = 0.05$, $T_m$ decreases slowly with increasing $y$. This is the optimum Eu concentration for $T_m$.

Figure 2 shows the time dependence of normalized asymmetry for $La_{2-x-y}Eu_ySr_xCuO_4$ with $x = 0.125$ and $y = 0.025$ under pressures of 0.00, 0.20 and 0.72 GPa. This sample lies in the low Eu concentration regime. An oscillation component is observed at low temperatures under pressures up to 0.72 GPa. Here we define the magnetic ordering temperature $T_m$ as the temperature where an oscillation component starts to appear in the $\mu$SR spectra. For example, in the case of ambient pressure (0.00 GPa), $T_m$ exists between 15 and 17 K. These spectra include contributions from the sample signal and the pressure cell. The ratio of the sample signal to the background is typically 1:2. The slow relaxation observed over a wide temperature range is due to the pressure cell.

The values of $T_m$ for $La_{2-x-y}Eu_ySr_xCuO_4$ with $x = 0.125$ and $y = 0.025$ are plotted as a function of pressure in Fig. 3. The pressure dependence of $T_m$ is similar to the Eu concentration dependence of $T_m$ for $La_{2-x-y}Eu_ySr_xCuO_4$ with $x = 0.125$ and $y \geq 0.05$, which is shown in Fig. 1. This similarity suggests that pressure has the same effect on $T_m$ as Eu substitution has, and can be explained in terms of the following scenario. An increase in the A-site disorder caused by Eu substitution or a shrinkage in the distance between the A site and the $CuO_2$ plane caused by pressure enhances local distortion and/or local potential disturbance in the $CuO_2$ plane. A slight disturbance in the $CuO_2$ plane induces/enhances the magnetic order, and an excessive disturbance depresses the magnetic order.

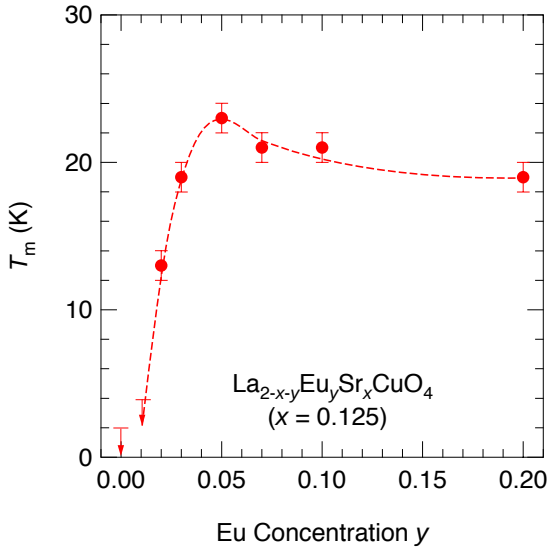


Fig. 1. Eu concentration dependence of $T_{\rm m}$ for $La_{2-x-y}Eu_ySr_xCuO_4$ with $x = 0.125$.

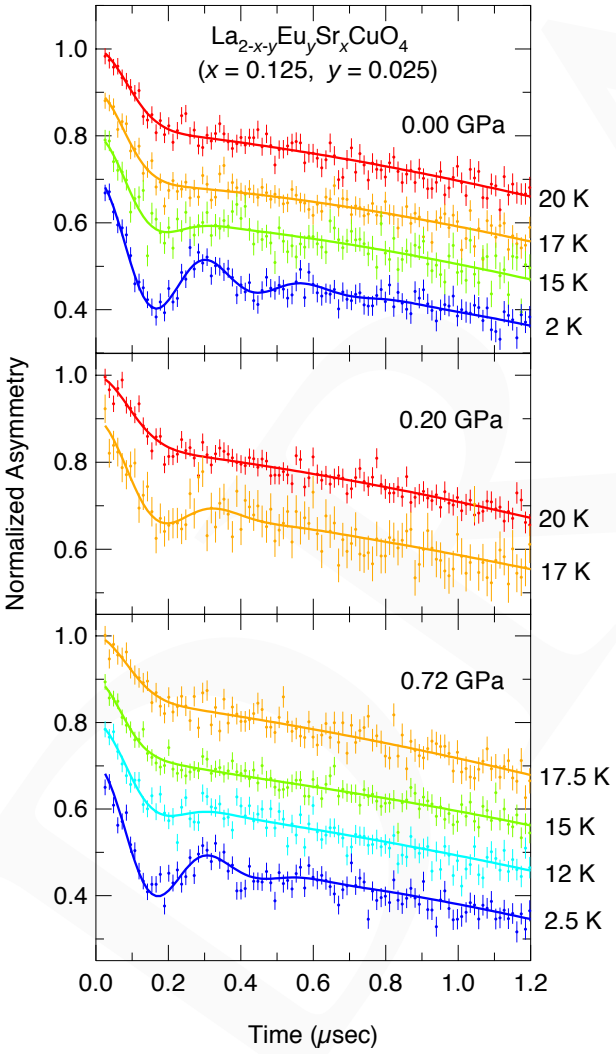


Fig. 2. ZF-$\mu$SR time spectra of $La_{2-x-y}Eu_ySr_xCuO_4$ with $x = 0.125$ and $y = 0.025$ under pressure of 0.00, 0.20 and 0.72 GPa. The spectra are vertically offset for clarity.

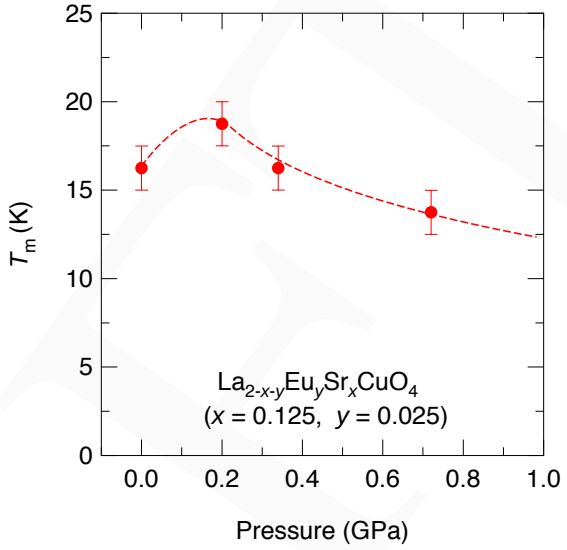


Fig. 3. Pressure dependence of $T_{\rm m}$ for $La_{2-x-y}Eu_ySr_xCuO_4$ with $x = 0.125$ and $y = 0.025$.

**Experiment 951**
**Magnetism and flux line lattice structure of oxychloride superconductors**
*(R. Kadono, KEK-IMSS)*

Oxychloride superconductor $Ca_{2-x}Na_xCuO_2Cl_2$ (Na-CCOC) has uniform $CuO_2$ planes suitable for preparing a clean surface by cleaving and thus it has been the subject of detailed investigation by spectroscopy measurements including STM/STS and ARPES. In particular, the checkerboard-like electronic modulation in underdoped Na-CCOC revealed by STM/STS study [Hanaguri *et al.*, Nature **430**, 1001 (2004)] attracted much attention. Recently, another oxychloride superconductor, $Ca_{2-x}CuO_2Cl_2$ (Ca-def), was discovered [Yamada *et al.*, Phys. Rev. **B72**, 224503 (2005)]. Hole carrier is derived from the deficiency of calcium ion in this system, and the maximum superconducting transition temperature ($T_{\rm C} \simeq 42$ K) upon varying $x$ is about 10 K higher than that of Na-CCOC ($\simeq$30 K), although they are derived from the same parent compound $Ca_2CuO_2Cl_2$ without causing any difference in their crystal structure. In order to compare their magnetic property in the underdoped region, we conducted ZF-$\mu$SR measurements in the polycrystalline samples of Ca-def ($p = 0.056 \sim 0.141$) on the M15 beam line at TRIUMF.

Figure 1 shows the ZF-$\mu^+$SR time spectra obtained at 2 K in the samples of $p = 0.056$, 0.075, 0.094 and 0.141. The spectrum of $p = 0.056$ clearly shows muon pressesion signals due to long-range antiferromagnetic (AF) order. While no precession signal was observed

in superconducting samples with $p = 0.094$ and 0.141 ($T_C = 10$ and 28 K, respectively), a remnant of the precession with fast relaxation is observed at $p = 0.075$. This indicates that the magnetic ground state changes probably from long-range AF to superconducting state through a disordered long-range AF state upon carrier doping. It is interesting to note that the carrier concentration dependence of the magnetic state is different from that seen in Na-CCOC, although the observed tendency is common to that of Na-CCOC. More specifically, the long-range AF state tends to persist at higher carrier concentration (up to $p = 0.056$) in Ca-def than that of Na-CCOC where it changes into a disordered AF state at $p = 0.05$. The observed difference suggests the influence of A-site cation disorder on the magnetic state, which may deserve more detailed study to clarify the intrinsic phase diagram of oxychlorides.

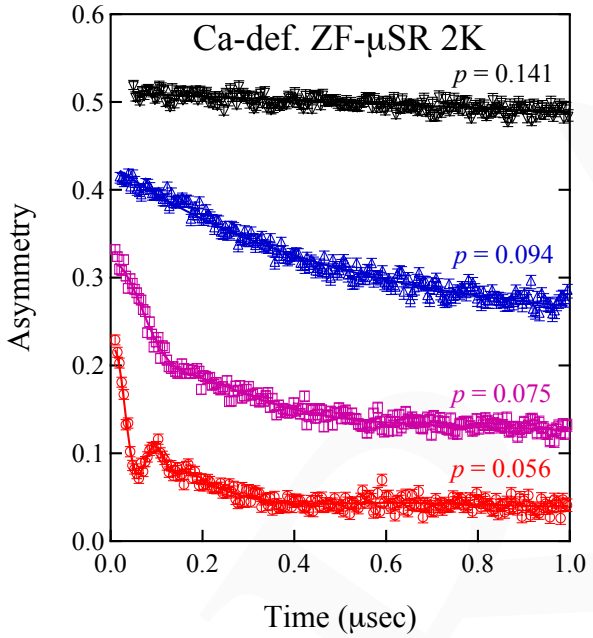


Fig. 1. ZF-$\mu^+$SR time spectra of Ca-def at 2 K. The spectra are offset by 0.1, 0.2, and 0.3 for $p = 0.075$, 0.094, and 0.141, respectively.

## Experiment 958
## HTF-$\mu^+$SR lineshapes in overdoped high-$T_c$ superconductors

*(J.H. Brewer, CIAR/UBC/TRIUMF)*

The magnetic penetration depth $\lambda_{ab}$ and the coherence length $\xi_{ab}$ are revealed indirectly in the field distribution at random sites in the vortex lattice of a Type 2 superconductor in the mixed state, which is very effectively revealed as the Fourier transform of a high transverse field (HTF)-$\mu^+$SR spectrum in the sample. This is therefore our method of choice. Most $\mu$SR experiments on high-$T_c$ superconductors (H$T_c$SC) address mainly the magnetic properties of optimally doped and/or underdoped materials, primarily $YBa_2Cu_3O_x$ ("Y123" or "YBCO").

The original stated goal of Expt. 958 (admittedly somewhat tongue-in-cheek) was to achieve "boring" results of lineshape analyses in overdoped cuprate superconductors – boring in the sense of a good match to theoretical predictions. At the time, the overdoped cuprates were considered to have no exotic properties related to "spin gap" magnetism, $SO(5)$ or quantum critical points. Unfortunately we appear to have missed the first wave of boredom, and now overdoped materials are attracting new theoretical interest.

Our problem with the timely exploitation of disinterest stems from the difficulty of growing high quality single crystal samples of highly overdoped cuprates, in particular $Tl_2Ba_2CuO_{6+\delta}$ (Tl-2201). (It appears to be impossible to grow good single-phase crystals of YBCO that are more than mildly overdoped.)

### $Tl_2Ba_2CuO_{6+\delta}$ (Tl-2201) samples from UBC

The UBC group of R.-X. Liang, D.A. Bonn and W.N. Hardy has spent the past few years learning to make large (several mm across) Tl-2201 single crystals of a quality comparable to their famous YBCO crystals; the difficulty with Tl-2201 is that one of its constituents, $Tl_2O_3$, is highly volatile as well as extremely poisonous. Moreover, overdoping (increasing $\delta$) requires annealing at high temperature and oxygen pressure, conditions under which $Tl_2O_3$ tends to evaporate from the sample. The final annealing therefore must be done in a sealed high pressure cell made of gold. This work is the Ph.D. project of Darren Peets.

In 2005 we were able to make HTF-$\mu^+$SR measurements on the first Tl-2201 single crystals from the UBC group, which had a critical temperature of $T_c = 72$ K. The resultant mosaic was very small and enormous statistics were required to obtain each spectrum. Nevertheless we were able to obtain the lineshapes (frequency spectra) shown last year, along with a preliminary analysis in the time domain.

In 2006 the UBC group supplied us with two more mosaics, this time consisting of a large number of quite small crystals (construction of the mosaics was limited by eye strain). The first had $T_c = 60$ K and the second had $T_c = 46$ K, so we were finally exploring the very overdoped regime with high quality samples. Results are shown in Figs. 1–6.

### Lineshapes in overdoped $Tl_2Ba_2CuO_{6+\delta}$

Lineshapes for the $T_c = 72$ K mosaic were shown last year. Figures 1 and 2 show those for $T_c = 60$ K (the sample with the greatest linewidth); Figs. 3–5 show those for $T_c = 46$ K (the most overdoped sample).

Note that all lineshape plots have the same horizontal scale.

Several features are immediately evident from the frequency spectra. First, all the spectra below $T_c$ exhibit the expected asymmetric shape, with a "tail" extending to high frequency corresponding to muons stopping in or near the vortex cores, and a cusp just below the average frequency due to the van Hove singularity at saddle points between vortices.

Second, the distribution does not go sharply to zero on the low field side, corresponding to the minimum field between vortices; this probably reflects a significant disorder in the vortex lattice, and/or some misalignment of the small individual crystals, which were meant to have their $\hat{c}$ axes parallel to the field.

Third, the sharp background peak from muons stopping in other materials decreases in amplitude with increasing field, reflecting the focusing effect of the field on the beam spot in the Helios spectrometer.

Finally, the overall width and the shift of the cusp with respect to the average field decrease dramatically with increasing field. These last two features are distinctly exhibited in Fig. 6.

**Penetration depth in overdoped $Tl_2Ba_2CuO_{6+\delta}$**

Last year we were only able to show preliminary analyses of the $T_c = 72$ K spectra in the time domain, using fits to a model lineshape function composed of a Gaussian "cusp" and a displaced Lorentzian "tail". This year, thanks in part to the larger samples and higher statistics, we were able to obtain fits to the full vortex lattice distribution using an improved "LSHfit" minimization program based on the venerable "msrfit" and the CERN "MINUIT" library.

The data were not yet fine enough to provide independently reliable estimates of both the penetration depth $\lambda_{ab}$ and the coherence length $\xi_{ab}$, so (as is usually done) we found a value of $\kappa \equiv \lambda_{ab}/\xi_{ab} = 100$ which fit all the spectra satisfactorily and held $\kappa$ fixed in global fits to a range of temperatures at a given field for each sample.

This procedure yielded the following results for the temperature dependence of $\lambda_{ab}^{-2}$, which should be proportional to the density of superconducting carriers in the sample (Fig. 7).

The same data are shown in normalized form in Fig. 8, suggesting that all the samples share roughly the same qualitative behaviour, differing only (or mainly) in the changing values of $\lambda_{ab}^{-2}(0)$ and $T_c$.

Again, several features are obvious. First, all the samples exhibit a roughly linear $\lambda_{ab}^{-2}(T)$ at low temperatures, reflecting nodes in the superconducting energy gap, as expected for a $d$-wave superconductor.

Second, there is a suggestion of a "dip and recovery" behaviour in $\lambda_{ab}^{-2}(T)$ in the region around $\frac{1}{2}T_c$.

Third, while the normalized curves of $\lambda_{ab}^{-2}(T)/\lambda_{ab}^{-2}(0)$ vs. $T/T_c$ look similar, there is a distinctly larger value of $\lambda_{ab}^{-2}(0)$ in the $T_c = 60$ K sample than in either of the other dopings. This is clear evidence of the so-called "boomerang" effect previously observed in a number of unoriented sintered or powdered samples, where $T_c$ grows and $\lambda_{ab}^{-2}(0)$ increases with increasing doping up to optimal doping, and then first $T_c$ decreases while $\lambda_{ab}^{-2}(0)$ continues to increase, followed by both decreasing with further overdoping.

This is clearly shown inn Fig. 9 in the form of a so-called "Uemura plot".

Comparing the 1 kG and 5 kG points at $T_c = 46$ K, we note a much more dramatic $H$-dependence than in near-optimally doped YBCO at 5 kG and 15 kG. This remains to be explored, but we do not think the difference is due to "melting" of the vortex lattice in 5 kG or to formation of 2D "pancake vortices". There might, however, be an incipient transition to a "vortex glass"; if so, it would be unprecedented in the cuprates for it to occur at such a low field.

What cannot be determined from the three points at 1 kG is whether $T_c$ is increasing or decreasing with $\lambda_{ab}^{-2}(0)$ at $T_c = 72$ K, whether the $T_c = 60$ K sample really has the highest possible $\lambda_{ab}^{-2}(0)$, and how the "boomerang" curve approaches $T_c = 0$ at still higher doping.

We will therefore be studying approximately three new Tl-2201 samples in the coming year, hoping to obtain a more complete "boomerang" (the first such measurement on aligned single crystals) and also to determine $\xi_{ab}(H, T)$ if possible.

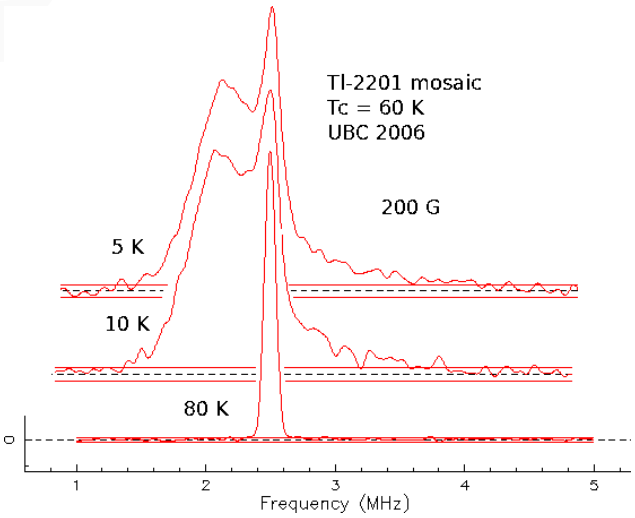


Fig. 1. Fourier transforms of $\mu^+$SR spectra in the $T_c = 60$ K UBC Tl-2201 mosaic at 200 G.

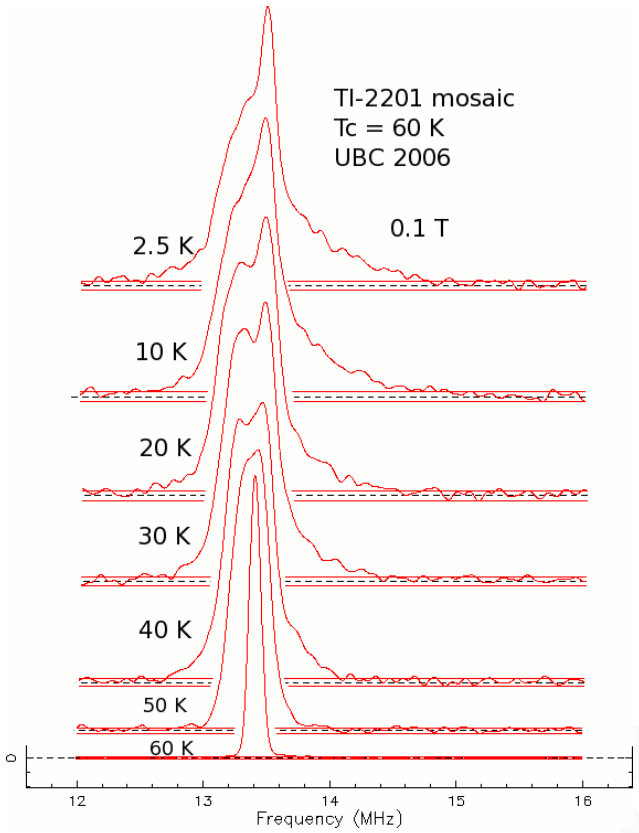


Fig. 2. Fourier transforms of $\mu^+$SR spectra in the $T_c$ = 60 K UBC Tl-2201 mosaic at 1 kG.

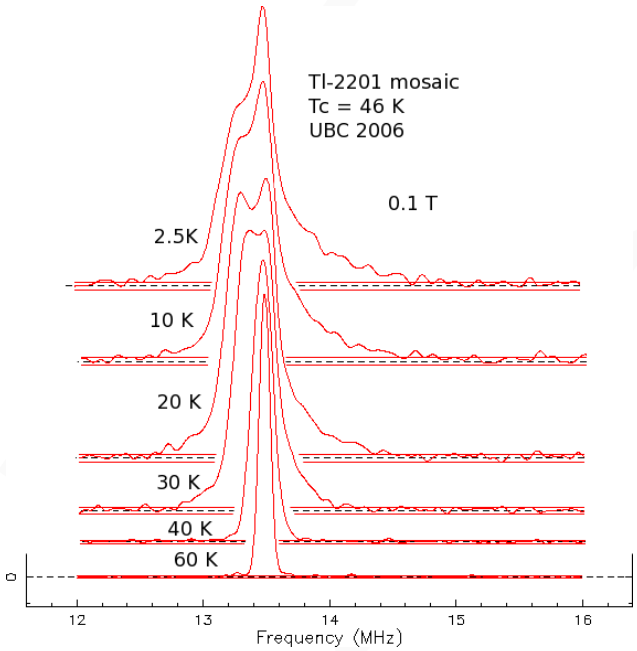


Fig. 4. Fourier transforms of $\mu^+$SR spectra in the $T_c$ = 46 K UBC Tl-2201 mosaic at 1 kG.

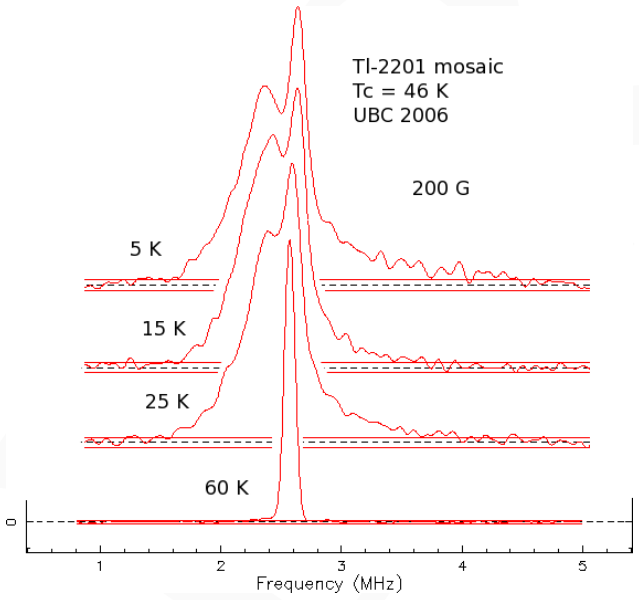


Fig. 3. Fourier transforms of $\mu^+$SR spectra in the $T_c$ = 46 K UBC Tl-2201 mosaic at 200 G.

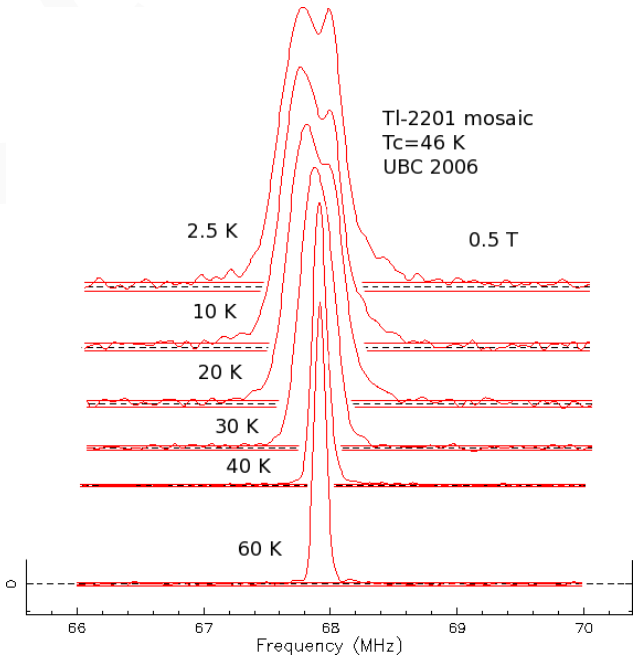


Fig. 5. Fourier transforms of $\mu^+$SR spectra in the $T_c$ = 46 K UBC Tl-2201 mosaic at 5 kG.

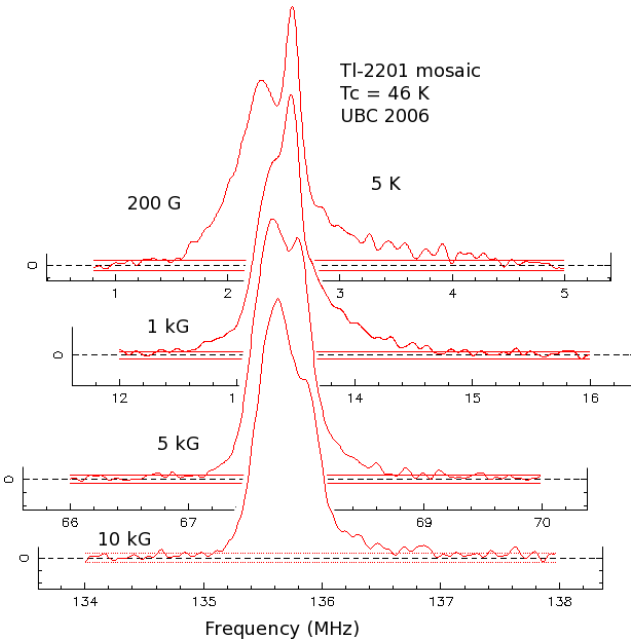


Fig. 6. Fourier transforms of $\mu^+$SR spectra in the $T_c$ = 46 K UBC Tl-2201 mosaic at 5 K in different fields.

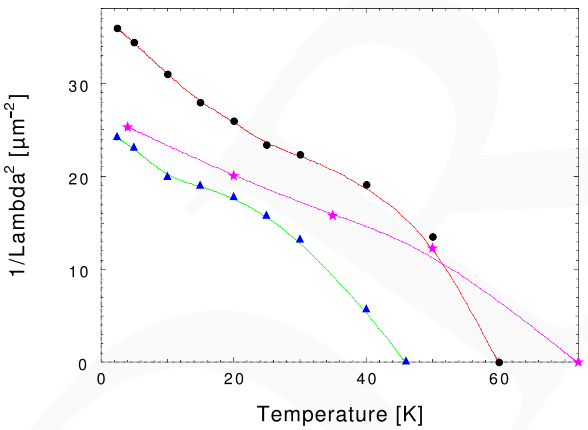


Fig. 7. Temperature dependence of $\lambda_{ab}^{-2}$ in several UBC Tl-2201 samples at 1 kG. Lines are spline fits to guide the eye. All are forced to go through $\lambda_{ab}^{-2}(T_c) = 0$.

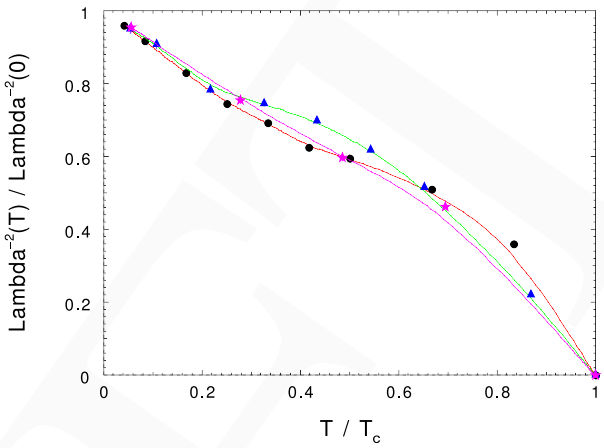


Fig. 8. Dependence of $\lambda_{ab}^{-2}(T)/\lambda_{ab}^{-2}(0)$ upon $T/T_c$ in several UBC Tl-2201 samples at 1 kG.

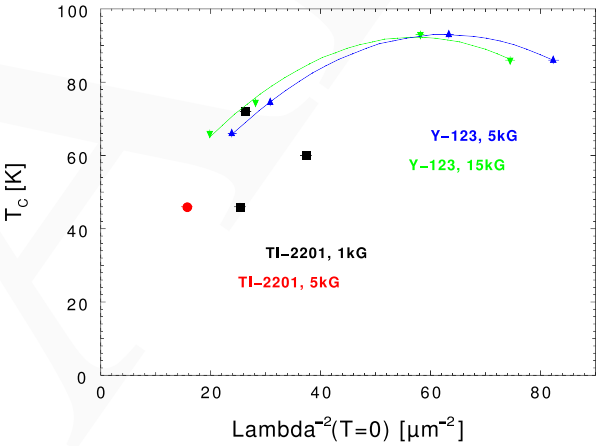


Fig. 9. "Uemura plot" of $T_c$ vs. $\lambda_{ab}^{-2}(0)$ in several UBC Tl-2201 samples at 1 kG (squares) and 5 kG (circle). Values for UBC YBCO crystals (lines through triangles and nablas) are shown for comparison.

## Experiment 976
## Muon Knight shift measurements in the superconducting state of $(Pr_{1-x}La_x)Os_4Sb_{12}$ ($x$ = 0.0, 0.4)

*(W. Higemoto, JAEA-ASRC)*

The discovery of superconductivity in the heavy fermion, filled-skutterudite compound $PrOs_4Sb_{12}$ has attracted much attention due to novel properties [Bauer *et al.*, Phys. Rev. **B65**, 100506(R) (2002)]. $PrOs_4Sb_{12}$ is the first known example of a Pr-based heavy fermion superconductor exhibiting unconventional superconductivity. The crystalline-electric-field(CEF) ground state of the localized $f$-electron has been confirmed to be a non-magnetic $\Gamma_1$ singlet state. The existence of a field-induced antiferro-quadrupolar

ordered phase was proved by neutron scattering experiments. This phase lies close to the superconducting phase and therefore, it is argued that quadrupole fluctuations play an important role for the electron pairing mechanism in the superconducting phase.

La substitution for Pr makes drastic change of superconducting properties. In $Pr_{1-x}La_xOs_4Sb_{12}$, a superconducting transition temperature $T_c$ monotonically decreases with increasing $x$. However, it is not clear how superconductivity changes from unconventional ($x = 0$) to conventional ($x = 1$) and the substitution effect is quite an interesting subject.

One of the central issues for this compound is the symmetry of the superconducting order parameter. In our previous precise zero-field $\mu$SR in $PrOs_4Sb_{12}$, the weak spontaneous internal magnetic field was observed below superconducting transition temperature. This result provides unambiguous evidence of the time reversal symmetry breaking superconductivity [Aoki *et al.*, Phys. Rev. Lett. **91**, 067003 (2003)]. Knight shift provides crucial information about the pairing symmetry of Cooper pairs. Since a muon has spin 1/2, one can deduce the Knight shift without any complication due to an electric field gradient (EFG). In this article, we report on muon Knight shift measurements on single crystalline $Pr_{1-x}La_xOs_4Sb_{12}$ ($x$ = 0.0, 0.4) to elucidate superconducting symmetry and the La substitution effect on it.

Single crystalline specimens of $Pr_{1-x}La_xOs_4Sb_{12}$ ($x = 0.0, 0.4$) were grown by the Sb-flux method. Small ($\sim$1–2 mm) crystals were aligned so that the muon spin rotates in the (001) plane. Magnetic fields were applied along the [001] direction of the crystals. Conventional $\mu$SR measurements under transverse fields (TF) were carried out at the M15 beam line of TRIUMF.

Figure 1 shows a typical spectrum of the fast Fourier transform (FFT) of the $\mu$SR spectra above and below $T_c$ at 3 kOe in $PrOs_4Sb_{12}$. We fitted the $\mu$SR spectra by using a sum of two Gaussian functions, namely,

$$P(t) = \sum_{i=1,2} A_i \exp(-\sigma_i^2 t^2) \cos(-2\pi f_i t + \phi) .$$

We defined the muon Knight shift of $i$-th component $K_i$ as $K_i = (f_i - f_{\rm ext})/(f_{\rm ext})$. Here $f_{\rm ext}$ indicates the external field frequency defined as $f_{\rm ext} = \gamma_\mu B_{\rm ext}/2\pi$, where $B_{\rm ext}$ indicates the external field. In $Pr_{0.6}La_{0.4}Os_4Sb_{12}$, we obtained similar results with $PrOs_4Sb_{12}$. Figure 2 shows the FFT of the $\mu$SR spectra at 5 kOe in $Pr_{0.6}La_{0.4}Os_4Sb_{12}$. From these results, we confirm that the Knight shift does not decrease below $T_c$ in both specimens [Higemoto *et al.*, Phys. Rev. **B75**, 020510(R) (2007); Higemoto *et al.*, J. Mag. Mag. Mat. in press].

No reduction in Knight shift indicates that spin-triplet (odd-parity) superconductivity is realized in $PrOs_4Sb_{12}$. In the previous ZF-$\mu$SR, we have found that the spin or orbital component of the Cooper pairs in $PrOs_4Sb_{12}$ carries a nonzero momentum and generates a hyperfine field at the muon site. Even in the spin-triplet pairing case, there are still two possible sources for the magnetic fields observed in the ZF-$\mu$SR measurements. Theoretically, several possible pairing symmetries have been discussed. For example, it is argued that a spin-triplet superconductivity can possibly be stabilized by considering an exciton-mediated pairing mechanism in the $T_h$ symmetry [Matsumoto and Koga, J. Phys. Soc. Jap. **74**, 1686 (2005)]. However, there are still several candidates for the pairing symmetry. Further experimental and theoretical investigations are required.

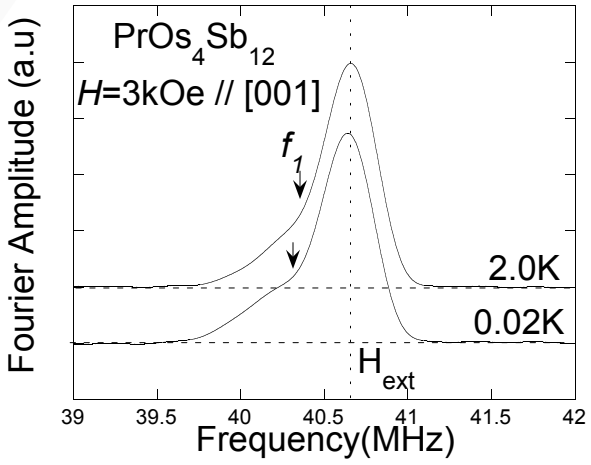


Fig. 1. FFT spectra of the $\mu$SR signal above and below $T_c$ at 3 kOe in $PrOs_4Sb_{12}$. Arrows indicate the muon spin rotation frequency for peak $f_1$.

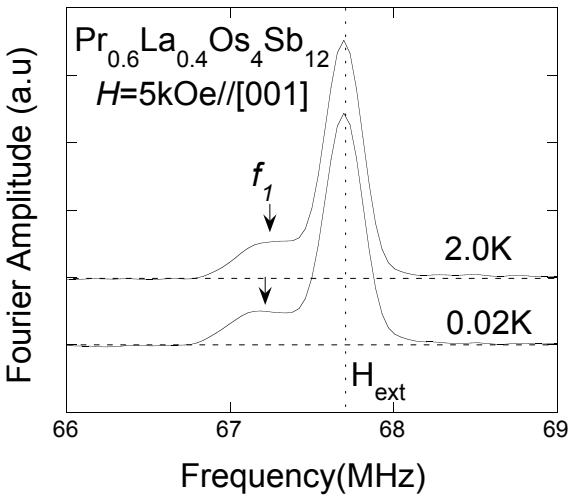


Fig. 2. FFT spectra of the $\mu$SR signal above and below $T_c$ at 5 kOe in $Pr_{0.6}La_{0.4}Os_4Sb_{12}$. Arrows indicate the muon spin rotation frequency for peak $f_1$.

**Experiment 998**

**Muon spin relaxation and dynamic scaling in novel magnetic materials**

*(D.E. MacLaughlin, California, Riverside; R.H. Heffner, JAEA-ASRC, Tokai)*

In the antiferromagnetic insulator $NiGa_2S_4$ the $Ni^{2+}$ ions ($S = 1$) form a two-dimensional triangular sublattice, so that their spins are geometrically frustrated if the interplanar exchange coupling is small. A van der Waals gap separates the planes in the crystal structure, so that this condition is fulfilled and $NiGa_2S_4$ is a quasi-2D spin system. The specific heat indicates freezing of single-spin excitations at roughly the Curie-Weiss temperature $\theta_W \approx 80$ K. Considerable remaining entropy ($\sim\frac{1}{3}\ln 3$ per spin) is found down to $\sim$10 K, however, suggesting a high degeneracy of more complicated low-energy states due to magnetic frustration in the triangular lattice. The entropy loss below $\sim$10 K suggests freezing out of these degenerate states. Specific-heat measurements at low temperatures exhibit a $T^2$ dependence, with practically no field dependence up to $\sim$7 T. This behaviour indicates gapless linearly-dispersive field-independent low-lying modes, suggesting long-range correlations, associated with a singlet spin liquid, that do not couple directly to a uniform field. Such behaviour is surprising in light of the short spin correlation length observed using neutron diffraction.

We have carried out $\mu$SR experiments in $NiGa_2S_4$ at the M20 beam line at TRIUMF. At 2.1 K the muon depolarization function $P(t)$ is distinctly nonexponential, with extremely rapid initial relaxation (Fig. 1; note this is a semilog plot). This initial depolarization might be due to muonium formation, but the maximum expected polarization $P(0) \approx 0.2$ is recovered above $\sim$10 K. This is near the crossover indicated by the specific heat data, suggesting a magnetic origin for the rapid initial relaxation; moreover, a muonium ionization energy this low would require an unphysically large dielectric constant ($\gtrsim$100). Thus the data are consistent with strong inhomogeneity of the $Ni^{2+}$ spin dynamics in $NiGa_2S_4$.

A sum of two components $P(t) = A_rG_r(t) + A_sG_s(t)$, where $A_r$ and $A_s$ are the component amplitudes, gives good fits with a rapidly-relaxing component $G_r(t) = \exp(-\lambda_r t)$, a "power-exponential" slowly-relaxing component $G_s(t) = \exp\left[-(\Lambda_s t)^K\right]$, and no asymmetry loss ($A_r + A_s = \text{const.}$). We do not observe the Gaussian muon relaxation found in some related Kagomé-lattice compounds that exhibit a similar field-independent $T^2$ specific heat.

The temperature dependencies of $\lambda_r$, $\Lambda_s$, the slow-component fractional amplitude $\eta_s = A_s/(A_r + A_s)$, and $K$ are given in Figs. 2–4. The two relaxation rates are very different in magnitude and in dependence on temperature (Fig. 2): $\Lambda_s$ increases with decreasing temperature to a maximum at $\sim$6 K and then decreases at lower temperatures, whereas $\lambda_r$, measurable only below $\sim$15 K where $A_r$ becomes appreciable (Fig. 3), saturates at about 50 $\mu s^{-1}$ at low temperatures. This behaviour is expected of a static order parameter but, as noted below, other properties of the muon spin relaxation do not necessarily support such a picture. Figure 4 shows that $G_s(t)$ is most inhomogeneous (smallest $K$) near 10 K but becomes roughly exponential ($K \approx 1$) at low temperatures and near 100 K. Below 20 K, however, $P(t)$ as a whole is highly nonexponential, indicating strong inhomogeneity in the spin dynamics.

The data of Fig. 1 exhibit neither the long-lived "1/3 tail" in low applied field nor the restoration of slow full-amplitude relaxation (decoupling) in a strong longitudinal field $H_L$ expected for a static field distribution due to frozen spins. Thus the observed behaviour suggests that the relaxation is not static but dynamic, i.e., due to $Ni^{2+}$ spin fluctuations. The complicated form of $P(t)$ makes this conclusion tentative, however. The muon spin relaxation becomes slower with increasing $H_L$ up to 2700 Oe.

The strongly inhomogeneous spin dynamics agree with the short spin correlation length found from neutron scattering. The spin fluctuations become very slow for a fraction of the sample volume that increases strongly with decreasing temperature below $\sim$15 K. There is no evidence for spin freezing, in agreement with a number of recent theoretical pictures. The field dependence ($\mu_B H_L \ll k_B T$) of the muon relaxation

(cf. Fig. 1) suggests that the spin excitations responsible for this relaxation, unlike those responsible for the specific heat, couple to the applied field.

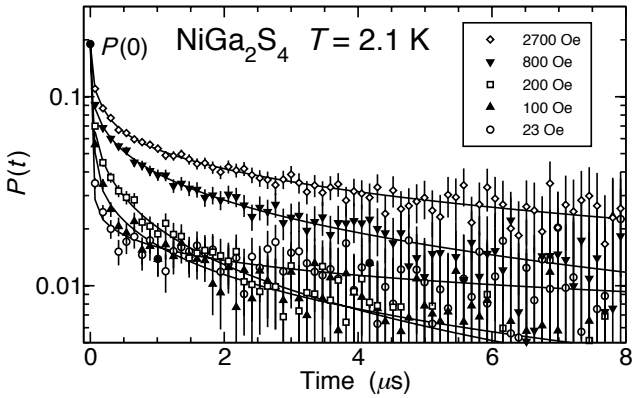


Fig. 1. Dependence of muon spin depolarization function $P(t)$ on longitudinal field $H_L$ in $NiGa_2S_4$ at 2.1 K. Curves: fits as described in the text.

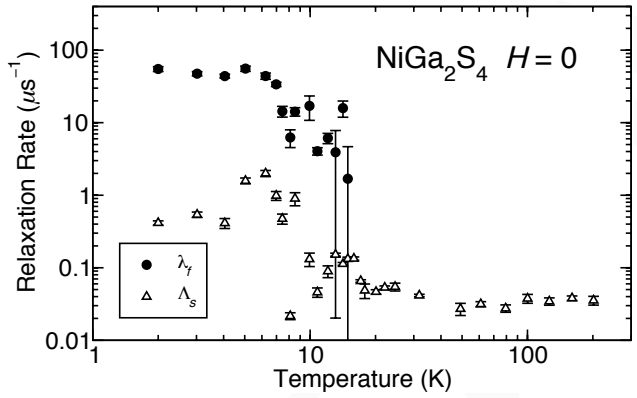


Fig. 2. Temperature dependence of rapid and slow zero-field muon spin relaxation rates ($\lambda_r$ and $\Lambda_s$, respectively; see text) in $NiGa_2S_4$.

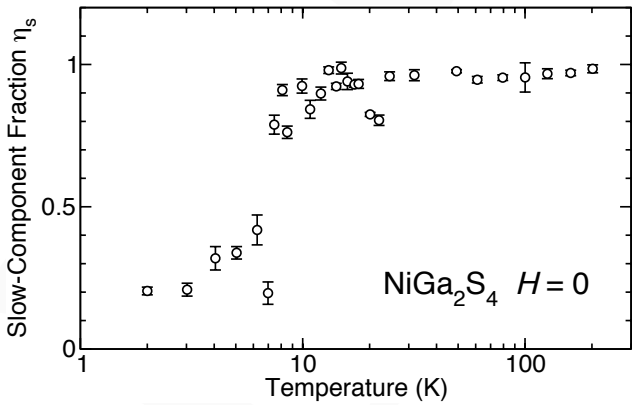


Fig. 3. Temperature dependence of the slow-component fractional amplitude $\eta_s = A_s/(A_r + A_s)$ (see text) in $NiGa_2S_4$.

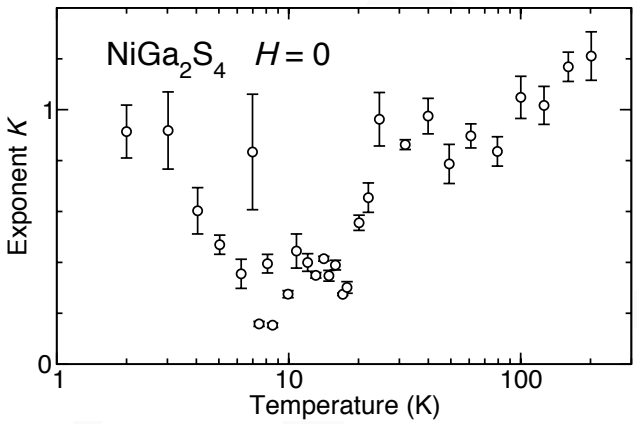


Fig. 4. Temperature dependence of the exponent $K$ for slow-component power-exponential fits (see text) in $NiGa_2S_4$.

**Experiment 1000**
**Measurements of the vortex core size in type-II superconductors**
*(J.E. Sonier, SFU)*

**Scientific motivation**

For nearly two decades, arrival at a firm theory for high-$T_c$ superconductivity has been hindered by an incomplete characterization of the phase diagram for doped copper oxides. There is speculation today about a quantum critical point (QCP) under the superconducting (SC) dome, corresponding to a zero-temperature phase transition at which a competing order is stabilized, and about which unusual properties emerge. So far the main experimental evidence for this has come from $\mu$SR and neutron scattering measurements on $La_{2-x}Sr_xCuO_4$. Zero-field (ZF) $\mu$SR on Zn-substituted samples reveal a SG transition at what has been argued to be a universal critical doping concentration $p_c = x \gg 0.19$. However, neutron studies of field-induced static magnetism in $La_{2-x}Sr_xCuO_4$ suggest there is a zero-field QCP closer to $x = 0.125$, supporting a proposed phase diagram in which the pure superconductor undergoes a quantum phase transition (QPT) to coexisting SC and spin-density-wave (SDW) orders.

It is now well established that a common intrinsic normal-state property of high-$T_c$ superconductors is the occurrence of a field-induced metal-to-insulator crossover (MIC) at low temperatures at a non-universal doping. It has been hypothesized that the MIC is associated with a QCP, at which remnants of the antiferromagnetic (AF) phase disappear. However, this interpretation is not widely accepted, as experiments that measure the MIC do not determine whether there is a competing magnetic order hidden in the SC phase at zero magnetic field. Moreover, neither the zero-field QCP deduced from the neutron studies,

nor the QCP inferred from ZF-$\mu$SR experiments, correspond to the critical doping for the normal-state MIC.

Kivelson *et al.* [Phys. Rev. **B66**, 144516 (2002)] have proposed that the true field-induced QPT in high-$T_c$ superconductors is one in which the competing order parameter is stabilized in a halo around weakly interacting vortex lines. In this situation the magnitude of the competing order parameter is spatially inhomogeneous and may only be detectable by a local probe technique, such as $\mu$SR.

**Experimental results**

Figure 1 shows the tail regions of the Fourier transforms of the muon spin precession signal in the vortex state of $YBa_2Cu_3O_y$ near the critical doping $y_c = 6.55$ for the normal-state MIC. The Fourier transform, often called the $\mu$SR line shape, provides a fairly accurate visual illustration of the internal magnetic field distribution $n(B)$ sensed by the muons. On the high-doping side of the MIC, the $\mu$SR line shapes for the $y = 6.67$, $y = 6.60$ and $y = 6.57$ samples are nearly identical, while the line shapes for the $y = 6.50$ and $y = 6.46$ samples on the low-doping side of the MIC are clearly different. At $y = 6.50$, there is a clear suppression of the high-field tail, which corresponds to the spatial region of the vortex cores. A previous $\mu$SR study of $y = 6.50$ at higher fields concluded that the unusual high-field tail originates from AF vortex cores, but in fact this feature of the $\mu$SR line shape is also consistent with static magnetism that is not ordered. At $y = 6.46$ the change in the high-field tail is accompanied by the appearance of a low-field tail, which indicates an enhancement in the size of the average magnetic field at the muon site(s).

Similar differences between the $\mu$SR line shapes above and below the critical doping $x_c \approx 0.16$ for the MIC are also observed in $La_{2-x}Sr_xCuO_4$ (Fig. 2). At higher magnetic field where the density of vortices in the sample is greater, the differences in the tails of the $\mu$SR line shapes become more apparent (compare Figs. 2(b)–(d)), consistent with an increased volume of magnetism in the low-doped samples. With increasing temperature, the line shapes become more alike (see Figs. 2(c), (e) and (f)), signifying thermal destruction of the static magnetism in and around the vortex cores. This is also confirmed by a detailed analysis of the muon spin precession signal. Figure 2(g) shows the temperature dependence of the relaxation rate $\Lambda$, which is a measure of the field inhomogeneity associated with the static magnetism induced in and around the vortex cores. The diverging temperature dependence of L indicates a slowing down of Cu spin fluctuations, which is entirely consistent with the approach to a second-order magnetic phase transition at $T = 0$ K.

Our experiments establish the presence of a field-induced QPT below the SC dome that coincides with the critical doping for the MIC (see Fig. 3). At relatively weak fields, competing disordered static magnetism is stabilized in and around weakly interacting vortices at the QPT. This confirms one of the main theoretical predictions of the modified phase diagram proposed by Kivelson and co-workers. Accounting for the interlayer couplings of vortices in neighbouring $CuO_2$ planes, Kivelson *et al.* showed that a competing phase could be stabilized in nearly isolated vortices, thus altering the position and character of the QPT. In their theoretical model, the pure superconductor undergoes a field-induced QPT to a coexistence phase in which the competing order parameter (which we identify here as the mean squared local magnetization) is spatially inhomogeneous. With increasing field, stronger overlap of the magnetism around neighboring vortices may lead to a co-operative bulk crossover to long-range magnetic order, as is apparently the case in $La_{2-x}Sr_xCuO_4$.

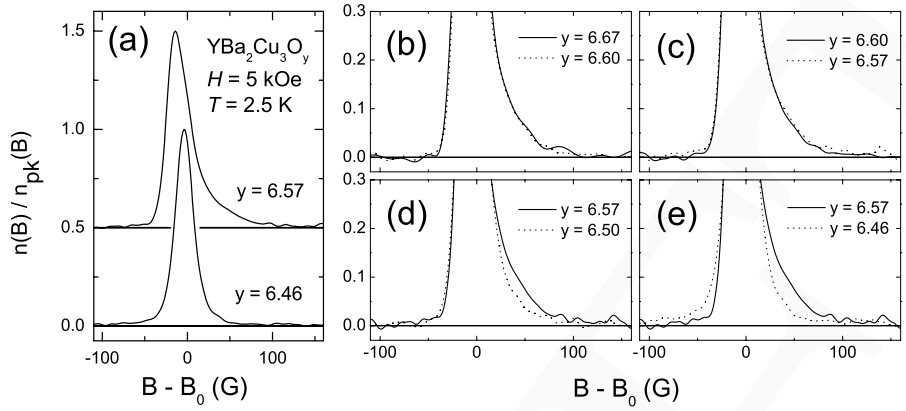


Fig. 1. Doping dependence of the $\mu$SR line shapes for $YBa_2Cu_3O_y$ at $H = 5$ kOe and $T = 2.5$ K. (a) Examples of the Fourier transforms of the measured muon spin precession signal in the vortex state for samples with oxygen content above ($y = 6.57$) and below ($y = 6.46$) the critical doping $y_c \approx 6.55$ for the normal-state MIC. (b), (c), (d), (e) Blowups of the tail regions of the Fourier transforms for samples above ($y = 6.67$, 6.60 and 6.57) and below ($y = 6.50$ and 6.46) the critical doping for the MIC. For comparison, all the line shapes have been normalized to their respective peak amplitude $n_{\rm pk}(B)$. Furthermore, to account for changes in the magnetic penetration depth, the widths of the line shapes in (b), (c), (d), and (e) have been made equivalent by rescaling the horizontal $B - B_0$ axis, where $B_0$ is the applied magnetic field.

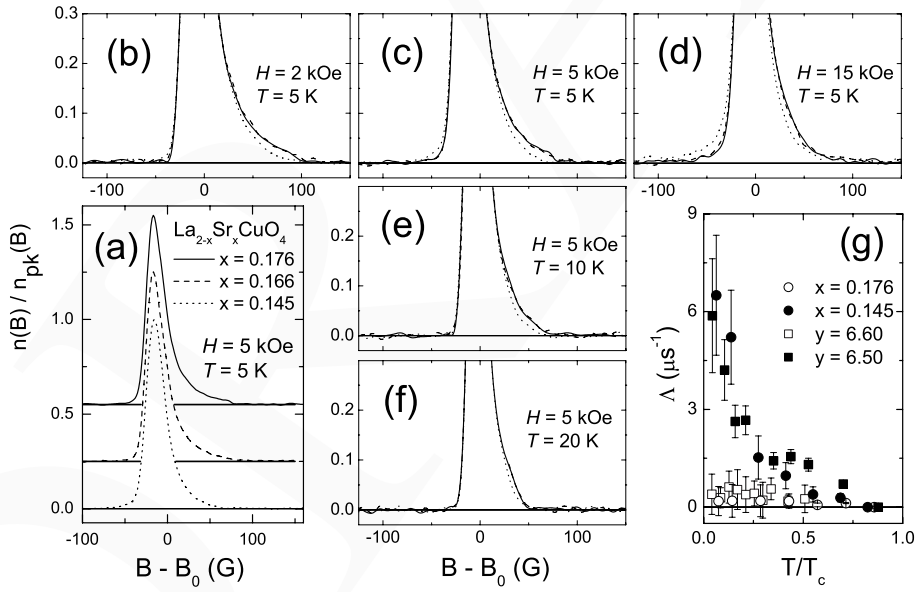


Fig. 2. Doping, temperature and magnetic field dependences of the mSR line shapes for $La_{2-x}Sr_xCuO_4$. (a) Fourier transforms of the measured muon spin precession signal in the vortex state of samples with strontium content above ($x = 0.176$ and $x = 0.166$) and below ($x = 0.145$) the critical doping $x_c \approx 0.16$ for the normal-state MIC. (b), (c), (d), (e), (f) Blowups of the tail regions of the Fourier transforms. The height and width of the line shapes have been normalized in the same way as in Fig. 1. With increasing magnetic field, (b), (c) and (d) show the suppression of the high-field tail and growth of the low-field tail for the sample with $x = 0.145$. Panels (c), (e) and (f) show that both tails gradually disappear with increasing temperature. (g) Temperature dependence of the relaxation rate $\Lambda$ for $La_{2-x}Sr_xCuO_4$ (circles) and $YBa_2Cu_3O_y$(squares) at $H = 5$ kOe. The open and solid symbols denote samples on the high-doping and low-doping sides of the critical doping for the normal-state MIC, respectively.

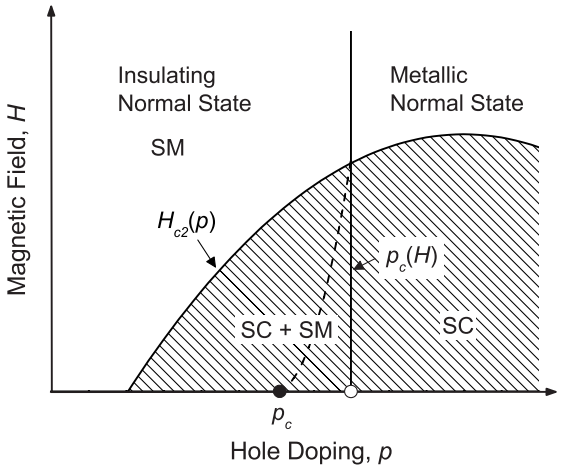


Fig. 3. Schematic zero-temperature phase diagram of high-$T_c$ superconductors deduced from this study. The SC (hatched region) and normal phases occur below and above the upper critical field $H_{c2}(p)$, respectively. The vertical solid line at $p_c(H)$ represents a QPT at finite $H$ coinciding with the low-temperature normal-state MIC. Below $H_{c2}$, the phase boundary $p_c(H)$ separates a pure SC phase from a SC phase coexisting with static magnetism (SM). Just to the left of $p_c(H)$ the SM is disordered, but strong coupling between neighbouring vortices may result in a crossover to long-range magnetic order (above the dashed curve), as is apparently the case in $La_{2-x}Sr_xCuO_4$. On the other hand, according to Kivelson *et al.*, $p_c(H)$ must have a discontinuity at $H = 0$, i.e. an avoided QCP (open circle), with the QCP at $H = 0$ (solid circle) lying at a lower doping concentration. Above $H_{c2}$, $p_c(H)$ separates the metallic and insulating normal phases. The unusual charge localization that occurs below $p_c(H)$ results from the onset of field-induced SM. The phase boundary $p_c(H)$ is non-universal, occurring in the underdoped region of the phase diagram for $YBa_2Cu_3O_y$, but at optimum doping for $La_{2-x}Sr_xCuO_4$. Our experiments probe the region well below the dashed curve.

## Experiment 1001
## Muonium defect levels in semiconductors

*(R.L. Lichti, Texas Tech)*

The main goal of this experiment has been to obtain ionization energies for each $Mu^0$ centre observed in several semiconductors in which at least two separate $Mu^0$ signals are observed. Generally, the two neutrals can be assigned to sites that separately have donor and acceptor characteristics. In zincblende compounds, the bond centre (BC) site has donor properties since it is the stable location for $Mu^+$ and one of the T-sites is stable for $Mu^-$, and thus has acceptor properties. Ionization energies for the $Mu^0$ centres at these sites locate the donor and acceptor levels relative to the conduction and valence band edges respectively, subject to a correction of one of these levels for the site metastability of $Mu^0$. The BC site is usually the low-energy $Mu^0$ location when that signal is observed, thus the $Mu^0_{BC}$ ionization energy locates the donor level relative to $E_C$. The BC neutral is seen in GaAs, and GaP, but not in any other III-V or in the II-VI compounds. ZnSe shows two isotropic $Mu^0$ signals at very low temperatures. These may be from the two different T-sites, individually having donor ($T_{Se}$) and acceptor ($T_{Zn}$) properties.

We have recently obtained the Mu acceptor energy in GaAs by careful analysis of existing RF-$\mu$SR data on growth of the diamagnetic signal between 300 and 400 K coupled with the relaxation rates from TF-$\mu$SR data which imply that the final state of that transition is $Mu^-$ rather than $Mu^+$. The T-site ionization energy from this analysis places the $T_{-/0}$ data point for GaAs in Fig. 1. The Mu defect levels we obtain for GaAs, and those found earlier for Si and Ge, are displayed within a theoretical band alignment scheme in which the midpoint between donor and acceptor levels of hydrogen is claimed to be at a constant energy independent of host material. We obtained an experimental determination of the offset between the BC and T-site energies in GaAs based on an interpretation of $Mu^+$ motion characteristics; indirectly yielding the correction from the $T_{-/0}$ experimental point to the thermodynamic Mu acceptor level. This adjustment for the metastability of $Mu^0_T$ compared to $Mu^0_{BC}$ had been directly measured for Ge but only estimated for Si. The results shown in Fig. 1 support universality but place the Mu pinning level (broken line) 0.3 to 0.5 eV higher than the predicted hydrogen pinning energy. We continue our efforts to add GaP, ZnSe, and perhaps SiC to this diagram to further test the theory.

**ZnSe results**

Earlier spin-precession results for ZnSe demonstrated that a transition from one isotropic $Mu^0$ centre to another takes place below 50 K. Based on a prediction that the T-site with Zn neighbours should have the lower energy for a $Mu^0$ centre, we tentatively assigned the final state $Mu_{II}$ to the $T_{Zn}$ acceptor site, and the initial state $Mu_I$ to the donor site $T_{Se}$. This was supported by calculated hyperfine constants for $Mu^0$ in the two T-sites of ZnSe. Figures 2 and 3 show the results of a series of microwave resonance measurements on the $Mu_{II}$ centre.

At power levels that do not saturate this signal, up to 280 K we observe clear evidence (Fig. 2) of nuclear hyperfine (*nhf*) contributions from a spin 1/2 neighbour but no evidence of neighbours with a larger nuclear spin. This demonstrates interaction with $^{77}$Se (7.6% $I = 1/2$) rather than with $^{67}$Zn (4.1% $I = 5/2$); thus we are forced to conclude that both of the amplitude peaks in Fig. 3 are from $Mu^0$ at the $T_{Se}$ donor site, reversing the earlier assignment. Observation of these *nhf* lines also implies that this $Mu^0$ centre is sta-

tionary in ZnSe, in contrast to the rapid motion seen for $Mu_T^0$ in most other cubic diamond or zincblende structured semiconductors. Above about 300 K the Se *nhf* lines broaden and weaken, suggesting the onset of motion. This needs to be pursued to higher temperatures to verify motion and determine whether there is motional averaging of the primary hyperfine constant, which would imply that $Mu^0$ visits both T-sites.

As seen in Fig. 3, the resonance amplitude for $Mu_{II}$ disappears very soon after the low-temperature site change and then reappears near 200 K. The energy associated with this low-$T$ decrease is consistent with the ionization energy for the native defect that makes ZnSe naturally n-type. The amplitude suppression is incomplete for a second ZnSe sample, but both show the second peak in amplitude near 260 K. There are numerous features in the TF-$\mu$SR and RF-$\mu$SR data on the diamagnetic $Mu^{\pm}$ states in ZnSe, as well as in the longitudinal relaxation; together these features indicate quite complicated dynamics. Because of the above site re-assignment for the dominant $Mu^0$ signal above 20–50 K, we are now required to re-examine all of our preliminary assignments for these features.

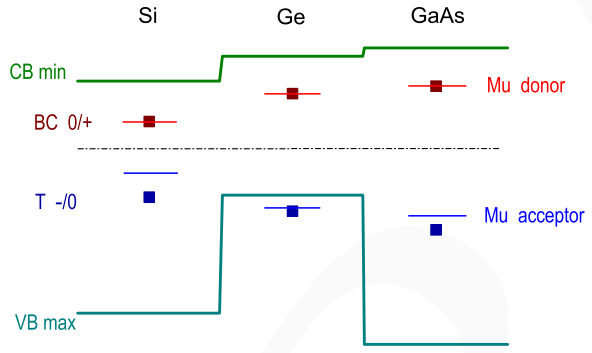


Fig. 1. Muonium defect levels determined for Si, Ge and GaAs. The data points are from experimental ionization energies related to the BC (donor) and T-site (acceptor) muonium states. Acceptor levels need correction for $Mu^0$ metastability, as shown, in order to compare with theory.

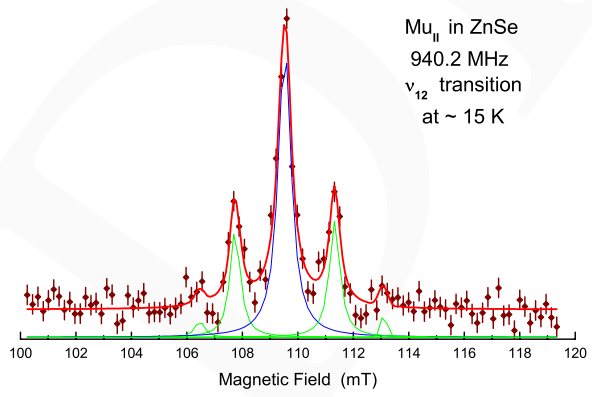


Fig. 2. Microwave resonance spectra from $Mu_{II}$ in ZnSe display an $I = 1/2$ nuclear hyperfine structure, identifying near neighbours as Se instead of Zn, implying a $T_{Se}$ site.

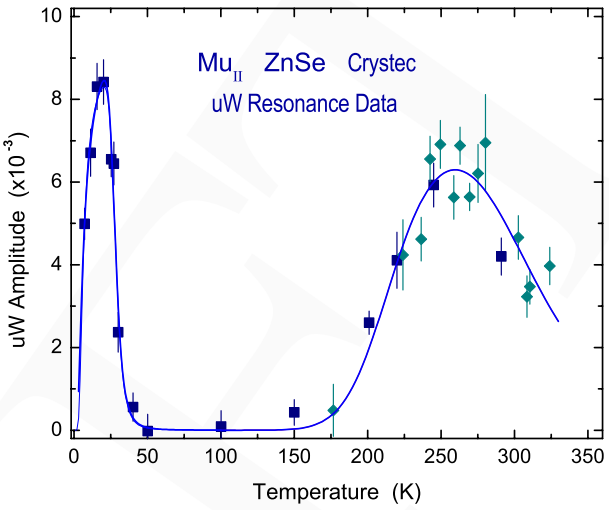


Fig. 3. Temperature dependent amplitudes from recent microwave resonance measurements on $Mu_{II}$ in ZnSe. The same spectra, shown in Fig. 2, occur at both peaks.

## Experiment 1005
## Optically induced dynamics and site changes in group IV semiconductors

*(I. Fan, K.H. Chow, Alberta)*

Positive muons implanted into Si can form either singly charged (diamagnetic) or neutral (paramagnetic) muonium (Mu) centres. In fact, it is now well-established that under certain conditions, and because of the short lifetime of the muon, multiple muonium centres can coexist in the material at low temperatures. In silicon, two distinct neutral muonium states are observed which are now commonly referred to as $Mu_T^0$ and $Mu_{BC}^0$. In addition, a diamagnetic state, likely $Mu^+$ and/or $Mu^-$, is seen. If free carriers are introduced into the sample, such as through doping, the various muonium centres can have dramatic interactions with them and undergo a variety of processes, including spin and charge exchange. Another method of introducing carriers into the system is to use light of the appropriate wavelength (i.e. energy) to photoexcite carriers across the bandgap of the semiconductor.

Experiments on muonium interacting with photoexcited carriers have produced many interesting results. In these semiconductors, spin and charge exchange with carriers are observed to take place, as are muonium site changes. The majority of the recent photoexcitation experiments are carried out at pulsed muon beam facilities and typically focus on studying the time-dependence of the muon polarization in a longitudinal magnetic field. If photoexcitation experiments are carried out at a continuous muon beam facility such as TRIUMF, additional/complementary

information is potentially available because the (high frequency) muon precession signatures associated with the various paramagnetic and diamagnetic muonium signals can be directly monitored. In addition, higher relaxation rates can be measured at continuous as compared to pulsed facilities.

However, it is not clear *a priori* that such experiments are possible at continuous facilities since the instantaneous amount of light that can be introduced into the sample is much smaller than at pulsed facilities. We illustrate in Fig. 1 that such experiments are indeed possible. These data were obtained in high resistivity silicon, and show that the diamagnetic muonium signal is heavily influenced by photoexcitation.

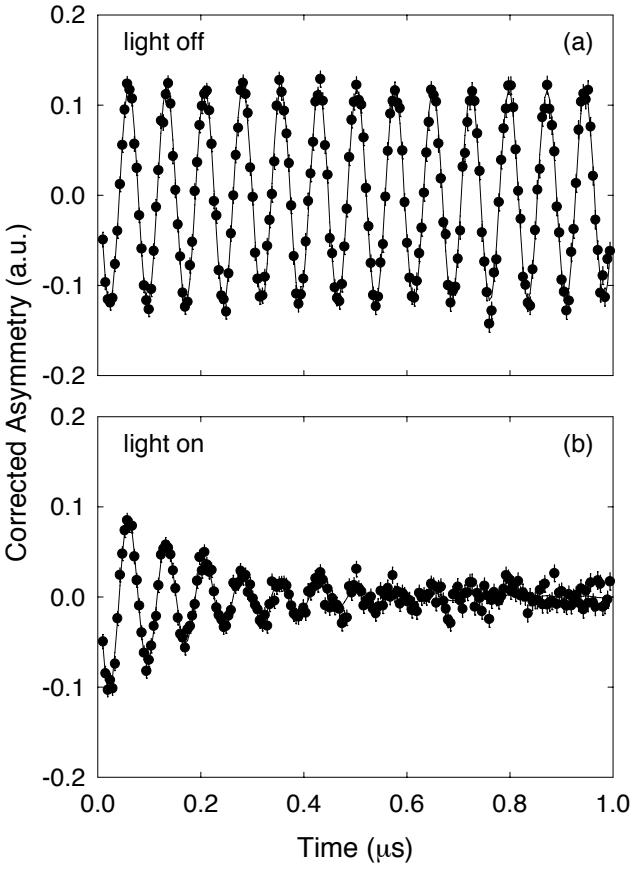


Fig. 1. Example of $Mu^+$ precession spectra with (a) light off, and (b) light on, with $B = 100$ mT and $T \approx 300$ K.

**Experiment 1006**
**Magnetism in $RECrSb_3$**
*(W.A. MacFarlane, UBC; K.H. Chow, Alberta)*

Lanthanide and actinide intermetallic compounds exhibit a rich variety of magnetic phenomena, from strong permanent magnetism to heavy fermion superconductivity. It is thus interesting to seek materials in this class with novel characteristics, particularly systems containing both $d$ and $f$ electrons. The objective of this experiment is to study newly discovered compounds in this class. We have carried out measurements on several members of the family $RECrSb_3$ (RE is a lanthanide), which exhibit interesting two dimensional transport properties and a complex magnetic phase diagram.

More recently, we have started to study the newly synthesized series $RE_{12}Co_5Bi$. The large size of the Bi atom in this material leads to a highly ordered structure with negligible substitutional disorder. Thus far, the only characterization of the magnetic state has been via macroscopic dc magnetization which shows Curie-Weiss behaviour in $M(T)$ down to an apparent ordering transition at 16 K, evident in a saturation of $M$. On closer inspection, $M(T)$ decreases slightly below the transition, exhibiting unusual features that are not currently understood. Interestingly, the magnetic ordering at 16 K does not show up in the electrical resistivity $\rho(T)$. Furthermore, there is a sharp kink in $\rho$ at about 110 K which is not evident in $M(T)$. It is important to determine whether these features are characteristic of the bulk state or whether they originate in dilute defects or rare impurity phases. To answer this, one requires a local, rather than macroscopic, probe such as the implanted muon.

While magnetic ordering is clearly evident by $\mu$SR below a bulk magnetic transition at $T_c \sim 30$ K, no zero field oscillations are observed, likely due to very high internal fields. Above the transition in the paramagnetic state, transverse and longitudinal field measurements indicate large amplitude fluctuating fields persist to quite high temperatures. Longitudinal field measurements reveal interesting behaviour with a relaxation rate $\lambda$ that is proportional to temperature times the magnetic susceptibility, consistent with Moriya's theory of nearly ferromagnetic metals. However, the proportionality constant appears to change abruptly, just at the temperature of the resistance anomaly at 110 K as shown in Fig. 1. Planned measurements will focus on the strongly anisotropic magnetic properties of these systems using single crystal samples.

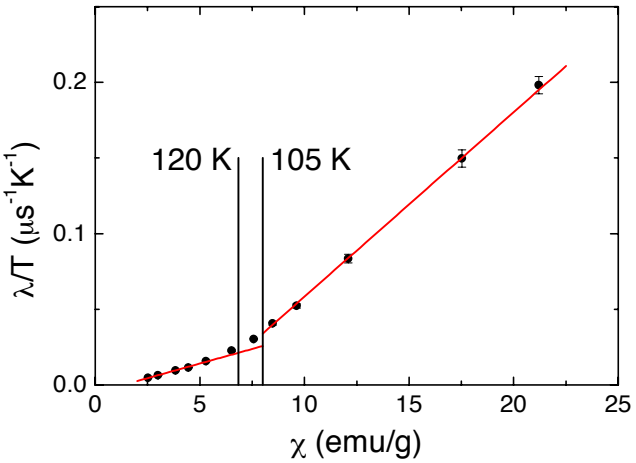


Fig. 1. The longitudinal field relaxation rate in $Ho_{12}Co_5Bi$ at 0.9 mT divided by the temperature vs. the susceptibility $\chi(T)$ with temperature as an implicit variable, here running between 300 K and 50 K. In the SCR picture the relationship should be linear. There are clearly two separate linear regimes with a crossover bracketed by the two vertical lines at ∼110 K.

## Experiment 1011
## $\mu$SR study of $LiHo_xY_{1-x}F_4$

*(G.M. Luke, McMaster)*

The transverse field Ising model is attractive for theoretical analysis of magnetic systems due to its simplicity comparing to other models (e.g. Heisenberg model). The Ising model is also interesting because it has been able to reproduce physically observed phenomena (e.g. magnetic glasses). Many times, this model is an approximation of real physical systems so, in order to fully test the predictions of the model, it is desirable to study systems with intrinsic Ising nature. $LiHo_xY_{1-x}F_4$ is thought to be a physical realization of the Ising model and it has been shown to be both an achievement and a challenge of the model. The physical behaviour of this system is rich and not yet completely investigated; it displays ferromagnetism, glassiness and a puzzling coherent phase which has been designated by some authors as an "anti-glass".

The crystal fields in $LiHo_xY_{1-x}F_4$ result in the $Ho^{3+}$ moments possessing an Ising electronic ground state ($\mu_{eff} = 7\ \mu_B$) with a distance of 9.4 K to the first excited crystal field level. The Ising ground state is further split by hyperfine interactions into eight doubly degenerate levels. The distance between hyperfine levels is ∼200 mK. Also, the ions interact mainly through magnetic dipolar fields [Chakraborty, *et al.*, Phys. Rev. **B70**, 144411 (2004)].

For $x = 1$ the system has a ferromagnetic ground state with $T_c = 1.53$ K. If magnetic holmium atoms are substituted by non-magnetic yttrium ones, randomness is introduced into the system and around $x = 0.5$ the ground state is that of a spin glass. Whether the glassy state coexists with the ferromagnetic one is still not known. If the system is further diluted, the low temperature behaviour is that of the previously mentioned anti-glass phase. $\chi_{AC}$ data taken in this phase suggest that, as the system cools down, its dynamical response tends to a single fluctuation rate. This is in contrast to the slowing down of the broad fluctuation distribution observed in glassy systems. Hence the term anti-glass [Reich *et al.*, Phys. Rev. Lett. **77**, 940 (1987)].

More experimental data are needed to have a clear phenomenological picture of the behaviour of this system at high dopings. With this in mind, we are using $\mu$SR to probe the magnetic properties of the diluted system at the microscopic level.

To our knowledge, all the measurements performed in the anti-glass phase had been done using a single specimen ($x = 0.045$ or 4.5% Ho concentration). Then, not only the experimental picture of the anti-glass phase needs to be rounded, but also a study of where in the phase diagram this anti-glass phase exists needs to be addressed.

Together with our collaborators at Waterloo University, we are studying the magnetic behaviour of three highly doped samples: $x = 0.08$, 0.045 and 0.018. In this report we present the data we have acquired in TRIUMF, as well as a partial analysis of it.

### Experimental procedure

Sample preparation was performed at McMaster University. Thin single crystal discs were aligned using a Laue camera, then they were cut using a water cooled diamond saw. The $\mu$SR measurements were performed in zero and longitudinal magnetic field (perpendicular to the Ising axis), and in a temperature range from 0.02 mK to 200 K. Scans from room temperature to 2 K were performed in a He flow cryostat at the M20 beam line; those from 10 K to 0.02 K were performed inside a dilution refrigerator at the M15 beam line. In M20 the samples were mounted in a low background sample holder using silver tape. In M15 they were mounted on a silver sample holder using Apiezon N grease. Longitudinal field runs were performed up to 1 T.

### Analysis of the data

The high level of dilution and the observed shape of the $\mu$SR signal in zero external magnetic field, motivated us to analyze our data by fitting a Lorenzian Kubo-Toyabe function in longitudinal field. This function, which has its origins in the stochastic theory of Kubo and Toyabe, assumes that the probability that a thermalized muon sees a given field has a Lorenzian shape and is characterized by the parameter "$a$". This function also assumes that the time correlation of

magnetic moments is Markovian ($\langle S(0)S(t)\rangle \ \alpha \ e^{-\nu t}$). Figures 1 and 2 present the fitted parameters at low longitudinal field for the three samples.

Even though high temperature data still need to be taken, Fig. 1 seems to indicate that the parameter $a$ increases in two stages. The first stage is from ≈0.1 K to ≈1 K, and the second from ≈1 K to ≈10 K. This last stage has the right temperature scale of the first excited crystal field level. We believe that this increase in relaxation is due to the depopulation of this level and the consequent increase of the magnetic moment of the ions. The origin of the low temperature increase on $a$ is not clear to us yet. It must be noted that, even though it has the right temperature scale of the hyperfine interaction, a slowing down of the nuclear magnetic moment can't produce such a big increase in the relaxation of the signal (the magnetic nuclear moment is 1000 smaller than the electronic one). One possibility is that small transverse dipolar fields can couple hyperfine levels with different Ising states, then the change in $a$ could be due to the depopulation of hyperfine levels with renormalized magnetic moments.

It is interesting to note that the fluctuation rate $\nu$ on Fig. 2 does not change very much in the explored temperature range. Still, there is a monotonic decrease of "$\nu$" as a function of $x$. This behaviour is similar to that of a spin liquid (persisting fluctuations down to base temperature). Figure 3 shows that, at base temperature, $\nu$ scales almost linearly with $x$. Now, the average magnetic interaction between the moments also scales linearly with $x$. Then it is possible that the fluctuation rate scales linearly with the average magnetic interaction. If this is true then, the persistent fluctuations down to base temperature might have its origin in a collective behaviour.

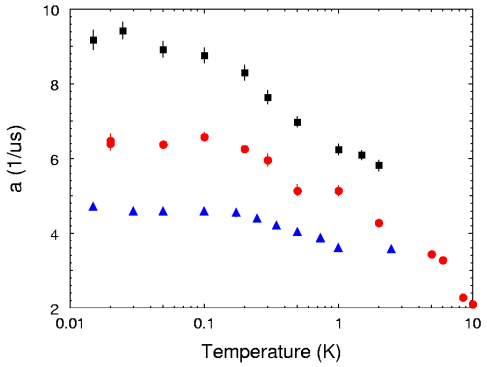


Fig. 1. Temperature dependence of $a$ in low longitudinal field for the $x = 0.08$ (black squares), 0.045 (red circles) and 0.018 (blue triangles). The magnitude of the external field is 4 G for the 0.08 sample, 15 G for the 0.045 and 4 G for the 0.018 one.

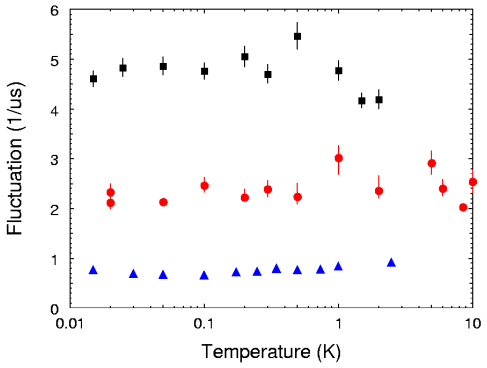


Fig. 2. Temperature dependence of $\nu$ in low longitudinal field for the $x = 0.08$ (black squares), 0.045 (red circles) and 0.018 (blue triangles). The magnitude of the external field is 4 G for the 0.08 sample, 15 G for the 0.045 and 4 G for the 0.018 one.

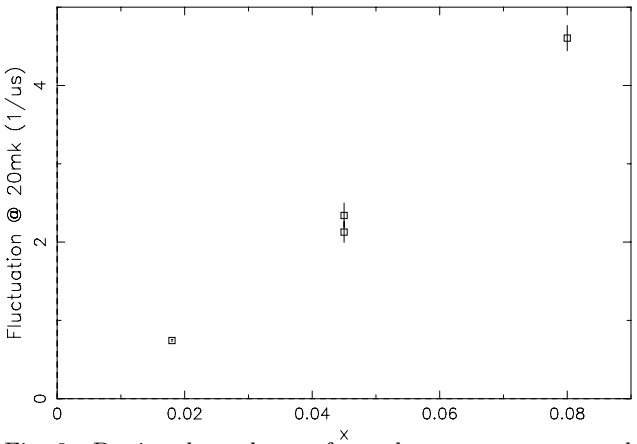


Fig. 3. Doping dependence of $\nu$ at base temperature and low longitudinal field.

**Conclusions**

We have found a narrowing of the magnetic field distribution as $x$ (the magnetic Ho concentration) is reduced. This effect might be associated with a renormalization of the Ho magnetic moments induced by dipolar transverse fields. Also we have observed persistent fluctuations of the magnetic moments down to base temperature (∼20 mK). These fluctuations seem to scale linearly with $x$.

**Experiment 1012**
**Organic free radicals under hydrothermal conditions**
*(P.W. Percival, SFU)*

There was little progress on Expt. 1012 in 2006, mostly due to technical problems. First, beam time originally allocated for the summer was postponed in favour of an installed experiment which had been delayed by the extended shutdown work in the T2 area. Secondly, a large part of the beam time taken in October suffered from very high background counts which resulted in unacceptably noisy spectra. This was eventually traced to a facility set-up error (incorrect arrangement of shielding inside the beam line).

Our plan had been to continue our study of acetone keto-enol tautomerism in superheated water by detecting and monitoring the muoniated radicals formed from aqueous solutions of $^{13}$C-enriched acetone. Given the technical problems, we decided not to risk the valuable sample and instead started a preliminary investigation of methyl ethyl ketone (MEK). At room temperature this molecule is essentially all in the keto form (the left-most structure in Fig. 1), but we expected to find evidence of enhanced enol formation at high temperature, as we have shown for acetone [Ghandi *et al.*, J. Am. Chem. Soc. **125**, 9594 (2003); Percival *et al.*, J. Am. Chem. Soc. **127**, 13714 (2005)]. The situation for MEK is more complicated than acetone because there are two possible enols and multiple potential sites of Mu addition, resulting in as many as five muoniated free radicals (**1**–**5**). In principle each radical can be identified from its muon level-crossing (LCR) spectrum, since each pair of muon and proton hyperfine constants gives rise to a distinct resonance.

We studied an aqueous solution of MEK at both low (30°C) and high (330°C) temperatures. The low-temperature signals were unambiguously assigned to the keto adduct (**5**), because only this radical has a low enough muon hyperfine constant to account for the pair of LCR resonances detected near 1 kG. At high temperature we found six resonances in the 8–11 kG region. The problem is, the four enol adducts (**1**–**4** are expected to produce only five signals here, with a further two at much higher fields. The distinction between the two groups of signals is due to the sign of the proton hyperfine constant, which is negative for H atoms directly bound to a radical centre (the dots on specific carbon atoms in the radical structures), but positive for H atoms adjacent to the radical centre.

At this stage it is not clear if the unexpected number of resonances is due to inequivalence of H atoms in a particular $CH_2$ or $CH_3$ group, or if there is some additional molecule in the system, perhaps as a result of decomposition or transformation of MEK. One possible strategy for future investigation is to simplify the situation by investigating the symmetrical diethyl ketone.

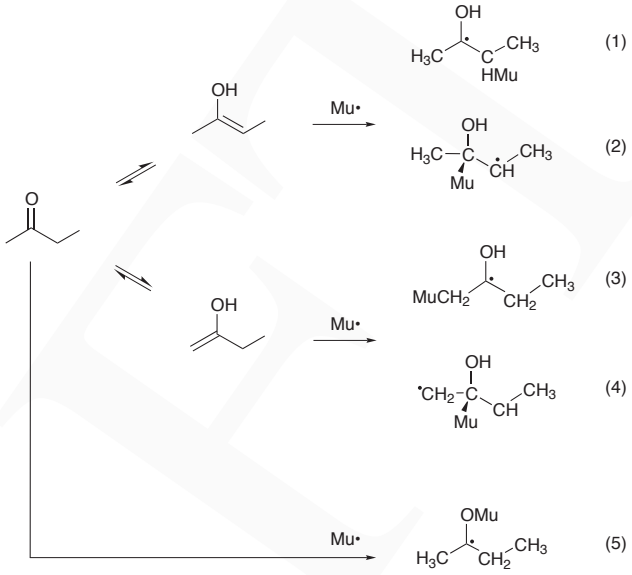


Fig. 1. Competitive formation of muoniated radicals by addition of muonium to enol and keto tautomers of methyl ethyl ketone in water.

**Experiment 1016**
**Muonium in isotopically enriched Si and Ge**
*(K.H. Chow, Alberta)*

Hydrogen is an important impurity in many semiconductors, including Si and Ge. Information on the isolated states of hydrogen come, albeit indirectly, from studies of muonium. However, the dynamics and reactivity of the isolated states of muonium are very difficult to study in systems such as Si and Ge. One interesting method to enable such investigations is to use materials that are isotopically enriched with nuclei with spin; for example, $^{29}$Si in silicon, etc. At the same time, we attempt to develop a new technique to improve our ability to directly study non-enriched systems. This new technique is based on collecting the integrated signal, hence enabling us to use the full incoming muon rate (as opposed to standard time-differential techniques). The data are collected as a function of field near zero applied field. At very low applied fields, the dipolar interaction dominates while at high fields, the Zeeman interaction is the dominant interaction. An example of such a signal is shown in Fig. 1.

As a demonstration of the power of this technique, Ag is investigated. Figure 2 shows a comparison of data obtained using this technique versus that using zero-field, taken in samples of high-purity Ag at the ISIS facility. Recall that ISIS is able to study very slow relaxations. The agreement is reasonably good; both sets of data appear to show an abrupt change in behaviour between 100 and 150 K.

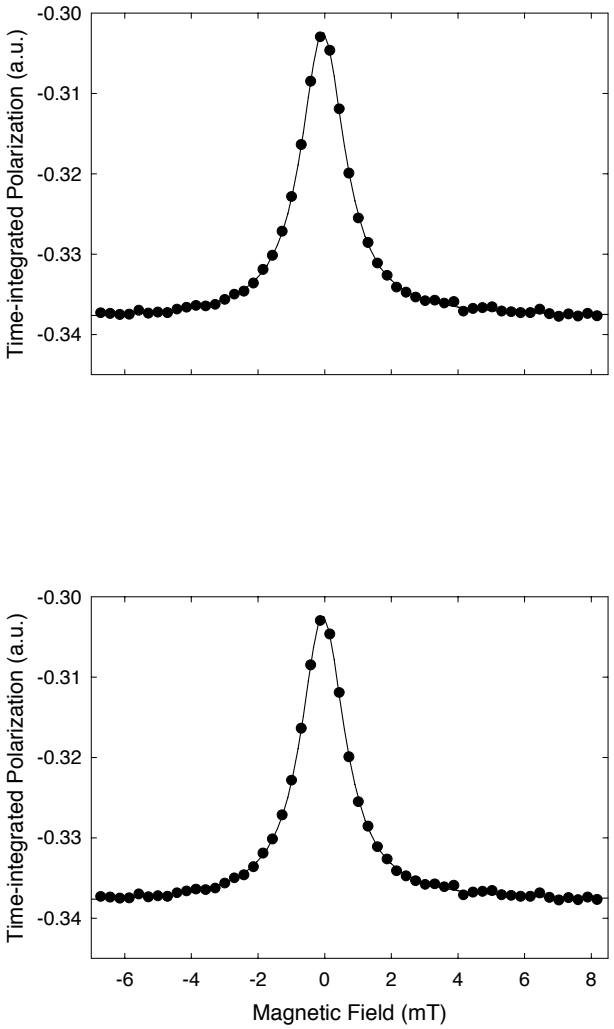


Fig. 2. (a) Fitted Lorentzian amplitude, and (b) zero field relaxation $\Delta$ in samples of high-purity Ag. Solid lines are guides to the eye.

**Experiment 1017**
**Quasicrystals**
*(J. Sugiyama, Toyota CRDL Inc.; J.H. Brewer, UBC-TRIUMF)*

The purpose of Expt. 1017 is to detect a short-range order and/or an accompanying critical phenomenon around a spin-glass-like transition in magnetic quasicrystals by $\mu^+$SR.

Here, quasicrystals have highly ordered atomic structure but have neither translational symmetry nor unit-cell. Interestingly, they also have five-, eight-, ten- or twelve-fold symmetry, which is usually forbidden in a periodic lattice. Among several quasicrystals, the *i*-Zn-Mg-*RE* and Cd-Mg-*RE*, where *RE* denotes rare earth elements, are among the rare cases which exhibit magnetism due to localized $4f$-electrons [Belin and Traverse, J. Phys. Cond. Matter **3**, 2157 (1991); Niikura *et al.*, Phil. Mag. Lett. **69**, 351 (1994); Hattori *et al.*, J. Phys. Cond. Matter **7**, 2313 (1995); *ibid.* **7**, 4183 (1995); Fisher *et al.*, Phys. Rev. **B59**, 308 (1999); Guo *et al.*, Jpn. J. Appl. Phys. **39**, L770 (2001)]. Actually, the effective magnetic moments in *i*-Zn-Mg-*RE* and *i*-Cd-Mg-*RE* estimated by $\chi(T)$ measurements are reported to be almost equivalent to those of free $RE^{3+}$ ions. Also, the $\chi(T)$ measurements suggested the existence of a spin-glass-like transition in the temperature range between 15–1.8 K (freezing temperature $T_f$ depends on *RE*) in *i*-Zn-Mg-*RE* and *i*-Cd-Mg-*RE*. Recent neutron scattering experiments on *i*-Zn-Mg-Ho indicated that the short-range magnetic order with $T_f$ = 1.95 K is induced by a magnetic modulation with six-dimensional hyper-cubic symmetry [Sato *et al.*, Phys. Rev. **B61**, 476 (2000)].

Earlier $\mu^+$SR results by Noakes *et al.* on *i*-ZnMgTb and *i*-ZnMgGd [Noakes *et al.*; Phys. Lett. **A238**, 197 (1998); Phys. Rev. **B65**, 132413 (2002)], for which spin-glass-like freezing was reported to occur at ($T_f$ = 5.8 K) and ($T_f$ = 5.5 K) respectively, were analyzed in terms of concentrated disordered magnetism, with the differences between the Tb and Gd results explained with reference to crystalline electric field (CEF) effects. We report here our first $\mu^+$SR results on *i*-ZnMgHo, *i*-CdMgHo, and *i*-CdMgGd in zero field (ZF), weak transverse field (wTF), and longitudinal fields (LF) of up to several T.

Alloys of three QCs ($Zn_{60}Mg_{31}Tb_9$, $Zn_{60}Mg_{31}Dy_9$, and $Zn_{60}Mg_{31}Ho_9$) were prepared at ISSP, University of Tokyo, by melting constituent elements in an Ar gas flow and then annealing at 673 K for 250 hours. The preparation and characterization of these QCs are reported in greater detail elsewhere [Sato *et al., op. cit.*]. The shapes of the sample for the $\mu^+$SR experiment were $\sim 8 \times 8 \times 1$ mm$^3$ thin plates cut from the ingot rod of the QC. Four plates were set on the Ag sample holder for the Helios spectrometer on the M20 surface muon channel and were measured in the temperature $T$ range between 2 K and 100 K.

Figure 1 shows ZF-$\mu^+$SR time spectra at 2.2, 10.0, and 12.5 K for the *i*-ZnMgTb sample. It should be noted that the appearance of the first minimum – i.e. the Kubo-Toyabe type behaviour due to randomly oriented Tb moments – is clearly different for the past results, for which the ZF-spectrum is well explained by a power exponential relaxation ($\exp(-(\lambda t)^\beta)$) [Noakes *et al., op. cit.*]. The full spectra were thus fitted using a combination of the following three signals: a dynamic Gaussian Kubo-Toyabe function $G^{\mathrm{DGKT}}(t, \Delta, \nu)$ and two exponential relaxation signals, which relax slowly. Since one of the two exponential relaxation signals was almost time independent, this signal is determined to be coming from the muons stopped outside the sample,

mainly in the silver holder:

$$A_0\,P(t) = A_{\rm KT}G^{\rm DGKT}(t,\Delta,\nu)\,e^{-\lambda_{\rm KT}t} + A_{\rm slow}\,e^{-\lambda_{\rm slow}t} + A_{\rm Ag}\,e^{-\lambda_{\rm Ag}t}$$

where $A_0$ is the empirical maximum muon decay asymmetry, $A_{\rm KT}$, $A_{\rm slow}$ and $A_{\rm Ag}$ are the asymmetries associated with the three signals, $\lambda_{\rm KT}$, $\lambda_{\rm slow}$, and $\lambda_{\rm Ag}$ are their relaxation rates, $\Delta$ is the static width of the local frequencies at the muon sites in the aperiodic lattice, and $\nu$ is the field fluctuation rate. Note that $\lambda_{\rm KT}$ has a finite value when the first minimum disappears. This is consistent with the fact that, in the fast fluctuation limit ($\nu \gg \Delta$) in zero field, $G^{\rm DGKT}(t,\Delta,\nu) \sim \exp(-\lambda t)$ [Kalvius *et al.*, *Handbook on the Physics and Chemistry of Rare Earths*, eds. Gschneidner, Jr. *et al.* (North-Holland, Amsterdam, 2001) v.32].

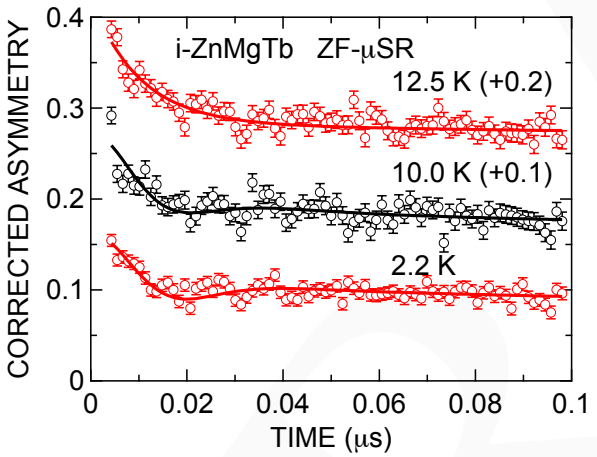


Fig. 1. ZF-$\mu^+$SR time spectra of $i$-Zn-Mg-Tb ($T_f = 5.8$ K) at 2.2, 10, and 12.5 K. Each spectrum is offset by 0.1 for clarity of the display. The solid lines represent the fits using the equation.

Figures 2(a–c) show the $T$ dependence of $\Delta$ and $\nu$ for $i$-ZnMgTb, $i$-ZnMgDy, and $i$-ZnMgHo obtained from the ZF spectra. Interestingly, both $\Delta$ and $\nu$ have a finite value below ∼30 K for $i$-ZnMgTb and $i$-ZnMgDy, and below ∼5 K for $i$-ZnMgHo, although $T_f = 5.8$ K for $i$-ZnMgTb, 3.6 K for $i$-ZnMgDy, and 1.95 K for $i$-ZnMgHo. Furthermore, as $T$ decreases from 30 K, the $\nu(T)$ curve seems to show a rapid decrease below $T_f$, being consistent with the result of the 2005 experiment on $i$-ZnMgHo at M15 with DR. This suggests that $\mu^+$SR detects the critical slowing down of the field fluctuation rate at $T_f$, as expected.

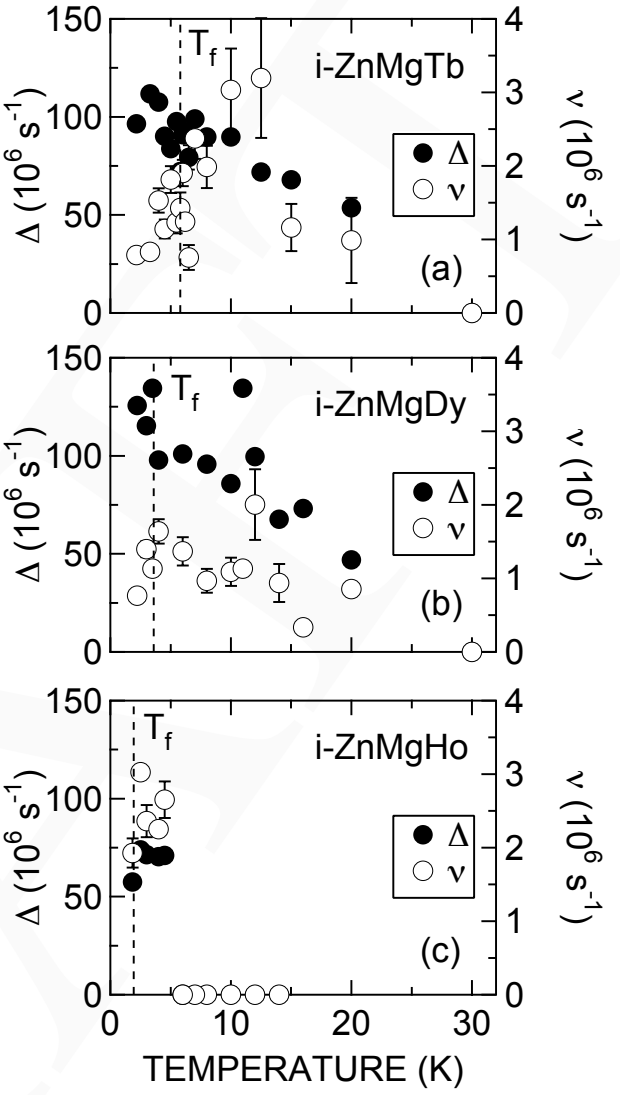


Fig. 2. Temperature dependence of the field distribution width $\Delta$ and the field fluctuation rate $\nu$ for (a) $i$-ZnMgTb ($T_f = 5.8$ K), (b) $i$-ZnMgDy ($T_f = 3.6$ K), and (c) $i$-ZnMgHo ($T_f = 1.95$ K). The broken lines represent $T_f$.

On the other hand, $\Delta$ is naturally due to the magnetic moments caused by localized $4f$-electrons of $RE$. According to the $\chi$ measurements on $i$-ZnMg$RE$ [Hattori *et al., op. cit.*], the effective magnetic moment ($\mu_{\rm eff}$) was reported as 10.29 $\mu_{\rm B}$ for $i$-ZnMgTb, 10.83 $\mu_{\rm B}$ for $i$-ZnMgDy, and 10.08 $\mu_{\rm B}$ for $i$-ZnMgHo. Since the spatial structures of the three QCs are essentially equal to each other, muons are expected to sit at equivalent sites in the three QCs. As a result, the magnitude of $\Delta$ is thought to be directly correlated with the $\mu_{\rm eff}$ of $RE$, if we ignore the crystalline electric field (CEF) effects. Actually, the order of magnitude of $\Delta$(2 K) corresponds with the order of $\mu_{\rm eff}$ for these three QCs.

The overall picture of the current QCs is as follows.

Above 30 K, the localized $4f$ moments are fluctuating too fast to be seen by $\mu^+$SR. As a result, since $\nu \gg \Delta$, the ZF-spectrum is mainly fitted by an exponential relaxation function (or a power exponential relaxation function). As $T$ decreases from 30 K (in the case of $i$-ZnMgTb and $i$-ZnMgDy), $\nu$ decreases to such a low value (i.e. slow fluctuations) that muons experience the Kubo-Toyabe type relaxation. The monotonic increase in $\Delta$ with lowering $T$ is probably due to the CEF effects, for the detail is still unknown. This is because the magnitude of $\Delta$ is considered to be $T$-independent at low $T$, if $\nu \sim \Delta$ and the magnitude of the $4f$ moments do not depend on $T$. With further lowering $T$, the $4f$ moments freeze with random-orientation at $T_f$, inducing the rapid decrease in $\nu$.

## Experiment 1032
## Penetration depth and time reversal symmetry breaking in filled-skutterudite $\mathbf{Pr(Os_{1-x}Ru_x)_4Sb_{12}}$

*(D.E. MacLaughlin, California, Riverside)*

A number of $\mu$SR studies of Pr-based filled skutterudites have been reported. In $PrOs_4Sb_{12}$, ZF-$\mu$SR spin relaxation data at low temperatures could be fit by a product of an exponential damping factor $\exp(-\Lambda t)$ and the Kubo-Toyabe (K-T) functional form expected for a quasistatic Gaussian field distribution. The exponential damping was determined by LF-$\mu$SR measurements to be due to dynamic fluctuations of an additional component of the local field $\mathbf{H}_{\rm loc}$ at muon sites. In the normal state above $T_c$ the quasistatic field distribution was attributed to dipolar interactions between $\mu^+$ spins and neighbouring (principally $^{121}$Sb and $^{123}$Sb) nuclear magnetic moments. The origin of the dynamic relaxation (damping) was not clear, although $4f$-electron dynamics associated with the small CEF splitting were noted as a possible mechanism. An increase in the quasistatic relaxation rate $\Delta$ was observed below $T_c$, and interpreted as evidence for time-reversal symmetry breaking in the superconducting state of $PrOs_4Sb_{12}$.

We have carried out LF-$\mu$SR experiments in $Pr(Os_{1-x}Ru_x)_4Sb_{12}$, $x$ = 0.05, 0.1, 0.2, 0.6, and 1.0, and $(Pr_{1-y}La_y)Os_4Sb_{12}$, $y$ = 0.2, 0.4, 0.6, and 0.8, to determine the origin of this exponential damping and as an auxiliary characterization of the normal states of these alloys. Data were taken at the M15 channel at TRIUMF in 2005, and also at KEK, Tsukuba, Japan in 2005 and at ISIS, Chilton, U.K. in 2006. We argue that the damping is due to enhancement of $^{141}$Pr nuclear magnetism via its intra-atomic hyperfine coupling to the $Pr^{3+}$ $4f$ electrons. This coupling induces a Van Vleck-like admixture of low-lying $Pr^{3+}$ magnetic CEF-split excited states into the singlet ground state, which greatly enhances the effect of $^{141}$Pr nuclear moments on $\mu^+$ spin relaxation by increasing both the $^{141}$Pr-$\mu^+$ dipolar coupling (by a factor of $\sim$20) and the $^{141}$Pr spin-spin interaction strength (by a factor of at least $\sim$400). This "hyperfine enhancement" accounts qualitatively for the observed damping, and we conclude that electron spin dynamics, $4f$ or otherwise, are not directly involved.

**Longitudinal-field muon spin relaxation**

LF-$\mu$SR experiments were performed in weak longitudinal fields $H_L$ in the normal state just above $T_c$, to confirm the dynamic nature of the exponential damping. This procedure makes use of the fact that for $H_L$ of the order of or greater than the rms magnitude of (quasistatic) $\mathbf{H}_{\rm loc}$ the resultant field is nearly parallel to the initial $\mu^+$ spin direction, so that the precession that causes quasistatic relaxation does not take place and the $\mu^+$ spin polarization is nearly time-independent. This phenomenon is called "decoupling," and does not occur for dynamic relaxation if the mechanism for the latter is field-independent. Thus LF-$\mu$SR measurements help to determine whether the observed ZF relaxation is due to static or dynamic contributions to $\mathbf{H}_{\rm loc}$. In addition, the dependence of the damping rate $\Lambda$ on $H_L$ yields statistical properties (rms amplitude, correlation time) of the fluctuating field.

Representative LF-$\mu$SR spectra are shown in Fig. 1. In zero field the asymmetry at long times is expected to approach 1/3 of its initial value $A$ for any distribution of quasistatic local fields. In Pr-based samples, however, the zero-field value of the asymmetry at long times is typically much lower than $A/3$. In the case of $PrRu_4Sb_{12}$ this can be seen in Fig. 1(c) (circles). Such behaviour is evidence that the exponential damping is dynamic.

The "damped Gaussian K-T" function

$$G(t) = \exp(-\Lambda t)\, G_z^{\rm KT}(\Delta, t) \qquad (4)$$

(solid curve) was fit to our LF-$\mu$SR data. Here $\Lambda$ is the exponential damping rate, and $G_z^{\rm KT}(\Delta, t)$ is the quasistatic K-T function in longitudinal field $H_L$ that describes $\mu^+$ spin relaxation by randomly-oriented quasistatic $\mu^+$ local fields with Gaussian distributions of their Cartesian components. This function is characterized by the K-T relaxation rate $\Delta$; the rms width of the field component distributions is $\Delta/\gamma_\mu$, where $\gamma_\mu$ is the $\mu^+$ gyromagnetic ratio.

The field dependence of $\Lambda$ from fits such as those shown in Fig. 1 is shown in Fig. 2 for several alloys. If the exponential damping were due to a (Lorentzian) distribution of quasistatic contributions to $\mathbf{H}_{\rm loc}$, the observed ZF value of $\Lambda$ leads to an estimate $\Lambda/\gamma_\mu \sim$ 1 Oe for the spread of these local fields. Then an applied longitudinal field of order 10 Oe should nearly

decouple these local fields and there should be almost no relaxation. But it can be seen from Fig. 2 that $\Lambda$ is reduced by only $\sim$25% for $H_L = 10$ Oe. This is good evidence that dynamic relaxation is involved, thus corroborating the conclusion reached above from the absence of a "1/3 tail." The temperature dependence of $\Lambda$ (not shown) is small, which suggests that nuclear magnetism (rather than electronic spin fluctuations) is the source of the dynamic relaxation. The obvious candidate is fluctuating hyperfine-enhanced $^{141}$Pr nuclear magnetism as discussed above.

**Relaxation by fluctuating $^{141}$Pr nuclear spins**

Before analyzing the relaxation data, we discuss the choice of Eq. (1). In LF-$\mu$SR, fluctuations of $\mathbf{H}_{\rm loc}$ are often treated using the "dynamic K-T" relaxation function, in which $\mathbf{H}_{\rm loc}$ fluctuates as a whole with a single correlation time. Such a procedure is not appropriate in the present experiments, however; a quasistatic contribution to $\mathbf{H}_{\rm loc}$, due mainly to Sb nuclear dipolar fields, is also present, so that $\mathbf{H}_{\rm loc}$ is the sum of quasistatic and rapidly-fluctuating components. The near equality (not shown) of the quasistatic rates $\Delta$ for $PrOs_4Sb_{12}$ and $LaOs_4Sb_{12}$ (where there are no $4f$ electrons) is strong evidence for this situation. In addition, significantly better fits to zero-field data are obtained from damped quasistatic K-T fits (reduced $\chi^2$ typically $\sim$1.1) than from dynamic K-T fits ($\chi^2 \sim 1.4$). Thus on the local scale $\mu^+$ spin states are split into Zeeman levels by the quasistatic component of $\mathbf{H}_L + \mathbf{H}_{\rm loc}$, and the $\mu^+$ spin polarization amplitude decays due to transitions induced between these Zeeman levels by the fluctuating component of $\mathbf{H}_{\rm loc}$. This situation is modelled by a damped quasistatic relaxation function of the form of Eq. (1).

Hayano *et al.* have treated LF-$\mu$SR and TF-$\mu$SR relaxation due to dipole-coupled fluctuating nuclear spins based on the theory of magnetic resonance absorption formulated by Kubo and Tomita. Their calculation applies to the present experiments when modified to include hyperfine enhancement of the $^{141}$Pr nuclear spins. This is accomplished by replacing the bare $^{141}$Pr gyromagnetic ratio $\gamma_{\rm Pr}$ by $\gamma_{\rm Pr}(1+K)$, where $K$ is the hyperfine enhancement factor (i.e., the $^{141}$Pr Knight shift), assumed isotropic for the tetrahedral Pr site. Assuming the rapid-fluctuation limit $\sigma_{\rm VV}\tau_c \ll 1$ (since otherwise an exponential relaxation function would not be expected), the relaxation rate is found to be of the form

$$\Lambda = \frac{\sigma_{\rm VV}^2}{2}\left\{\frac{\tau_c}{1+[\gamma_{\rm Pr}(1+K)-\gamma_\mu]^2H_L^2\tau_c^2} + \frac{3\tau_c}{1+(\gamma_\mu H_L\tau_c)^2} + \frac{6\tau_c}{1+[\gamma_{\rm Pr}(1+K)+\gamma_\mu]^2H_L^2\tau_c^2}\right\}. \quad (5)$$

Here $\sigma_{\rm VV}$ is the high-field $\mu^+$ Van Vleck relaxation rate due to $^{141}$Pr dipolar fields (used as a measure of the rms amplitude of these fields), $\tau_c$ is the correlation time of the $^{141}$Pr spin fluctuations due to their mutual spin-spin interactions, and a powder average has been taken. Equation (2) gives the contributions to $\Lambda$ of both longitudinal and transverse $^{141}$Pr spin fluctuations, which are assumed to have a common correlation time $\tau_c$.

From Fig. 2 it can be seen that the field dependence of $\Lambda$ is well fit by Eq. (2) except perhaps for $Pr_{0.2}La_{0.8}Os_4Sb_{12}$, where the damping is weak because of the low Pr concentration. We find that the form of this relation does not determine $K$ well compared to the other fitting parameters, so that we obtain $K$ independently from the observed low-temperature molar susceptibility $\chi_{\rm mol}$ of the Pr ions and fix it in the fitting. This is done by means of the standard relation $K = a_{\rm hf}\chi_{\rm mol}$, where $a_{\rm hf} = 187.7$ mole emu$^{-1}$ is the Pr atomic hyperfine coupling constant. The calculated values of $K$ together with the fit values of $\sigma_{\rm VV}$ and $\tau_c$ are given in Table I.

Next we compare our results with the expected relaxation behaviour based on the model of Hayano *et al.* We first calculate the "unenhanced" powder-average $\mu^+$ Van Vleck relaxation rate $\sigma_{\rm VV}^0$ (i.e., assuming only the bare $^{141}$Pr gyromagnetic ratio) from a standard lattice sum for the candidate $\mu^+$ site (0, $\frac{1}{2}$, 0.15) (12$e$ in Wyckoff notation) in the filled-skutterudite structure (space group $Im\bar{3}$). The unenhanced correlation time $\tau_c^0$ is taken to be the inverse of the zero-field-like-spin Van Vleck rate for the (unenhanced) $^{141}$Pr nuclear spin system, which is calculated from a similar lattice sum. The hyperfine-enhanced values of these parameters are then

$$\sigma_{\rm VV} = \sigma_{\rm VV}^0(1+K) \quad \text{and} \quad \tau_c = \tau_c^0/(1+K)^2\,; \quad (6)$$

in both cases the dependence on $K$ comes solely from the hyperfine enhancement of $\gamma_{\rm Pr}$. The calculated values of $\sigma_{\rm VV}$ and $\tau_c$ are also given in Table I.

The inequality $\sigma_{\rm VV}\tau_c \ll 1$ required for our analysis is satisfied by the data, at least approximately. It can be seen that the fit values of $1/\tau_c$ generally exceed the calculated values, sometimes as much as an order

of magnitude. This may be an indication that the assumption that the $^{141}$Pr-$\mu^+$ and $^{141}$Pr-$^{141}$Pr interactions are purely dipolar is not valid; RKKY interactions may play an important role. Then $1/\tau_c$ could be increased considerably. In addition, the calculation of $\sigma_{VV}$ depends on the assumed $\mu^+$ stopping site, which has not been determined definitively; indeed, there may be more than one stopping site in $PrOs_4Sb_{12}$, as evidenced by the observation of two resonances in high-field TF-$\mu$SR. Given these caveats the qualitative agreement can be regarded as satisfactory.

Figure 3 gives the Ru and La concentration dependencies of the zero-field relaxation rate $\Lambda(0)$ extrapolated to $T = 0$. We see that $\Lambda(0)$ decreases linearly as we dilute the Pr with La ions, as expected. This strengthens our conclusion that the dynamic relaxation is due to $^{141}$Pr nuclear magnetism. For an undiluted Pr sublattice, one finds $\Lambda(0) = 5\sigma_{VV}^2\tau_c$ from Eq. (2). Therefore, from Eq. (3) there should be no $K$ dependence of $\Lambda(0)$; i.e., no dependence on Ru concentration. It can be seen in Fig. 3(b), however, that $\Lambda$ increases slightly from the end compound $PrOs_4Sb_{12}$ with Ru doping, and decreases again in the other end compound $PrRu_4Sb_{12}$. This behaviour, which is not well understood, will be investigated in future experiments over a wider range of Ru doping.

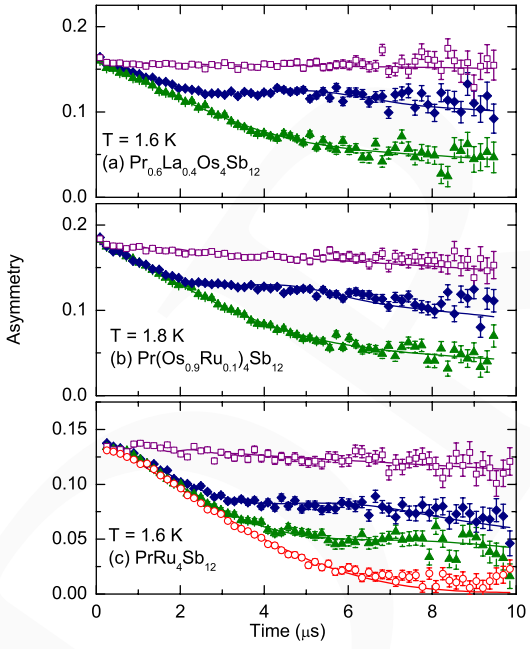


Fig. 1. Representative ZF- and LF-$\mu$SR spin polarization decay functions. (a) $Pr_{0.6}La_{0.4}Os_4Sb_{12}$. Triangles: $H_L = 5.9$ Oe. Diamonds: $H_L = 16.1$ Oe. Squares: $H_L = 121$ Oe. (b) $Pr(Os_{0.9}Ru_{0.1})_4Sb_{12}$. Triangles: $H_L = 5.3$ Oe. Diamonds: $H_L = 16.0$ Oe. Squares: $H_L = 75.6$ Oe. (c) $PrRu_4Sb_{12}$. Circles: $H_L = 0$ Oe. Triangles: $H_L = 6.3$ Oe. Diamonds: $H_L = 10$ Oe. Squares: $H_L = 63$ Oe. Curves: fits to the damped quasistatic K-T function in longitudinal field (Eq. (1), see text).

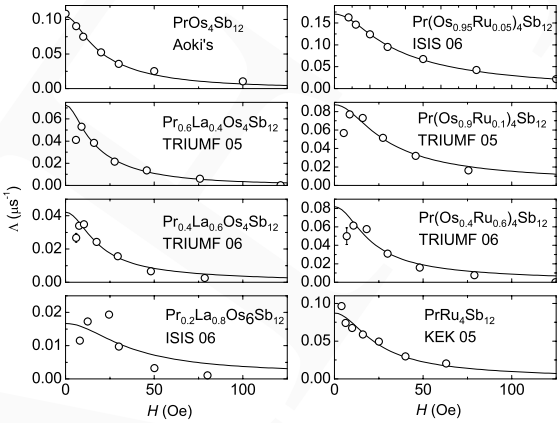


Fig. 2. Exponential damping rate $\Lambda$ vs. longitudinal applied field $H_L$ for $Pr_{1-y}La_yOs_4Sb_{12}$, $y = 0$, 0.4, 0.6, and 0.8; and $Pr(Os_{1-x}Ru_x)_4Sb_{12}$, $x = 0.05$, 0.1, 0.6, and 1.0. Curves: fits to Eq. (2).

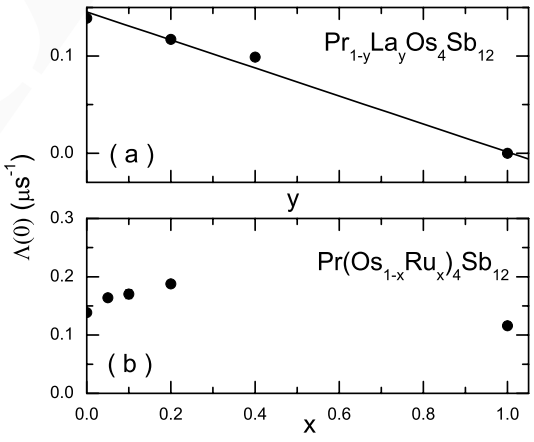


Fig. 3. Concentration dependence of zero-field low-temperature exponential damping rate $\Lambda(T \to 0)$ in (a) $Pr_yLa_{1-y}Os_4Sb_{12}$ and (b) $Pr(Os_xRu_{1-x})_4Sb_{12}$.

Table I. Parameters from fits and calculation of longitudinal field dependence of relaxation rate $\Lambda$ to Eq. (2) for alloys: $PrOs_4Sb_{12}$, $Pr_{1-y}La_yOs_4Sb_{12}$ ($y$ = 0.4, 0.6, and 0.8), $Pr(Os_{1-x}Ru_x)_4Sb_{12}$ ($x$ = 0.05, 0.1, and 0.6), and $PrRu_4Sb_{12}$. $\sigma_{VV}$: Van Vleck relaxation rate due to fluctuating local field. $\tau_c$: correlation time. $K_\chi$: Hyperfine enhancement factor (Knight shift) calculated from the observed molar susceptibility.

| Alloy | $K_\chi$ | $\sigma_{VV}$ ($\mu s^{-1}$) | | $\tau_c$ ($\mu$s) | |
|---|---|---|---|---|---|
| | | fit | calc. | fit | calc. |
| $PrOs_4Sb_{12}$ | 19.7 | 0.26(1) | 0.34 | 0.31(2) | 1.31 |
| $Pr_{0.6}La_{0.4}Os_4Sb_{12}$ | 18.1 | 0.20(0) | 0.25 | 0.38(3) | 1.98 |
| $Pr_{0.4}La_{0.6}Os_4Sb_{12}$ | 7.13 | 0.14(1) | 0.085 | 0.44(7) | 13.36 |
| $Pr_{0.2}La_{0.8}Os_4Sb_{12}$ | 9.39 | 0.013(3) | 0.077 | 0.2(1) | 11.57 |
| $Pr(Os_{0.95}Ru_{0.05})_4Sb_{12}$ | 15.9 | 0.43(1) | 0.28 | 0.19(1) | 1.96 |
| $Pr(Os_{0.9}Ru_{0.1})_4Sb_{12}$ | 12.2 | 0.28(1) | 0.22 | 0.23(3) | 3.22 |
| $Pr(Os_{0.4}Ru_{0.6})_4Sb_{12}$ | 7.51 | 0.20(1) | 0.14 | 0.4(1) | 7.66 |
| $PrRu_4Sb_{12}$ | 6.76 | 0.22(1) | 0.13 | 0.35(6) | 9.19 |

**Experiment 1036**
**$\beta$-NMR study of single molecule magnets mono-layers**
*(Z. Salman, Oxford; R.F. Kiefl, UBC)*

The use of nanoscale magnets for technological applications such as information storage or quantum computing requires monodisperse magnets that can be addressed individually. A major step towards achieving this goal came recently with the discovery of molecules that function as identical magnets, and the ability to deposit a monolayer of these molecules on a suitable substrate. At low temperatures these single molecule magnets (SMMs) exhibit fascinating quantum mechanical behaviour that dramatically affects macroscopic properties such as magnetization. These include the observation of quantum tunnelling of the magnetization (QTM), topological quantum phase interference, and quantum coherence. However, the small quantity of magnetic material present in a monolayer (or submonolayer) implies that it is virtually impossible to accurately determine their magnetic properties with conventional bulk techniques. However, depth-resolved $\beta$-detected NMR ($\beta$-NMR), which has $\approx 10^{13}$ orders of magnitude higher sensitivity compared to conventional NMR, is well-suited for studying such systems.

The experiments reported here were performed on two different samples. Sample 1 was prepared using a three-step process: 1) grafting of methyl ester of 10-undecanoic acid on a H-terminated Si(100) substrate, 2) hydrolysis of the ester group, and 3) ligand exchange between $[Mn_{12}O_{12}\text{-}(OAc)_{16}(H_2O)_4]\cdot H_2O\cdot 2AcOH$ and the grafted undecanoic acid to anchor the $Mn_{12}$ SMMs to the organic layer. A schematic of sample 1 is shown in Fig. 1(a). Sample 2 is an identically prepared Si substrate, i.e. following step 1 only. It is used as a control sample in order to confirm that the effects measured in 1 are solely due to the $Mn_{12}$. The resonance lines of $^8$Li were measured at various temperatures and implantation energies in both samples in an external magnetic field $H_0 = 6.55$ T.

The $\beta$-NMR spectra were measured by implanting the $^8$Li beam at different energies in the Si substrate below the $Mn_{12}$ monolayer. An example of the stopping profile of the implanted $^8$Li at two different energies is shown in Fig. 1(a). At $E = 1$ keV, where most of the $^8$Li stop within 10 nm of the surface of Si, the dipolar field from the $Mn_{12}$ moments is large. However, at $E = 28$ keV the average $^8$Li implantation depth is $\sim$250 nm, and the dipolar field at this depth is negligible; hence, the local field experienced by the $^8$Li is simply the applied uniform field $H_0$. As a result the measured resonance line at 1 keV is significantly broadened compared to that measured at 28 keV, as clearly seen in Fig. 1(b) at $T = 3.2$ K. Furthermore, the resonance measured in sample 2 at $E = 28$ keV and $T = 3.2$ K is identical to that measured in sample 1 under the same conditions, and the broadening observed in sample 2 is much smaller at $E = 1$ keV. This demonstrates that low energy $\beta$-NMR spectroscopy is sensitive to the magnetization of the $Mn_{12}$ monolayer. In particular, the $^8$Li nuclei implanted into sample 1 at low $E$, and hence stopping close to the $Mn_{12}$ molecules, experience a large distribution of magnetic fields, which are attributed to the dipolar fields from the $Mn_{12}$ monolayer.

The observed broadening of the resonance line at low implantation energies, compared to high implantation energy, enables the determination of functional form of the dipolar magnetic field from the $Mn_{12}$ moments experienced by the $^8$Li. This is found to follow a power law decaying function with power $\sim$–3 as expected from its dipolar nature. It also provides a measure of the size of the magnetic moment of individual $Mn_{12}$ molecules. The main finding of our study is that the temperature dependence of the size of magnetic moment on a $Mn_{12}$ molecule is dramatically different

from bulk. In particular, at low temperatures (∼3.2 K) the magnetic moment in the monolayer is estimated to be 5–12 $\mu_B$ compared to 20 $\mu_B$ in bulk.

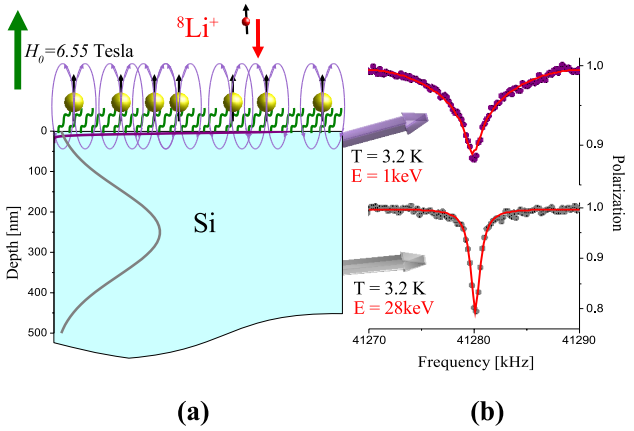


Fig. 1. (a) A schematic of sample 1 where the $Mn_{12}$ molecules are grafted on a Si substrate. The stopping profiles of $^8$Li in Si at $E = 1$ and 28 keV are also shown (purple and grey lines respectively). (b) The measured $\beta$-NMR spectra from sample 1 in an applied magnetic field $H_0 = 6.55$ T at $T = 3.2$ K. The top spectrum is for $E = 1$ keV and the bottom for $E = 28$ keV. The solid lines are fits to the calculated resonance lineshape.

**Experiment 1040**
**$\beta$-NMR investigation of the magnetic properties of manganites**
*(R. Miller, UBC–UILO; W.A. MacFarlane R.F. Kiefl, UBC)*

The manganites exhibit a range of interesting behaviour which includes large magneto-resistance, a sharp insulator-metal transition and a rich magnetic phase diagram. Numerous probes have shown that the magnetic transitions are unconventional, involving both phase separation and phase competition. In $La_{1-x}Ca_xMnO_3$ (LCMO) ($x > 0.2$), it is proposed that a strong coupling of the charge and spin degrees of freedom arises from double exchange and strong Hund coupling between the spins of the itinerant Mn charge carriers and the core spins. In materials with low doping ($x < 0.2$), Jahn-Teller effects and polarons dominate the behaviour. In many of these materials, charge order, orbital order, ferromagnetic, antiferromagnetic and paramagnetic phases can be induced with small changes in temperature, an external magnetic field, chemical composition, and light levels. Given this one would expect their properties to change as a function of distance from a surface or interface. Although many experimental methods have been applied to these materials, including $\mu$SR, neutron scattering, and NMR, none can be used to probe local properties in a depth-controlled manner.

In this experiment we are using low energy $\beta$-NMR to monitor magnetic properties of a thin film of $La_{1-x}Ca_xMnO_3$ with $x = 0.30$. The main result is the implanted $^8$Li's spin relaxation rate is sensitive to the LCMO magnetic fluctuations both in the film and in the substrate. This shows that low energy $\beta$-NMR can be used to probe spin dynamics in thin films and near the surface of a material as a function of depth.

The LCMO film was synthesized by pulsed laser deposition at the University of Toronto on epitaxially polished $SrTiO_3$ substrate and has a thickness of approximately 2,500 Å. The film exhibits a sharp insulator-metal transition at 260 K, such that it is semiconducting above $T_c$ and metallic at lower temperatures. The magnetic properties also change at $T_c$ since it is ferromagnetic below $T_c$. Although the measurements presented here were performed at a single implantation energy, a high voltage platform is being constructed for the low field spectrometer. This will allow the mean depth of implantation to be controlled on a nm lengthscale. Figure 1 shows the simulated implantation profile for a 28 keV $^8$Li ion, the beam energy used in this experiment. The peak in the distribution occurs near the middle of the film (1,500 Å) such that only about 5% of the beam lands in the substrate.

Figire 2 shows the spin relaxation measurements in a small magnetic field ($B = 150$ G) at a few different temperatures. The measurements were taken by delivering relatively long (4 s) beam pulses separated by long periods (12 s) of beam off. The beta-decay asymmetry is measured during the beam-on and beam-off periods, although only the beam-on period is shown in Fig. 2. In order to fit the data one must convolute the theoretical relaxation function with the square beam pulse. Typically a short beam pulse would be used for this purpose, in which case no convolution is required. However, we have found that the statistics and resulting signal quality are much higher with the long pulse method. At low temperature (Fig. 2a [$T = 10$ K]), the initial asymmetry is close to the full asymmetry expected (0.19) and most of the relaxation is visible in the $^8$Li time window. A fast component relaxes on a timescale of 100 ms while most of the signal relaxes on the timescale of seconds. As the temperature increases the relaxation rates increase rapidly. Near $T_c$, the relaxation is so fast the signal is barely visible in our time window (Figs. 2c [$T = 260$ K] and 2d [$T = 290$ K]). On a long time scale there is still a small amplitude slowly relaxing component, which we attribute to $^8$Li in the STO substrate expected from the predicted implantation profile (see Fig. 1).

Below $T_c$ the spin relaxation rate in STO is about an order of magnitude larger than in a bare STO crystal and about a factor of two larger above $T_c$. The

difference can be attributed to the spin fluctuations in the LCMO film. The $^8$Li in the STO lies mostly within a few hundred Angstroms of the LCMO interface (see Fig. 1) and therefore will experience fluctuating dipolar magnetic fields from the LCMO. This is confirmed by the fact that at $T = 260$ K, the relaxation rate in the STO increases sharply and is too fast to be seen. These results suggest it is possible to use the signal in the substrate to monitor fluctuations in the film. This could be useful in situations where the relaxation in the film itself is too fast to be observed directly ($T_1 \ll \tau = 1.2$ s, the $^8$Li lifetime).

Figure 3 shows the relaxation rate of the fast component, that we attribute to the LCMO film. Near $T_c$ the relaxation rate is outside the $^8$Li time window. Therefore we plot a lower bound for the relaxation rate. Above $T_c$ the signal falls back into our time window. This behaviour is expected for a ferromagnet since the spin relaxation rate should peak near $T_c$. Above $T_c$ there is a critical slowing down of the spin fluctuations as one approaches the transition from above, whereas well below $T_c$ the relaxation rate in the film decreases due to the freezing out of the magnetic excitations.

In conclusion, we have demonstrated that low energy $\beta$-NMR can be used to probe magnetic spin fluctuations in thin magnetic films. The spin fluctuations result in nuclear spin relaxation of the Li both inside the film and also in the substrate next to the film. This opens up a range of possible new experiments on manganites and other thin magnetic films.

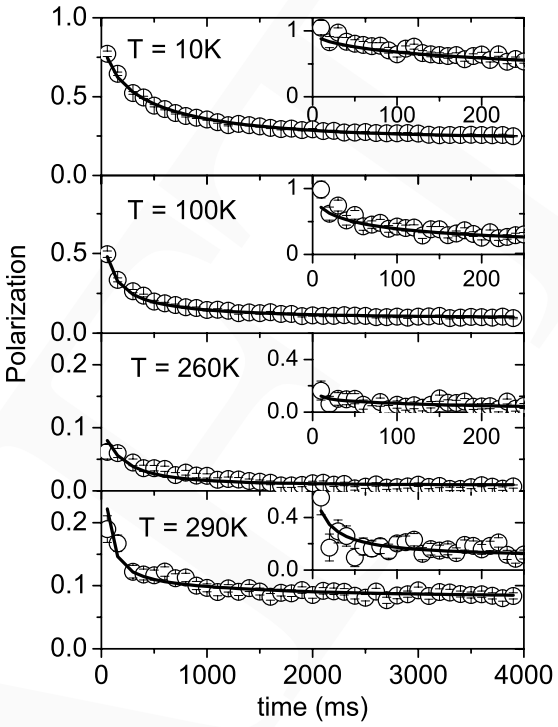


Fig. 2. Relaxation of the polarization of $^8$Li decay in the $La_{1-x}Ca_xMnO_3$ (with $x = 0.33$) film measured with $^8$Li $\beta$-NMR at various temperatures. A 4 s pulse of Li beam is delivered onto the film starting at $t = 0$. The curves are fits to the sum of a stretched exponential ($\beta = 0.5$) and an exponential function. Note that the $y$-axis for panels c and d are expanded compared to panels a and b. Insets: Polarization on an expanded time scale. The time axis is the same for each inset. Panel (a) is at the top.

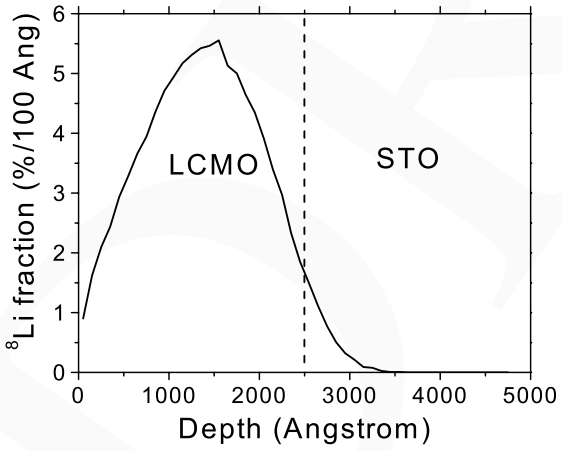


Fig. 1. Simulated implantation profile of $^8$Li ions at 28 keV implantation energy in 2,500 Åthick LCMO film on $SrTiO_3$ substrate. The implantation profile is calculated with TRIM Monte Carlo simulation.

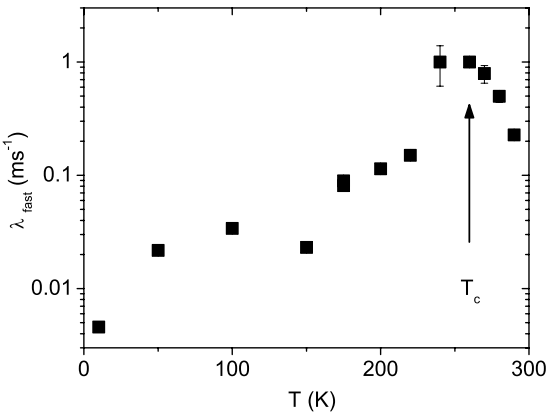


Fig. 3. Relaxation rate of the fast component from fits in Fig. 2. This relaxation is attributed to the LCMO layer.

**Experiment 1042**
**$\beta$-NMR investigation of finite size effects in metallic thin films and nanoparticle arrays**
*(T.J. Parolin, W.A. MacFarlane, UBC)*

As part of our ongoing study of finite size effects in thin metallic films, we have recently focused our attention on the particularly interesting case of palladium, a transition metal intrinsically close to a ferromagnetic instability.

The technique of $\beta$-NMR is well suited for the study of thin films, offering the potential to gain depth-resolved information that very few other spectroscopic techniques can, especially conventional NMR. Earlier results from a sample of Pd foil showed unusually large Knight shifts ($K$, a key quantity in the NMR of metals) for the implanted $^8$Li. A follow-up study using a 100 nm film on $SrTiO_3$ confirmed that the large $K$ is intrinsic to the Pd host. Before proceeding with further detailed studies of thinner samples, the results from this film are themselves intriguing as measurements of the local susceptibility around dilute, non-magnetic impurities in bulk Pd.

The incident beam was electrostatically decelerated to 11 keV for these measurements to maximize the number of ions stopping in the Pd. Two overlapping signals are seen for Li in Pd; their resonance frequencies both decrease by a similar amount as the temperature is lowered. The reference frequency used to compute $K$ was determined from the known $K$ of Li stopping in the Au capping layer (10 nm) that was deposited *in situ* onto the Pd film. Panel (a) of Fig. 1 displays the average $K$ for the Li signals as a function of temperature in an external field of 4.1 T (points). The trend in $K_{\rm avg}$ with $T$ is similar to what was seen in the 12.5 $\mu$m foil. $K$ is assumed to be dominated by the local magnetic susceptibility at the Li. If this susceptibility were the same as that for bulk Pd, $K_{\rm avg}$ should scale with $\chi_{Pd}$ for all $T$. This appears to be the case above $\approx$100 K as indicated by the solid line in (a) obtained from the linear fit of this region shown in the inset. Below this point, $\chi_{\rm Pd}$ is known to decrease, while $K_{\rm avg}$ is seen to increase further. This low-$T$ deviation can be taken as a measure of the local response of the Pd host to the isolated defect of the implanted $Li^+$ (the concentration of Li here is only $\sim$1 in $10^{11}$). This response can now be compared with detailed theoretical calculations based, for example, on the scattering of the host Pd spin fluctuations from the defect.

The spin-lattice relaxation $T_1^{-1}$ for the Li was measured in the foil at 4.1 T and the results are shown in Fig. 1(b). It is overall linear as expected for relaxation due to polarized electrons in a metal; however, the deviation at higher $T$ is attributed to Li making a site change. The rates of relaxation are much slower than expected from the large $K_{\rm avg}$. For instance, applying the Korringa relation for $K_{\rm avg} = -885$ ppm predicts a $T_1^{-1}$ given by the dashed line. In Fig. 1(c) the product $(T_1TK_{\rm avg})$ is seen to be essentially constant, as has been predicted for a nearly ferromagnetic system. The high-$T$ change in $T_1^{-1}$, and the low-$T$ increase in $K_{\rm avg}$ discussed are responsible for the small nonlinearity observed.

Preliminary measurements indicate that the shift of $^8$Li in Pd is strongly dependent on the Pd film thickness for thicknesses below 100 nm. Further measurements are planned to study this remarkable and unexpected finite size effect.

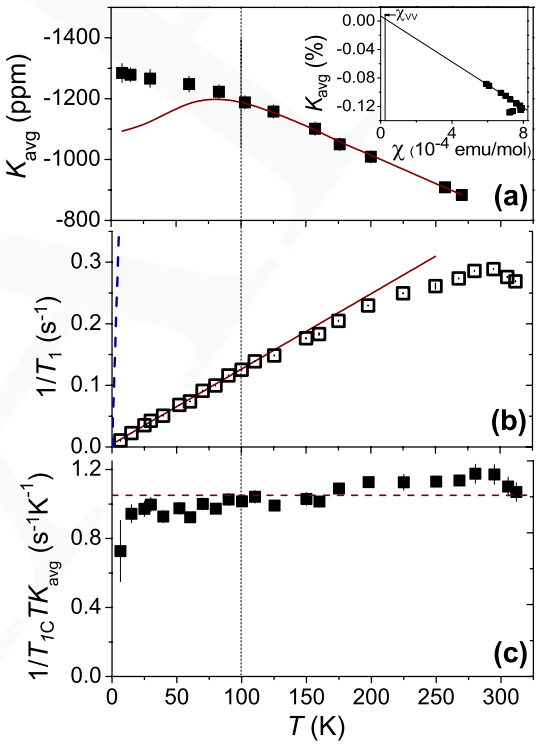


Fig. 1. (a) Knight shift of Li in 100 nm Pd at 4.1 T. The solid line represents the shifts predicted for $K_{\rm avg}$ linear with the bulk susceptibility of Pd for all $T$ (inset). (b) Spin-lattice relaxation rate $T_1^{-1}$ of Li in Pd foil at 4.1 T. (c) The product $T_1TK_{\rm avg}$ is nearly independent of $T$ as predicted for nearly ferromagnetic material. Some of the $K_{\rm avg}$ have been interpolated/extrapolated from (a).

**Experiment 1047**
**Magnetic correlations and superconductivity in $La_{2-x}Sr_xCuO_4$**
*(K. Ishida, Kyoto)*

In the cuprate superconductors, hole or electron carrier doping changes an antiferromagnetic (AFM) insulator to a $d$-wave superconductor. One of the most

important issues is to understand the interplay between the AFM and superconducting (SC) phases, i.e. whether the SC phase can coexist with the AFM phase homogeneously or whether these two phases compete with each other inhomogeneously.

A lot of experiments have already been carried out in various cuprate compounds to elucidate the interplay between two phases. The appearance of the low-temperature magnetism below $T_c$ was indicated by early $\mu$SR studies [Brewer *et al.*, Phys. Rev. Lett. **60**, 1073 (1988); Weidinger *et al.*, Phys. Rev. Lett. **62**, 102 (1989)], and it has been established by recent comprehensive $\mu$SR measurements in $YBa_2Cu_3O_{6+y}$ [Sanna *et al.*, Phys. Rev. Lett. **93**, 207001 (2004)] and $(Ca_xLa_{1-x})(Ba_{1.75-x}La_{0.25+x})Cu_3O_{6+y}$ [Kanigel *et al.*, Phys. Rev. Lett. **88**, 137003 (2002)]. However, microscopic information about this low-temperature magnetism, e.g. the magnitude and inhomogeneity of the static moments and magnetic structure, is still unclear. These are very important to understand the relation between two phases.

In the present $\mu$SR studies on $La_{2-x}Sr_xCuO_4$ (LSCO), we planned to measure the distribution of the internal field at the muon site below $T_c$, and to estimate the SC and magnetic volume fractions from the analyses of the TF-$\mu$SR spectra. Single crystals of LSCO with $x = 0.053$ ($T_c = 17$ K), 0.07 ($T_c = 17$ K), 0.10 ($T_c = 30$ K), 0.12 ($T_c = 29$ K) and 0.15 ($T_c = 38$ K) were used for the TF-$\mu$SR measurements. The TF-$\mu$SR measurements were performed in the field of 1 kOe and 60 kOe parallel to the *c*-axis. The field dependence of the relaxation rate was also investigated at several temperatures. In this report, the experimental results obtained in 1 kOe are discussed.

The muon spin relaxation rate $\sigma$ measured by the TF-$\mu$SR measurement is related to the magnetic field penetration depth $\lambda$, superconducting carrier density $n_s$, and effective mass $m^*$, as $\sigma \propto n_s/m^*$. The relaxation rate $\sigma$ was estimated by fitting $\mu^+$ time-differential relaxation data to the relaxation function,

$$G(t) = A\exp[-(\sigma t)^\gamma]\cos(\gamma_\mu B_\mu + \phi),$$

where $A$ is the initial muon decay asymmetry, $\gamma_\mu$ is the $\mu^+$ gyromagnetic ratio, $B_\mu$ is the local field at the stopping muon site, and $\phi$ is the phase of the initial $\mu^+$ spin orientation.

Figure 1 shows the temperature dependence of $\sigma$ for $La_{2-x}Sr_xCuO_4$ with $x = 0.07$, 0.10, 0.12 and 0.15. Above $T_c$, $\sigma(T)$ is temperature independent with the value of $\sigma \sim 0.15$ $\mu s^{-1}$ in these compounds. In $x = 0.15$, $\sigma(T)$ increases below $T_c$, following the relation of

$$\sigma(T) = 0.15 + \Delta\sigma(T \to 0)\left[1 - \left(\frac{T}{T_c}\right)^\beta\right].$$

In $x = 0.15$, the best fitting was observed when $\beta = 1$, and $\Delta\sigma(T \to 0) = 0.65$ ($\mu s^{-1}$). In $x = 0.07$, 0.10 and 0.12, $\sigma(T)$ increases below $T_c$, but abruptly enhances below $T_g$, which is much lower than $T_c$. The abrupt increase below $T_g$ gives clear evidence of the occurrence of the static magnetism. The TF-$\mu$SR spectra of these compounds at the lowest temperature exhibit a broad peak without clear structure, indicating that the internal field is inhomogeneously distributed. In $x = 0.07$, the internal field ranges from zero to ∼150 Oe, suggesting that the ordered moments are distributed from 0 to 0.17 $\mu_B$, when the coupling constant between the muon spins and the ordered moments ($A_\mu \sim 860$ Oe/$\mu_B$) found in undoped $La_2CuO_4$ is employed [Nachumi *et al.*, Phys. Rev. **B58**, 8760 (1998)].

Figure 2 shows a plot of $T_c$ vs. $\Delta\sigma(T \to 0)$ in these compounds. It is well known that the universal relation called the "Uemura relation", which is the linear relation between $\Delta\sigma$ and $T_c$, holds in various underdoped cuprate superconductors [Uemura *et al.*, Phys. Rev. Lett. **62**, 2317 (1989)]. As seen in Fig. 2, the linear relation seems to be observed between $T_c$ and $\Delta\sigma(T \to 0)$, and the coefficient is $72.9 \pm 8.0$ (K/$\mu s^{-1}$). It is noted that $\Delta\sigma(T \to 0)$ in this estimation approximately corresponds to $\sigma_{TF}/\sqrt{2}$, since $\sigma_{TF}$ is given by $\exp[-(\sigma_{TF}t)^2/2]\cos(\gamma_\mu B_\mu t + \phi)$. Therefore, the coefficient in the present measurement corresponds to $51.5 \pm 5.7$ (K/$\mu s^{-1}$) in $\sigma_{TF}$ in the Gaussian function, which is close to ∼40 (K/$\mu s^{-1}$) in the Uemura plot, because $\sigma_{TF}$ was used in the Uemura plot. It seems that the Uemura relation holds in the underdoped $La_{2-x}Sr_xCuO_4$.

Figure 3 shows the Sr concentration dependence of $T_c$ and $T_g$, in which those temperatures determined in polycrystalline LSCO samples were also plotted [Panagopoulos *et al.*, Phys. Rev. **B66**, 064501 (2002)]. $T_g$ was determined from the abrupt increase of $\sigma(T)$ in Fig. 1. $T_g$ gradually decreases with increasing Sr concentration, but has the local maximum around $x = 0.12$, which corresponds to the 1/8 anomaly. The internal field at the muon site at 2 K in $x = 0.12$ is much larger than that in $x = 0.10$, indicating that the static magnetism is enhanced in $x = 0.12$. $T_g$ in $x = 0.15$ seems to be lower than 2 K. Our present data are in good agreement with the previous data. The analyses of the TF-$\mu$SR spectra for the estimation of the two-phase volume are now in progress.

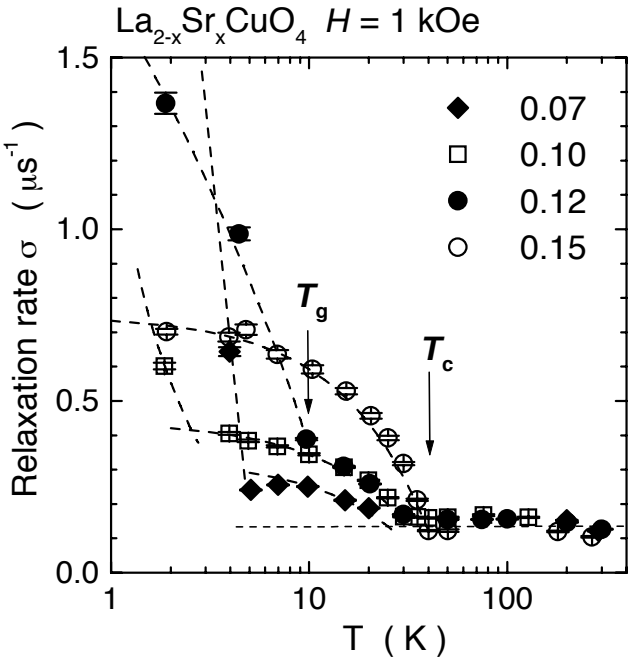


Fig. 1. The TF-$\mu$SR relaxation rate $\sigma$ as a function of temperature for the LSCO with $x = 0.07$, 0.10, 0.12, and 0.15. $T_c$ determined with dc-susceptibility measurements are shown by arrows. $T_g$ below which the $\sigma$ abruptly increases is also shown by arrows.

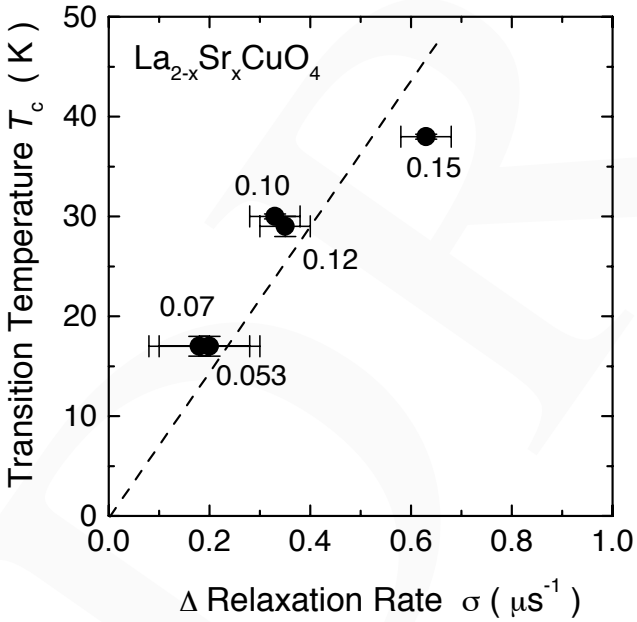


Fig. 2. The increase of the muon spin relaxation rate $\sigma(T \rightarrow 0)$ ascribed to the SC diamagnetism is plotted against $T_c$. The dotted line is the fitting of these data, with a linear coefficient $72.9 \pm 8.0$ (K/$\mu$s$^{-1}$).

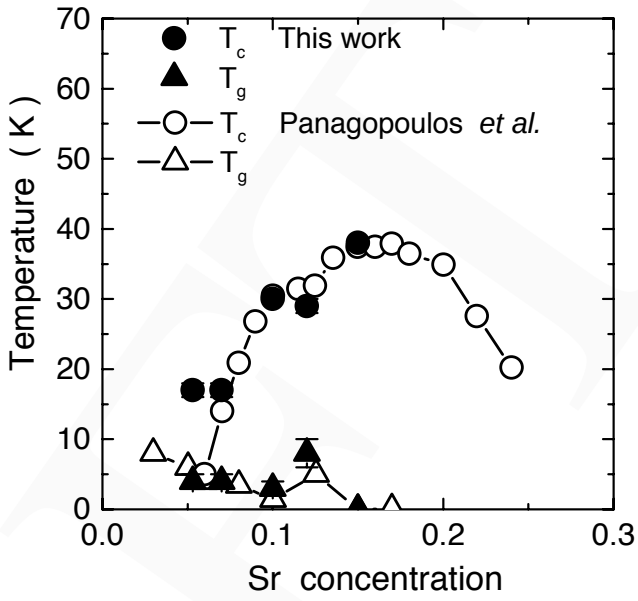


Fig. 3. The Sr concentration dependence of $T_c$ and $T_g$. $T_c$ and $T_g$ determined in polycrystalline LSCO by Panagopoulos *et al.* were also plotted.

**Experiment 1049**
**Spin state transition in *RE*CoO$_3$ (*RE* = La,Pr, Nd and Sm)**
*(J. Sugiyama, Toyota CRDL Inc.; J.H. Brewer, UBC-TRIUMF)*

The purpose of Expt. 1049 is to detect a spin state transition and an accompanying critical phenomenon in $RE$CoO$_3$ perovskites with $RE$ = La, Pr, Nd, and Sm by means of muonic Knight shift(s) measurements.

In a September $\mu^+$SR experiment on single crystals of the $RE$CoO$_3$ perovskites in the $T$ range between 1.8 and 320 K, we have found evidence of a spin state transition around 150 K as seen in the muon Knight shift ($K_\mu$) in LaCoO$_3$. A similar indication also appears in PrCoO$_3$ and NdCoO$_3$ around 150 K, whereas no $K_\mu$ anomalies are seen in La$_{0.95}$Sr$_{0.05}$CoO$_3$.

LaCoO$_3$ exhibits temperature-induced magnetic transitions around 100 and 500 K, which have attracted considerable interest in the past 50 years [Radaelli and Cheong, Phys. Rev. **B66**, 094408 (2002)]. Goodenough [J. Phys. Chem. Solids **6**, 287 (1958); in Magnetism and the Chemical Bond (Wiley, New York, 1963)] originally explained that LaCoO$_3$ underwent a spin state transition from a low-$T$ low-spin ($LS$, $S$=0, $t_{2g}^6$) state to a high-$T$ high-spin ($HS$, $S$=2, $t_{2g}^4 e_g^2$) state at around 100 K. In 1996, a new concept including an intermediate-spin ($IS$, $S$=1, $t_{2g}^5 e_g^1$) state was proposed based on an LDA+U calculation [Potze *et al.*, Phys. Rev. **B51**, 11501 (1995)]. Currently, the two transitions ($T_{\rm SS}^{\rm L}$ and $T_{\rm SS}^{\rm H}$) are believed to be the spin-state transitions from $LS$ to $IS$ around 100 K and $IS$ to $HS$ around 500 K, respectively. For other $RE$CoO$_3$,

$T_{SS}^{L}$ ∼200 K and $T_{SS}^{H}$ ∼500 K for $PrCoO_3$, 300 K and 500 K for $NdCoO_3$ and unknown for $SmCoO_3$. For lightly Sr-doped $LaCoO_3$ crystals, the value of $T_{SS}^{L}$ decreases linearly from 100 K to below 4.2 K as the Sr content increases up to 0.01.

Since $\mu^+$SR is a very powerful technique for detecting spin-state transitions, as we demonstrated in the layered cobalt dioxides $[Ca_2CoO_3]_{0.62}[CoO_2]$ [Sugiyama *et al.*, Physica **B326**, 518 (2003)], we proposed systematic $\mu^+$SR measurements on $RECoO_3$ crystals in high transverse magnetic fields over a wide temperature range (1.8 K to 900 K) in order to clarify the nature of the spin-state transitions and the low $T$ magnetic phase.

Indeed, we successfully detected an indication of $T_{SS}^{L}$ for $LaCoO_3$, $PrCoO_3$ and $NdCoO_3$ around 150 K by means of TF-$\mu^+$SR with $H = 1$ T on M15 using Helios, although there are no anomalies in $La_{0.95}Sr_{0.05}CoO_3$.

Figure 1 shows all the results obtained in the experiment in 2006, that is, the $T$ dependence of the Knight shift ($K_\mu$) and the dc susceptibility ($\chi$) measured in a magnetic field of $H = 1$ T. Note that both measurements were carried out using the same sample. The Knight shift was measured by a TF-$\mu^+$SR technique with a reference mode using Ag as a reference.

Basically, the $K_\mu(T)$ curve is similar to the $\chi(T)$ curve, because of the relationship $K_\mu(T) = A_{hf}\chi(T)$, where $A_{hf}$ is the hyperfine coupling constant. However, the $K_\mu(T)$ curve deviates from the $\chi(T)$ curve below 150 K for $LaCoO_3$, although both curves are very similar for $La_{0.95}Sr_{0.05}CoO_3$, which does not exhibit a spin state transition. Moreover, the $K_\mu(T)$ curve for $PrCoO_3$ shows a small maximum around 140 K, while $\chi$ increases monotonically with decreasing $T$. For $NdCoO_3$, the $K_\mu(T)$ curve shows a small shoulder around 150 K, in spite of the Curie-Weiss behaviour of $\chi$.

In order to confirm the relationship between $K_\mu$ and $\chi$, Fig. 2 shows the so-called $K_\mu - \chi$ plot for the four samples. One can clearly see anomalies – i.e. a small maximum at $\chi = 0.004$ emu/mol-Co for $LaCoO_3$ and at 0.008 emu/mol-Co for $PrCoO_3$ and $NdCoO_3$. The linear $\chi$ dependence of $K_\mu$ for $La_{0.95}Sr_{0.05}CoO_3$ with a slope of 45° indicates that the sample is a simple Curie-Weiss paramagnet under $H = 1$ T in the whole $T$ range measured. Since the slope for $La_{0.95}Sr_{0.05}CoO_3$ is almost the same as that for $LaCoO_3$ above 200 K for which Co ions are in the intermediate-spin state, the spin state of Co ions in $La_{0.95}Sr_{0.05}CoO_3$ is also likely to be an intermediate-spin state below 320 K.

Assuming that the small maximum corresponds to $T_{SS}^{L}$, $T_{SS}^{L} \sim 150$ $K$ for $LaCoO_3$, although the past bulk measurements showed $T_{SS}^{L}$ ∼100 K. This is probably due to the fact that $\mu^+$SR is sensitive to local magnetic environment. We also find that $T_{SS}^{L} \sim 140$ K for $PrCoO_3$ and ∼150 K for $NdCoO_3$, while the past $\chi(T)$ measurement suggested ∼200 K for $PrCoO_3$ and ∼300 K for $NdCoO_3$. This is because the large magnetic moments of Pr and Nd hinder the anomaly associated with the spin state transition in the $\chi(T)$ curve. Usually, the contribution of the rare earth moment is subtracted from the measured $\chi(T)$ curve. However, the residual $\chi(T)$ curve showed a broad minimum which may lead to ambiguous conclusions (see Fig. 3) [Yan *et al.*, Phys. Rev. **B69**, 134409 (2004)]. Hence we wish to emphasize that the existence of $T_{SS}^{L}$ for $PrCoO_3$ and $NdCoO_3$ is definitely confirmed only by the present $\mu^+$SR experiment.

In conclusion, we have used $\mu$SR to detect spin-state transition in the $RECoO_3$ perovskites via muonic Knight shift measurements. This could also lead to other uses for $\mu$SR in studying magnetism. For example, if $\mu^+$SR detects the spin state transitions, we could also possibly observe a Jahn-Teller transition in transition metal ($M$) oxides, in which the spin state is also altered by the competition between thermal fluctuation and a crystal field splitting in $MO_6$ octahedra. Here, it should be noted that a $^{59}$Co-NMR technique is unavailable above 50 K due to a short nuclear spin-spin relaxation time in the $IS$ state [Itoh and Hashimoto, Physica **C341-348**, 2141 (2000)].

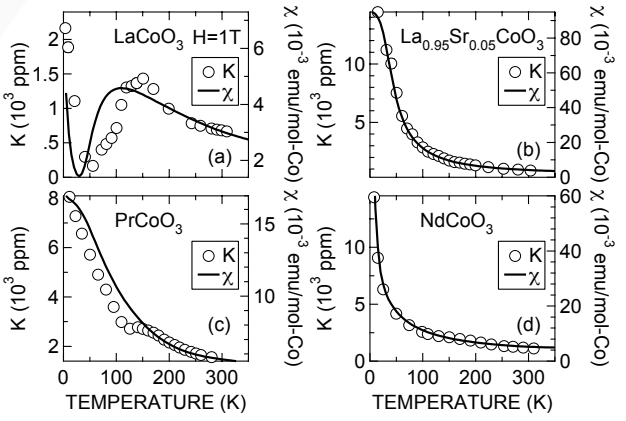


Fig. 1. $T$ dependence of both $K_\mu$ relative to Ag and $\chi$ for (a) $LaCoO_3$, (b) $La_{0.95}Sr_{0.05}CoO_3$, (c) $PrCoO_3$, and (d) $NdCoO_3$. $K_\mu$ and $\chi$ were measured using the same sample under magnetic field of $H = 1$ T with field-cooled mode by TF-$\mu^+$SR and SQUID magnetometer.

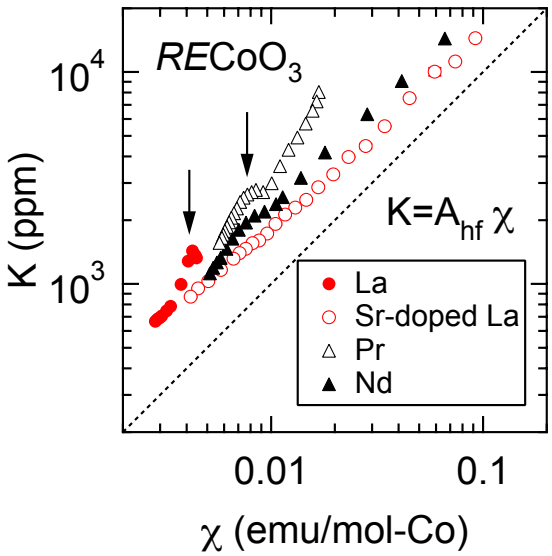


Fig. 2. The relationship between $K_\mu$ and $\chi$ for the four $RE$CoO$_3$ crystals. The three pure samples show a local maximum due to $T_{SS}^{L}$, whereas a quite linear relationship is obtained for the Sr-doped LaCoO$_3$ in the whole $T$ range measured.

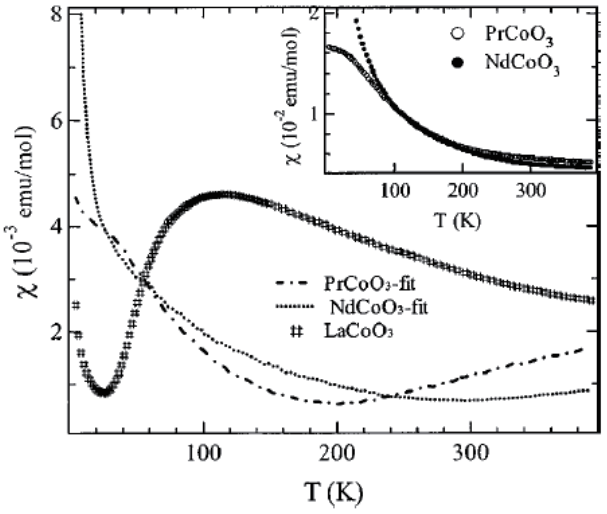


Fig. 3. [Yan *et al., op. cit.*] $T$ dependence of $\chi$ for single crystals of LaCoO$_3$, PrCoO$_3$, and NdCoO$_3$ measured at 500 Oe. Contribution from magnetic $Pr^{3+}$ and $Nd^{3+}$ were subtracted. Inset: Measured $\chi$ before the subtraction for PrCoO$_3$ and NdCoO$_3$.

**Experiment 1050**

**Lithium battery materials $LiCo_{1-y}Ni_yO_2$ with $0 \leq y \leq 1$**

*(J. Sugiyama, Toyota CRDL Inc.; J.H. Brewer, UBC-TRIUMF)*

The layered nickel dioxides, a series of materials with chemical formula $A^+Ni^{3+}O_2$, such as rhombohedral LiNiO$_2$ [Kitaoka *et al.*, J. Phys. Soc. Jpn. **67**, 3703 (1998); Chatterji *et al.*, J. Phys.: Cond. Matter **17**, 1341 (2005)], NaNiO$_2$ [Darie *et al.*, Eur. Phys. J. **B43**, 159 (2005); Lewis *et al.*, Phys. Rev. **B72**, 014408 (2005); Baker *et al.*, Phys. Rev. **B72**, 104414 (2005)], and AgNiO$_2$ [Shin *et al.*, J. Solid State Chem. **107**, 303 (1993); Kikuchi *et al.*, Hyp. Int. **120/121**, 623 (1999)], in which Ni ions form the two-dimensional triangular lattice 2DTL by the connection of edge-sharing NiO$_6$ octahedra, have been considered to be good candidates for an ideal half-filled 2DTL. In these materials at low temperature, there is a strong interaction between the $Ni^{3+}$ ions and the crystalline electric field of the NiO$_6$ octahedron. This causes the $Ni^{3+}$ ions to be in the low spin state with a $t_{2g}^6 e_g^1$ ($S = 1/2$) configuration.

Among the three layered nickel dioxides, NaNiO$_2$ is perhaps the best investigated. It exhibits two transitions at $T_{JT} \sim 480$ K and $T_N = 23$ K. The former is a cooperative Jahn-Teller (JT) transition from a high-$T$ rhombohedral phase to a low-$T$ monoclinic phase, while the latter is a transition into an A-type AF phase – i.e. ferromagnetic (FM) order in the NiO$_2$ plane but AF between the two adjacent NiO$_2$ planes, as has been reconfirmed very recently by both neutron diffraction [Darie *et al., op. cit.*; Lewis *et al., op. cit.*], and positive muon spin rotation/relaxation ($\mu^+$SR) experiments [Baker *et al., op. cit.*]. The magnetic order is associated with the JT induced trigonal distortion which stabilizes a half occupied $d_{z^2}$ orbital [Meskine *et al.*, Phys. Rev. **B72**, 224423 (2005)].

Although LiNiO$_2$ and NaNiO$_2$ are structurally very similar, LiNiO$_2$ shows dramatically different magnetic properties. LiNiO$_2$ exhibits neither a cooperative JT transition nor long-range magnetic order down to the lowest $T$ investigated. In fact, both heat capacity and NMR measurements suggest a spin-liquid state with short-range FM correlations [Kitaoka *et al., op. cit.*]. Chatterji *et al.* [*op. cit.*], however, found a rapid increase in the muon spin relaxation rates in LiNiO$_2$ below ~10 K using the longitudinal field-$\mu^+$SR technique, suggesting a spin-glass-like behaviour below 10 K. The discrepancy between the two results is considered to be a sample-dependent phenomenon that arises from the difficulties in preparing stoichiometric LiNiO$_2$. The third compound, AgNiO$_2$, also lacks a cooperative JT transition. A magnetic transition $T_N$ was clearly observed by both susceptibility ($\chi$) and $\mu^+$SR measurements but long-range magnetic order was not detected by a neutron diffraction experiment even at 1.4 K [Kikuchi *et al., op. cit.*].

While the nature of the magnetic ground states of LiNiO$_2$ and AgNiO$_2$ is still not clear, the FM interaction on the 2DTL NiO$_2$ plane has been thought to be common for all the layered Ni dioxides with a half-filled state because of the clear magnetic order ob-

served in $NaNiO_2$. In this paper, we present measurements that demonstrate this supposition is incorrect. This is accomplished by investigating the magnetism in $Ag_2NiO_2$, a material that can be represented by the chemical formula $(Ag_2)^+Ni^{3+}O_2$ and hence is expected to have a $NiO_2$ plane that has properties identical to the above three layered nickel dioxides. However, in $Ag_2NiO_2$, static AF order, likely the formation of an incommensurate AF structure in the $NiO_2$ plane, is observed instead.

Disilver nickel dioxide $Ag_2NiO_2$ is a rhombohedral system with space group $R\overline{3}m$ ($a_{\rm H} = 0.29193$ nm and $c_{\rm H} = 2.4031$ nm for the hexagonal unit-cell) [Schreyer *et al.*, Angew. Chem. **41**, 643 (2002)] that was found to exhibit two transitions at $T_{\rm S} = 260$ K and $T_{\rm N} = 56$ K by resistivity and $\chi$ measurements, while the symmetry remains rhombohedral down to 5 K [Yoshida *et al.*, Phys. Rev. **B73**, 020408(R) (2006)]. Interestingly, $Ag_2NiO_2$ shows metallic conductivity down to 2 K probably due to a quarter-filled Ag $5s$ band, as in the case of $Ag_2F$ [Andres *et al.*, J. Phys. Chem. Solids **27**, 1747 (1966)]. Very recently, Yoshida *et al.* proposed the significance of the AF interaction in the 2DTL $NiO_2$ plane from the $\chi(T)$ measurement.

Susceptibility ($\chi$) was measured using a superconducting quantum interference device magnetometer (mpms, Quantum Design) in the temperature range between 400 and 5 K under magnetic field $H \leq 55$ kOe. For the $\mu^+$SR experiments, the $Ag_2NiO_2$ powder was pressed into a disk of about 20 mm diameter and 1 mm thickness, and subsequently placed in a muon-veto sample holder. The $\mu^+$SR spectra were measured on the M20 surface muon beam line at TRIUMF.

Figure 1 shows zero-field (ZF-)$\mu^+$SR time spectra in the $T$ range between 1.9 K and 60 K for a powder sample of $Ag_2NiO_2$. A clear oscillation due to quasi-static internal fields $\mathbf{H}_{\rm int}$ is observed below 54 K, unambiguously establishing the existence of long-range magnetic order in the sample. Interestingly, as $T$ is decreased from 60 K, the relaxation rate first decreases down to $\sim$20 K and then increases as $T$ is lowered further. By contrast, the average oscillation frequency increases monotonically down to 1.9 K. This implies that the distribution of $\mathbf{H}_{\rm int}$ at $T \geq 54$ K and $\leq$20 K is larger than that at $20\,K < T < 54\,K$.

This is further established by the $T$ dependence of the Fourier transform of the ZF-$\mu^+$SR time spectrum shown in Fig. 2. Note that there is clearly line broadening below 20 K as well as above 54 K. The line-broadening above 54 K is reasonably explained by critical phenomena in the vicinity of $T_{\rm N} = 56$ K; however, it is difficult to understand the origin of the line-broadening below 20 K using a classical AF model without invoking the presence of an additional magnetic transition. Furthermore, even the spectrum at 30 K, which is the sharpest FFT measured, consists of a main peak at $\sim$14 MHz and a shoulder around 16 MHz, suggesting a wide distribution of $\mathbf{H}_{\rm int}$ in $Ag_2NiO_2$.

We therefore use a combination of three signals to fit the ZF-$\mu^+$SR time spectrum:

$$\begin{aligned} A_0\,P_{\rm ZF}(t) &= A_1\,\cos(\omega_{\mu,1}t+\phi)\,\exp(-\lambda_1 t) \\ &\quad + A_2\,J_0(\omega_{\mu,2}t)\,\exp(-\lambda_2 t) \\ &\quad + A_{\rm slow}\,\exp(-\lambda_{\rm slow}t)\,, \end{aligned} \tag{7}$$

where $A_0$ is the empirical maximum muon decay asymmetry, $A_1$, $A_2$ and $A_{\rm slow}$ are the asymmetries associated with the three signals, $J_0(\omega_{\mu,2}t)$ is a zeroth-order Bessel function of the first kind that describes the muon polarization evolution in an incommensurate spin density wave (IC-SDW) field distribution [Kalvius *et al.*, *Handbook on the Physics and Chemistry of Rare Earths* eds. K.A. Gschneidner Jr. *et al.* (North-Holland, Amsterdam, 2001) v. 32, chap. 206], and $\omega_{\mu,1} < \omega_{\mu,2}$.

Although $J_0(\omega t)$ is widely used for fitting the ZF-$\mu^+$SR spectrum in an IC-SDW state, it should be noted that $J_0(\omega t)$ only provides an approximation of the generic IC magnetic field distribution. This is because the lattice sum calculation of the dipole field at the muon site ($\mathbf{H}_{\rm IC}$) due to an IC magnetic structure lies in a plane and traces out an ellipse. The half length of the major axis of the ellipse corresponds to $H_{\rm max}$, whereas half of the minor axis corresponds to $H_{\rm min}$. As a result, the IC magnetic field distribution $P_{\rm IC}$ is generally given by [Kalvius *et al.*, Physica **B206-207**, 205 (1995)]

$$P_{\rm IC} = P(\mathbf{H}_{\rm IC}) = \frac{2}{\pi}\frac{H}{\sqrt{(H^2-H_{\rm min}^2)(H_{\rm max}^2-H^2)}}\,. \tag{8}$$

The distribution diverges as $H$ approaches either $H_{\rm min}$ or $H_{\rm max}$ (see Fig. 3). $J_0(\omega t)$ describes the field distribution very well except in the vicinity of $H_{\rm min}$, and the value of $\omega$ should be interpreted as an accurate measure of $H_{\rm max}$. However, $J_0(\omega t)$ provides no information on $H_{\rm min}$. Hence, the first term $A_1\cos(\omega_{\mu,1}t + \phi_1)\exp(-\lambda_1 t)$ is added in Eq. (1) to account for the intensity around $H_{\rm min}$ and to determine the value of $H_{\rm min}(=\omega_{\mu,1}/\gamma_\mu)$ [Andreica, Ph.D. thesis, IPP/ETH-Zurich (2001)] ($\gamma_\mu$ is the muon gyromagnetic ratio and $\gamma_\mu/2\pi = 13.55342$ kHz/Oe). In other words, only when $H_{\rm min} = 0$, Eq. (2) is well approximated by $J_0(\omega t)$. Here it should be emphasized that $\mu^+$SR spectra are often fitted in a time domain, i.e. not by Eq. (2) but by Eq. (1), since information on all the parameters such as $A$, $\omega$, $\lambda$ and $\phi$ are necessary to discuss the magnetic nature of the sample.

We note that the data can also be well-described using two cosine oscillation signals, $A_1\cos(\omega_{\mu,1}t +$

$\phi_1)\exp(-\lambda_1 t) + A_2\cos(\omega_{\mu,2}t + \phi_2)\exp(-\lambda_2 t)$ with $\phi_2$ = –54 ± 10° below $T_N$. The delay is physically meaningless, implying that the field distribution fitted by a cosine oscillation, i.e. a commensurate $\mathbf{H}_{int}$ does not exist in $Ag_2NiO_2$. [Kalvius *et al., op. cit.* (2001)] Furthermore, as $T$ decreases from 54 K, $A_1$ ($A_2$) decreases (increases) linearly with $T$ from 0.15 (0) at 54 K to 0 (0.15) at 1.9 K. In order to explain the $A_1(T)$ and $A_2(T)$ curves, one would need to invoke the existence of two muon sites, and a situation whereby the population of $\mu^+$ at each site is changing in proportion to $T$. Such behaviour is very unlikely to occur at low $T$. Hence, we believe that our data strongly suggest the appearance of an IC-AF order in $Ag_2NiO_2$ below $T_N$, as predicted by the calculation using a Mott-Hubbard model (discussed later). Such a conclusion is also consistent with the fact that the paramagnetic Curie temperature is –33 K estimated from the $\chi(T)$ curve below 260 K [Yoshida *et al., op. cit.*].

Figures 4(a)–4(d) show the $T$ dependence of the muon precession frequencies ($\nu_i = \omega_{\mu,i}/2\pi$), the volume fraction of the paramagnetic phases ($V_{para}$), $\Delta\nu = \nu_2 - \nu_1$, $\lambda_1$, $\lambda_2$, the asymmetries $A_1+A_2$, $A_1$, $A_2$, $A_{slow}$, and $\chi$ for the powder sample of $Ag_2NiO_2$. Here, $V_{para}$ is estimated from the weak transverse field (wTF-) $\mu^+$SR experiment described later. In agreement with the FFTs shown in Fig. 2, as $T$ is decreased from 60 K, $\nu_2$ appears at 54 K. It then increases monotonically with decreasing $T$ down to around 20 K, and then increases more rapidly upon further cooling. The $\nu_1(T)$ curve exhibits a similar behaviour to that observed for $\nu_2(T)$. It is noteworthy that as $T$ is decreased from 80 K, the $V_{para}(T)$ curve shows a sudden drop down to ∼0 at $T_N$, indicating that the whole sample enters into an IC-AF state.

As $T$ decreases from $T_N$, $\Delta\nu$, which measures the distribution of $\mathbf{H}_{int}$ in the IC-AF phase, rapidly decreases down to ∼0.8 MHz at 40 K, then seems to level off the lowest value down to ∼20 K and then increases with increasing slope ($|d\Delta\nu/dT|$) until it reaches 4 MHz at 1.9 K. The overall $T$ dependence of $\Delta\nu$ is similar to that of $\lambda_i$. This behaviour is expected since a large $\Delta\nu$ naturally implies a more inhomogeneous field distribution – i.e, an increased flattening of the ellipse that enhances $\lambda_i$. The asymmetry of the IC magnetic phase, $A_1+A_2$, also increases monotonically with decreasing $T$, although a small jump likely exists around 20 K. The existence of a significant $A_1$ underscores the inappropriateness of fitting the ZF-$\mu^+$SR data with only a $J_0(\omega_{\mu,2}t)$ term. In fact, note that $A_1 < A_2$ above 20 K, suggesting that the IC-AF order develops/completes below 20 K. This is consistent with the rapid increases in $\Delta\nu$ and $\lambda_i$ below 20 K, as described above.

The behaviour of the muon parameters is quite consistent with the $\chi(T)$ curve, which exhibits a sudden increase in the slope ($|d\chi_{FC}/dT|$) below ∼22 K (= $T_m$) with decreasing $T$. Note the $\chi(T)$ curve measured under $ZFC$ conditions starts to deviate from that measured in the $FC$ configuration below $T_N$, suggesting the development of a ferro- or ferrimagnetic component probably due to a canted spin structure [Lewis *et al., op. cit.*]. The ferro- or ferrimagnetic behaviour is, however, observed only at low $H$, although the cusp at $T_N$ is clearly seen with $H$ = 100–10 kOe (see Figs. 4(d) and 6(d)). Below $T_m$, $\chi_{FC}$ increases with decreasing $T$, while the slope is suppressed by increasing $H$ (see Fig. 5). Keeping in mind that $\mu^+$SR is insensitive to magnetic impurities, we conclude that $Ag_2NiO_2$ undergoes a transition from a paramagnetic to an IC-AF state at $T_N$ = 56 K and then to a slightly different ordered state at $T_m \sim$ 22 K.

It is worth contrasting the current $\mu^+$SR results on $Ag_2NiO_2$ with those in related compounds $NaNiO_2$ and $AgNiO_2$. The ZF-$\mu^+$SR spectrum on a powder sample of $NaNiO_2$ consists of two signals below $T_N$(∼20 K): an exponentially relaxing cosine oscillating signal (same as the first term in Eq. (1)) as the predominant component and a minor signal described by an exponential relaxation [Baker *et al., op. cit.*] This indicates that the whole $NaNiO_2$ sample enters into a commensurate AF state below $T_N$, being consistent with the magnetic structure determined by neutron diffraction experiments, i.e., an A-type AF order [Darie *et al., op. cit.*; Lewis *et al., op. cit.*]. Interestingly, the value of $\nu_{T\to 0\,K}$ = 64.2 MHz, which corresponds to $H_{int} \sim$ 0.5 T, is 2.5 times higher than that for $Ag_2NiO_2$. The muon site in $NaNiO_2$ is assigned to the vicinity of the O ions [Baker *et al., op. cit.*], and is also thought to be reasonable for the other layered nickel dioxides. The differences between the $\mu^+$SR results on $NaNiO_2$ and $Ag_2NiO_2$ hence suggest that the magnetic structure of $Ag_2NiO_2$ is most unlikely to be an A-type AF. Furthermore, there are no indications for additional transitions of $NaNiO_2$ below $T_N$ by $\chi$, $\mu^+$SR and neutron diffraction measurements.

In $AgNiO_2$, the primary ZF-$\mu^+$SR signal is one that exponentially relaxes down to the lowest $T$ (∼3 K). Below $T_N$ (= 28 K), three minor oscillating components appear. These have small amplitudes and correspond to internal fields from 0.2 to 0.33 T (27–45 MHz) [Kikuchi *et al., op. cit.*]. The comparison between $AgNiO_2$ and $Ag_2NiO_2$ indicates that the interlayer separation ($d_{NiO_2}$) enhances the static magnetic order in the $NiO_2$ plane. It is highly unlikely that the AF interaction through the double $Ag_2$ layer is stronger than that through the single Ag layer, since $d_{NiO_2}$ = 0.801 nm for $Ag_2NiO_2$[Schreyer *et al., op. cit.*]

and 0.612 nm for $AgNiO_2$ [Shin *et al., op. cit.*].

Our results therefore suggest that the AF order exists in the $NiO_2$ plane, in contrast to the situation in $NaNiO_2$. Assuming the AF interaction is in the $NiO_2$ plane, an IC-spiral SDW phase is theoretically predicted to appear in a half-filled 2DTL [Krishnamurthy *et al.*, Phys. Rev. Lett. **64**, 950 (1990)] (calculated using the Hubbard model within a mean field approximation with $U/t \geq 3.97$, where $U$ is the Hubbard on-site repulsion and $t$ is the nearest-neighbour hopping amplitude). In order to further establish the magnetism in $Ag_2NiO_2$, it would be interesting to carry out neutron diffraction experiments to determine the magnetic structure below $T_N$ and below $T_m$.

We wish to mention here that if the valence state of the Ni ion in the $NiO_2$ plane can be varied for $Ag_2NiO_2$, the resultant phase diagram should serve as an interesting comparison with that of $A_xCoO_2$ ($A$ = alkali elements) with $x \leq 0.5$. Unlike $Li_xNiO_2$, ($Ag_2$)-deficient samples are currently unavailable, probably because of the metal-like Ag-Ag bond in the disilver layer [Schreyer *et al., op. cit.*]. A partial substitution for $Ag_2$ by other cations has thus far also been unsuccessful for reasons unknown.

In order to elucidate the magnetic behaviour above $T_N$, in particular near $T_S = 260$ K, we carried out weak transverse field (wTF) $\mu^+$SR measurements up to 300 K. The wTF-$\mu^+$SR spectrum was fitted by a combination of slow and fast relaxing precessing signal; the former is due to the external field and the latter due to the internal AF field (same as the first term in Eq. (1));

$$A_0\, P_{\rm TF}(t) = A_{\rm TF} \cos(\omega_{\mu,{\rm TF}} t + \phi_{\rm TF}) \exp(-\lambda_{\rm TF} t) + A_{\rm AF} \cos(\omega_{\mu,{\rm AF}} t + \phi_{\rm AF}) \exp(-\lambda_{\rm AF} t)\,, \quad (9)$$

where $\omega_{\mu,{\rm TF}}$ and $\omega_{\mu,{\rm AF}}$ are the muon Larmor frequencies corresponding to the applied weak transverse field and the internal AF field, $\phi_{\rm TF}$ and $\phi_{\rm AF}$ are the initial phases of the two precessing signals and $A_n$ and $\lambda_n$ ($n$ = TF and AF) are the asymmetries and exponential relaxation rates of the two signals. Note that we have ignored the $J_0(\omega t)$ term in Eq. (3) since we are primarily interested in the magnetic behaviour above $T_N$.

The results are shown in Fig. 6 together with $\chi^{-1}$. Besides the transition at 56 K, there are no anomalies up to 300 K in the normalized asymmetries, the relaxation rate ($\lambda_{\rm TF}$) or the shift of the muon precession frequency ($\Delta\omega_{\mu,{\rm TF}}$). Transverse field (TF) $\mu^+$SR measurements at $H = 2600$ Oe, which should be about 50 times more sensitive to frequency shifts than the wTF measurements, show no obvious changes in $\Delta\omega_{\mu,{\rm TF}}$ at $T_S$ either. On the other hand, the $\chi^{-1}(T)$ curve exhibits a clear change in slope at $T_S$. Above 60 K, the normalized wTF-asymmetry ($A_{\rm TF}$) levels off to its maximum value – i.e. the sample volume is almost 100% paramagnetic. This therefore suggests that $T_S$ is induced by a purely structural transition and there is no dramatic change in the spin state of Ni ions; that is, $T_S$ is unlikely to be a cooperative JT transition. This is consistent with the fact that the crystal structure remains rhombohedral down to 5 K [Yoshida *et al., op. cit.*].

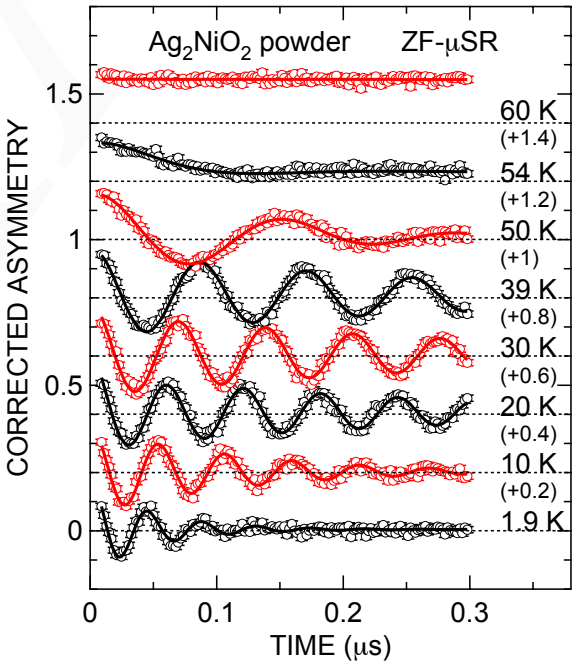


Fig. 1. Temperature dependence of the ZF-$\mu^+$SR time spectra of a powder sample of $Ag_2NiO_2$. Each spectrum is offset by 0.2 for clarity of the display. The solid lines represent the fitting result using Eq. (1).

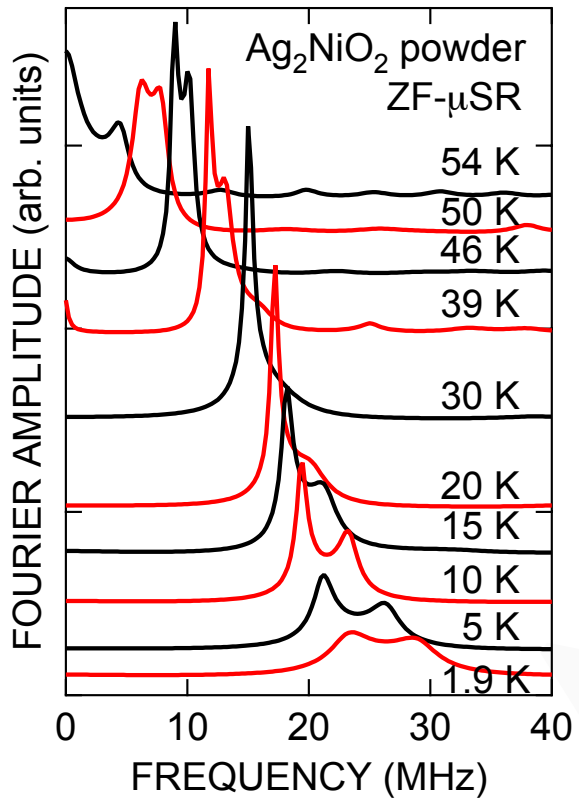


Fig. 2. Temperature dependence of the Fourier ransform of the ZF-$\mu^+$SR time spectrum for $Ag_2NiO_2$.

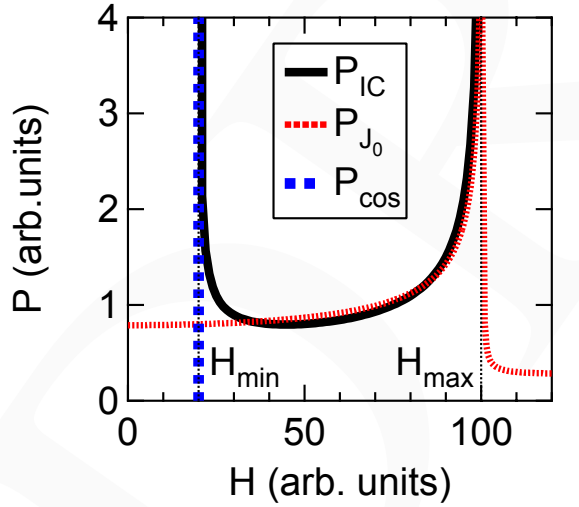


Fig. 3. The distribution of the magnitude of the magnetic field $H$ due to a generic incommensurate magnetic structure described in the text. The distribution corresponding to a Bessel function $J_0(\omega_2 t)$ and a $\cos(\omega_1 t)$ are also plotted for comparison. Here, $\gamma_\mu H_{\max} = \omega_2$ and $\gamma_\mu H_{\min} = \omega_1$.

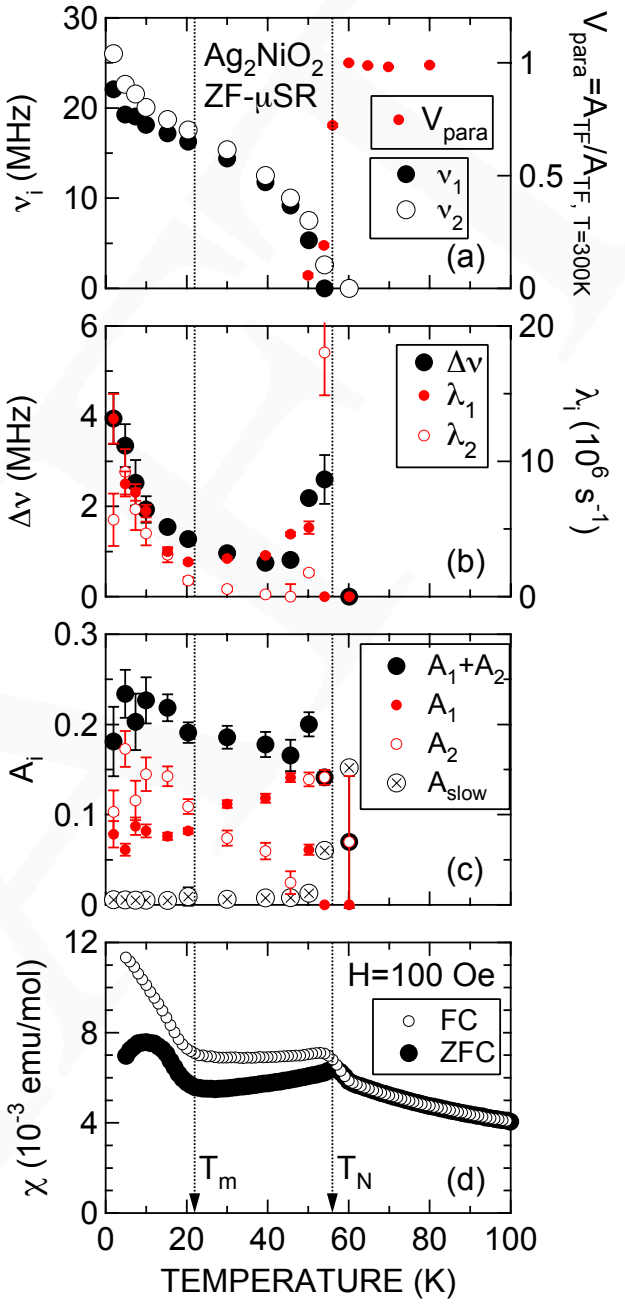


Fig. 4. Temperature dependences of (a) the muon precession frequencies ($\nu_i = \omega_{\mu,i}/2\pi$) and normalized transverse field asymmetry that roughly corresponds to the volume fraction of the paramagnetic phases in the sample ($V_{\rm para}$), (b) $\Delta\nu = \nu_2 - \nu_1$, $\lambda_1$ and $\lambda_2$, (c) the asymmetries $A_1+A_2$, $A_1$, $A_2$ and $A_{\rm slow}$ and (d) $\chi$ for the powder sample of $Ag_2NiO_2$. $\chi$ was measured in zero-field-cooling (ZFC) and field-cooling (FC) mode with $H = 100$ Oe.

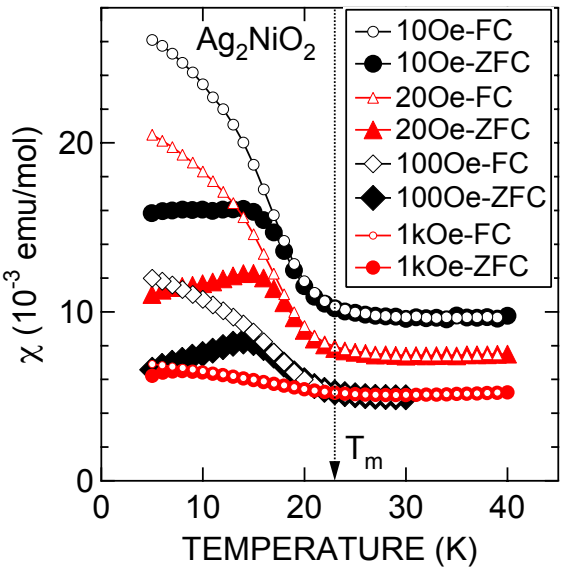


Fig. 5. Temperature dependence of $\chi$ measured in both ZFC and FC mode well below $T_N = 56$ K with $H = 10$ Oe, 20 Oe, 100 Oe and 1 kOe for $Ag_2NiO_2$.

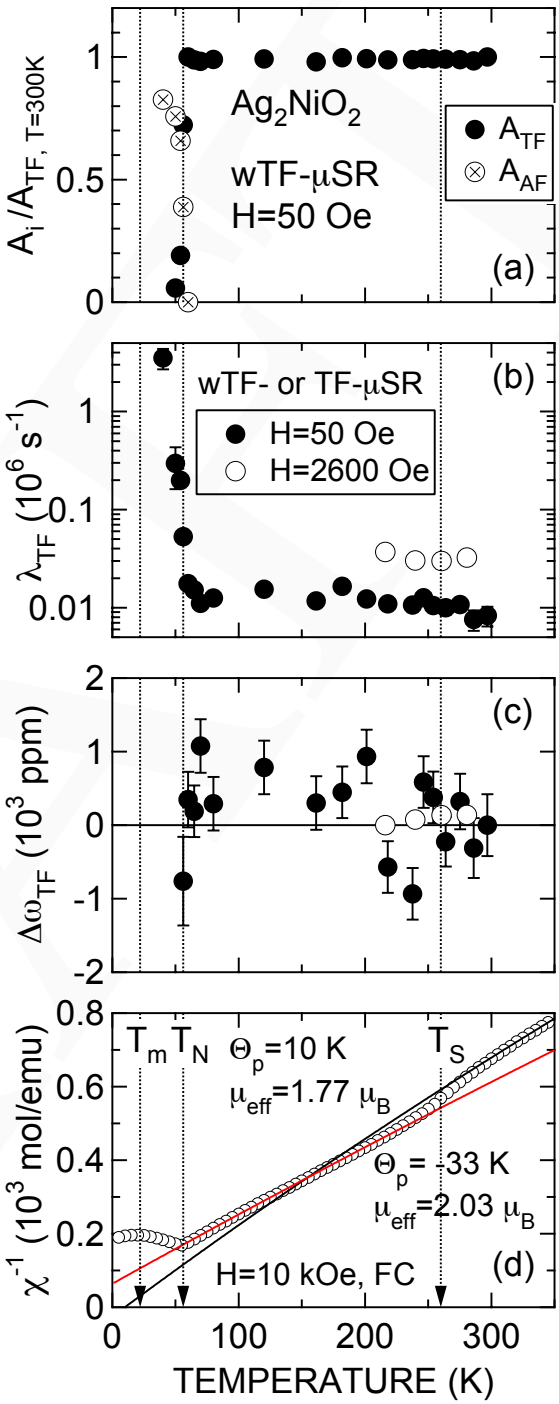


Fig. 6. Temperature dependences of (a) the normalized $A_{TF}$ and $A_{AF}$, (b) $\lambda_{TF}$, (c) the shift of the muon precession frequency, $\Delta\omega_{\mu,TF}$ and (d) the inverse susceptibility, $\chi^{-1}$ in the $Ag_2NiO_2$ powder. The wTF and TF data were obtained by fitting using Eq. (3). $\chi$ was measured in *FC* mode with $H = 10$ kOe. The paramagnetic Curie temperature ($\Theta_p$) and the effective magnetic moment of Ni ions ($\mu_{eff}$) are calculated above and below $T_S$ by the Curie-Weiss law in the general form; $\chi = C(T - \Theta_p)^{-1} + \chi_0$.

**Experiment 1051**
**Muonium and muoniated free radical formation and reactivity in ionic liquids**
*(K. Ghandi, Mount Allison)*

Industries now are trying to change their processes to use environmentally friendly or "green" solvents such as ionic liquids. Yet there is significant lack of thermodynamic and kinetic data on chemical reactions in these green solvents. Knowledge of reaction mechanisms, rates and molecular motion of radicals is important for understanding processes that use free radicals. Our focus is to study free radicals and chemical reactions in ionic liquids. Our experimental tools include a range of techniques used at TRIUMF. This approach is being reinforced with theoretical modelling in order to apply experimental results to industrially relevant and complex systems. The ultimate goal of this project is to *generate* and *detect* free radicals and subsequently determine their reactivity and dynamics in ionic liquids in pure form or mixtures with green molecular solvents over as wide a range of temperature as feasible. To work towards this goal we began an initial study aimed at characterizing possible free radicals formed in ionic liquids by measuring their hyperfine interactions. We showed that it is possible to form free radicals in a phosphonium ionic liquid and investigated the free radical formation by both TF-$\mu$SR and ALCR methods. We have also developed experimental techniques needed to work with the ionic liquids.

Radicals from addition to benzene (Mu-cyclohexadienyl), toluene and 1,3,5 tert-butyl benzene in phosphonium ionic liquid tetradecyl (trihexyl) phosphonium chloride (Fig. 1), formed by Mu addition to the double bond in these solutes, were investigated by both TF-$\mu$SR and ALC-$\mu$SR mostly at room temperature except for solutions of benzene which has been studied over a range of temperatures. (From now on the ionic liquid tetradecyl (trihexyl) phosphonium chloride that was used for this experiment will be called IL 101, its commercial name.)

Preparation of the samples included purification of ionic liquids, dissolving the double bonded solutes in the ionic liquid and freeze/pump/thaw cycles, to remove the residual oxygen, on our vacuum line at Mount Allison University, and sealing of the sample cells designed for these types of experiments from non-magnetic stainless steel. The samples were sealed in a glove box under argon atmosphere. Several solutions were used in this experiment to test the possibility of studying free radicals in ionic liquids by $\mu$SR. The solutions were 1.4 M benzene in ionic liquid, in ionic liquid with a trace of water ($\sim$0.05%), in propanol, 0.7 M benzene in ionic liquid and in n-heptayne and 0.7 M 1,3,5 tri-tertiary butyl benzene in ionic liquid and in propanol and in hexane. The experiments on solutions in molecular liquids were for comparison with ionic liquids.

Results are incomplete with ALC-$\mu$SR and TF-$\mu$SR at only a few temperature points. Both the benzene and toluene solutions in the ionic liquid IL 101 need further study using ALC-$\mu$SR and TF-$\mu$SR, in order to obtain all relevant hyperfine coupling and dynamics information of these radicals in this ionic liquid.

Our studies in benzene were from 298 to 341 K. The temperature range of studies of 1,3,5-tri-*tert*-butyl benzene in the ionic liquid is from 60 to 125°C. The studies at upper limit of the temperature range were restricted by the circulating liquid used to control the temperature. The upper limits of temperatures in molecular liquids are due to their boiling point, e.g. in propanol we were limited to 85°C. This shows the complementary nature of our studies in ionic liquids to the studies in molecular solvents and also it demonstrates the broad range of temperature available to study free radical chemistry in ionic liquids.

Despite our limited data due to relatively short beam time, we have some significant results, described in the following. We detected non-persistent (reactive) free radicals in a phosphonium ionic liquid. As an example of our data, the TF spectrum obtained for the Mu-cyclohexadienyl radical in IL 101 is shown in Fig. 2 in comparison to the data in a molecular solvent at the exact same conditions with the same FT parameters and scale. The pair of peaks (in IL 101) is due to the radical with a muon hyperfine coupling constant of 515 MHz. At low concentrations our data showed that free radical product from addition to a solute with the double bond in the ionic liquid is much more favoured as compared to molecular solvents.

The LCR resonance of the same radical in the ionic liquid, corresponding to the methylene (CHMu) group, is shown in Fig. 3.

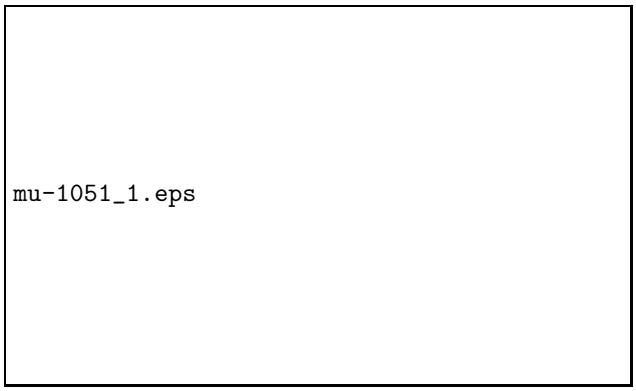


Fig. 1. The trihexyl (tetradecyl) phosphonium chloride ionic liquid (IL 101).

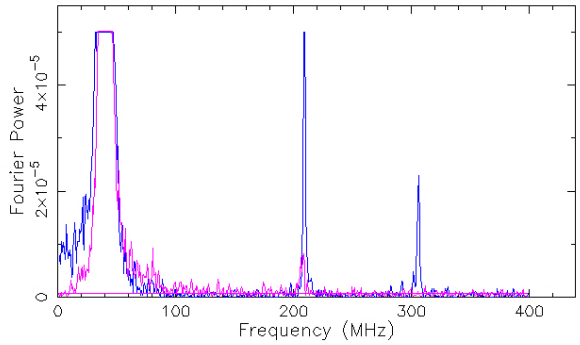


Fig. 2. The TF-$\mu$SR spectrum of 0.7 M solution of benzene in n-heptane (pink) and IL 101 (red). The temperature and magnetic field is the same. The scale of the $y$ axis is the same in both figures.

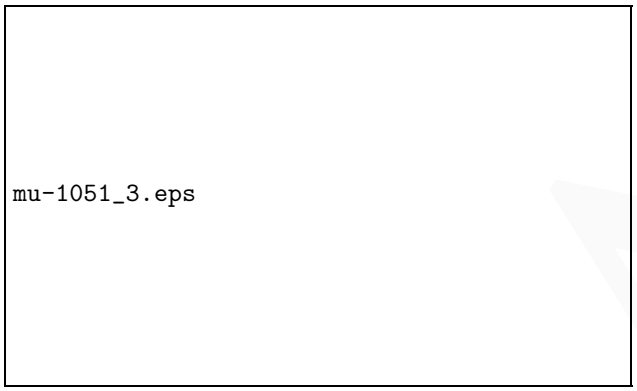


Fig. 3. An LCR spectrum of $C_6H_6Mu$ radical in trihexyl (tetradecyl) phosphonium chloride ionic liquid at room temperature. The resonance is due to coupling to methylene (CHMu) proton.

## Experiment 1052
## $\mu$SR studies in MnSi under applied pressure

*(Y.J. Uemura, Columbia; T. Goko, Tokyo Univ. of Science)*

### Suppression of critical dynamics in MnSi in quantum magnetic phase transitions

MnSi is a weak helical magnet based on itinerant electrons which orders with a very long helical spin modulation of 180 Å below $T_c \sim 30$ K at ambient pressure. Previous $\mu$SR studies have shown that dynamic spin fluctuations of this system can be described well by the self consistent renormalization theory of Moriya and co-workers. In the late 1990's, Pfleiderer *et al.* of Cambridge showed that the magnetic order can be suppressed by the application of hydrostatic pressure, with the critical pressure $p_c$ of 15 kbar above which the ordered moment disappears. Temperature dependence of transport properties above $p^* \sim 12$ kbar exhibits history dependence. Short range correlations of spin fluctuations have also been detected at $p > p^*$ by neutron studies of Pfleiderer *et al.*

In the last year's Annual Report, we reported our results of $\mu$SR measurements in weak transverse field (WTF) at applied pressure up to 15 kbar. The volume fraction $V_M$ of the magnetically ordered region at $T \to 0$ start decreasing from 100% with increasing pressure at $p > p^*$, and $V_M(T \to 0)$ finally become zero for $p > p_c$. This clearly implies phase separation in quantum phase transition (QPT) at the boundary between helically ordered and paramagnetic phases. Similar behaviour was also observed in another itinernant ferromagnet (Sr,Ca)$RuO_3$ in ambient pressure as a function of (Sr,Ca) substitution.

In 2006, we performed further $\mu$SR measurments in longitudinal external field (LF) of 200 G, which was applied to decouple the effect of nuclear dipolar fields. Figure 1 shows the relaxation rate $1/T_1$ observed as a function of temperature at several selected pressures. The divergent behaviour of $1/T_1$ becomes weaker with increasing pressure. Between $p^* < p < p_c$, we do not see any anomaly of $1/T_1$ at $T_c$, and the relaxation rate becomes smaller than our detection limit (indicated by the broken line) for a pressure above $p_c$. These results reinforce the view that the QPT of MnSi is achieved in a first order phase transition.

These results of ZF, WTF, and LF $\mu$SR measurements in MnSi and (Sr,Ca)$RuO_3$ will been published as an article in the January, 2007 issue of Nature Physics [Uemura *et al.*, Nature Phys. **3** (in press)]. As we pointed out in this article, not only in itinerant-electron magnet systems, but also in heavy fermion and HTSC systems, QPTs in the overwhelming majority of cases are associated with discontinuous changes, phase separation and/or suppression of dynamical critical behaviours. It would be very interesting to develop theoretical discussions on the origin of this behaviour and on the possibly important role played by soft collective mode excitations [Uemura *et al.*, Physica **B374-375**, 1 (2006)] at/near QPTs of correlated electron systems. In the future, we are planning to extend this study to cover the effect of high applied field in MnSi, as well as to perform further studies of QPTs in (Mn,Fe)Si, (Fe,Co)Si, and some other itinerant weak ferromagnet systems.

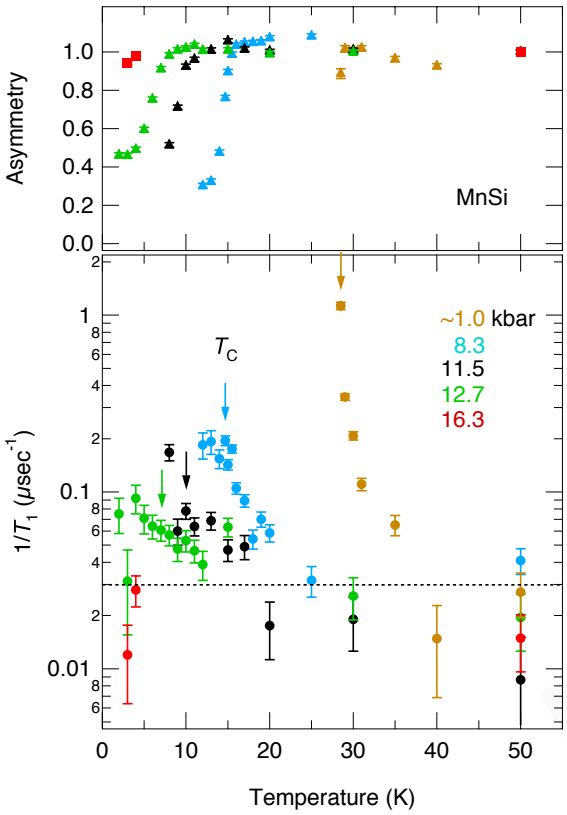


Fig. 1. The muon spin relaxation rate $1/T_1$ and the relative magnitude of the corresponding muon asymmetry in MnSi in a longitudinal field (LF) of 200 G. Divergent critical behaviour of $1/T_1$, seen at $p \sim 1$ kbar, is gradually suppressed with increasing pressure. No anomaly of $1/T_1$ is seen at $T_c$ (indicated by arrows) at $p = 12.7$ kbar ($p^* < p < p_c$). At $p = 16.3$ kbar, $1/T_1$ becomes smaller than the technical limit of detection, indicated by the broken line.

### Experiment 1053
### $\mu$SR studies of $S = 0$ doped inorganic spin Peierls system $Ti_{1-x}Sc_xOCl$

*(T. Imai, G. Luke, McMaster)*

Spin $S = \frac{1}{2}$ chain material TiOCl recently emerged as a new inorganic model spin-Peierls system. Unlike $CuGeO_3$, the uniform spin susceptibility fits quite nicely with the nearest neighbour Heisenberg model. This means that we may consider the spin-Peierls transition at $T_c = 95$ K (or, the incommensurate transition to be more precise) a much cleaner one-dimensional phenomenon than in $CuGeO_3$. In fact, both NMR and Raman measurements showed a clear evidence for lattice softening high above $T_c$. Our primary goals are (a) to establish a magnetic phase diagram of $Ti_{1-x}Sc_xOCl$ in the presence of spin $S = 0$ doped into the $S = \frac{1}{2}$ Ti sites, and (b) to shed a new microscopic light on the interplay between the magnetic moments induced by Sc ions and the spin-Peierls distortion of the lattice. We use $^{35}$Cl NMR to observe the temperature dependence of the nuclear quadrupole interaction, which reflects the lattice distortion.

We conducted one week of $\mu$SR experiments during the fall for Sc doping concentration $x = 0.01$ and $x = 0.03$. Our preliminary analysis showed that the relaxation rate begins to grow below ~100 K. Moreover, the relaxation rate nearly saturates below $10 \sim 15$ K, but the time evolution is always overdamped and never shows the signature of a magetic long range order. Our finding is in remarkable contrast with the case of doped $CuGeO_3$, in which a long range Néel ordering was readily observed at any doping concentration.

We are in the process of further data analysis, and also plan to conduct more ZF and TF measurements to understand the dynamics of spin fluctuations in $Ti_{1-x}Sc_xOCl$.

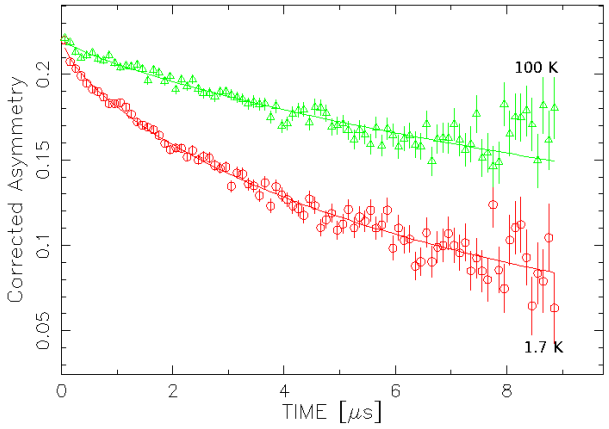


Fig. 1. Two representative ZF-$\mu$SR spectra observed for $Ti_{0.97}Sc_{0.03}OCl$. Notice that no precession is observed even at the base temperature.

### Experiment 1079
### Spin liquid state in the square-lattice antiferromagnet $(CuCl)LaNb_2O_7$ and related compounds

*(H. Kageyama, Kyoto; Y.J. Uemura, Columbia; G.M. Luke, McMaster)*

Geometrical spin frustration in low-dimensional quantum spin systems gives rise to unusual quantum phenomena such as spin liquids. From an experimental point of view, however, such spin liquid states are mostly realized in quasi-one-dimensional systems (e.g., $CuGeO_3$, $SrCu_2O_3$). However, spin liquids also appear in 2D systems as well, such as the Kagomé lattice. The frustrated two-dimensional square lattice system, the so-called $J_1$–$J_2$ model, is the most interesting system in relevance to the RVB concept proposed after the discovery of high-$T_c$ superconductivity.

We demonstrated from the magnetic susceptibility, magnetization curve and neutron elastic/inelastic scattering experiments that a double-layered perovskite

$(CuCl)LaNb_2O_7$ is a new class of 2D Heisenberg spin system, where a spin-singlet ground state with a finite energy gap ($\Delta = 2.3$ meV) is achieved in an $S = \frac{1}{2}$ frustrated square lattice, while its isostructural Br-based counterpart $(CuBr)LaNb_2O_7$ exhibits a stripe magnetic order at 32 K. Although some analysis of the temperature dependence of the magnetic susceptibility and high-field magnetization data suggests that both compounds have competing antiferromagnetic and ferromagnetic interactions, the origin of the spin-singlet formation as well as the relevance of $J_1$–$J_2$ model remain to be solved.

We carried out $\mu$SR experiments at the M15 and M20 beam lines, based on the proposal of Expt. 1079. From the temperature dependence of $\mu$SR spectra of $(CuCl)LaNb_2O_7$ for $T > 2$ K, we found very weak relaxation with a Gaussian peak shape. The observed slow relaxation is comparable to that of the two-leg ladder system $SrCu_2O_3$. Figure 1 shows LF decoupling measurements at 2 K, demonstrating that the $\mu$SR spectrum becomes flattened in a LF $\sim$50 G, indicating the static nature of the spectra. The spectra at 15 mK and 2 K are essentially the same, providing firm evidence that the spin-singlet ground state is realized in this compound.

Figure 2 shows that the static magnetic order of $(CuBr)LaNb_2O_7$ starts to set in around $T = 32$ K. The volume fraction of the ordered region increases with decreasing temperature towards $T = 25$ K, below which the full volume of the system exhibits static magnetism. We have analyzed the data by assuming three types of signals:

(a) oscillating signal
(b) fast relaxing signal
(c) slow decay signal

(a) and (b) represent muons stopped where the local field is perpendicular to the initial muon polarization direction, while (c) represents muons whose local field is parallel to the initial polarization direction. Usually, we expect (a) + (b) to have about $\frac{2}{3}$ of the total asymmetry and (c) to have $\frac{1}{3}$, in the magnetically ordered state. In the paramagnetic state, we will only see (c). In our measurements, the total asymmetry, which can be derived from the weak transverse field measurements, is about 0.24–0.25. So, we expect (c) to contribute about 0.08 to the asymmetry. The actual asymmetry of the "slow" (c) component is about 0.11 at low temperatures. We would guess that about 10% of the total muons have been stopped in the surroundings or counters, and contribute to background, apparently increasing the slowly decaying component (c). The volume fraction of the magnetically ordered region increases sharply below $T = 32$ K, and saturates at around $T = 28$ K.

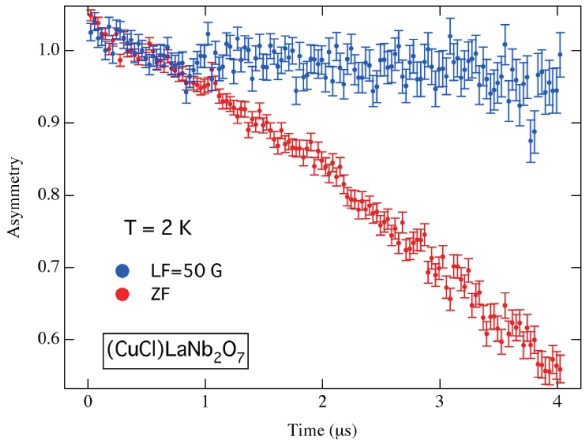


Fig. 1. Longitudinal field decoupling measurements at 2 K for $(CuCl)LaNb_2O_7$.

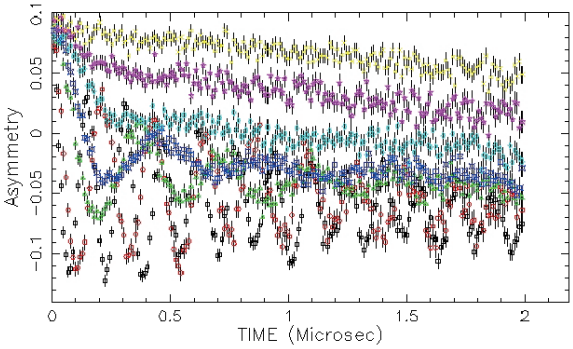


Fig. 2. Zero-field mSR spectra of $(CuBr)LaNb_2O_7$.

**Experiment 1080**
**Full phase diagram of $Na_xCoO_2$**
*(J. Sugiyama, Toyota CRDL Inc.; J.H. Brewer, UBC-TRIUMF)*

The phase diagram of the $Na_xCoO_2$ (NCO) system is a solid state physics treasure trove, because of a variety of magnetic phases that appear as a function of $x$: long-range antiferromagnetic (AF) order with $T_N \sim 22$ K for NCO with $x \geq 0.75$ [Sugiyama *et al.*, Phys. Rev. **B67**, 214420 (2003); Bayrakci *et al.*, Phys. Rev. Lett. **94**, 157205 (2005)]; two successive AF transitions ($T_{N_1} = 87$ K and $T_{N_2} = 53$ K) in NCO with $x = 0.5$ [Foo, *et al.*, Phys. Rev. Lett. **92**, 247001 (2004)]; and superconductivity with $T_C = 5$ K for NCO with $x = 0.35$ and absorbed water [Takada, *et al.*, Nature **422**, 53 (2003)]. All these magnetic behaviours are considered to be influenced by geometrical frustration in the two-dimensional (2D) triangular lattice formed by edge-sharing $CoO_6$ octahedra in the $CoO_2$ planes.

The AF order of $Na_{0.5}CoO_2$ appears to be an isolated island in the narrow $x$ range between a metallic Pauli paramagnet ($0.3 < x < 0.5$) and a Curie-Weiss

metal ($0.5 < x < 0.75$), although the phase boundary of the AF phase is still unknown. Since resistivity ($\rho$) measurements [Foo *et al., op. cit.*] and TEM observations [Zandbergen, *et al.*, Phys. Rev. **B70**, 024101 (2004)] on $Na_{0.5}CoO_2$ indicated charge-ordering in the $CoO_2$ plane probably due to the order of Na ions, the origin of the AF order was naturally explained using this model. The Na-ordering also reduces the symmetry of $Na_{0.5}CoO_2$ from hexagonal to orthorhombic even at 295 K, due to the formation of Na zig-zag chains [Zandbergen *et al., op. cit.*]. As expected from the layered structure of NCO, $Na_{0.5}CoO_2$ is highly anisotropic: the $\chi_{ab}(T)$ curve exhibits a clear change in slope ($d\chi/dT$) at both $T_{N_1}$ and $T_{N_2}$, whereas the $\chi_c(T)$ curve only changes slope at $T_{N_2}$ [Yokoi *et al.*, J. Phys. Soc. Jpn. **74**, 3046 (2005)]. Here $\chi_{ab}$ and $\chi_c$ are $\chi$ measured under $H \perp c$ and $H \parallel c$, respectively. However, as $T$ decreases from high $T$, the $\rho_{ab}(T)$ curve exhibits a rapid increase at $T_{N_2}$ without any clear anomalies around $T_{N_1}$ [Yokoi *at al., op. cit.*].

Past $\mu^+$SR experiments on a powder $Na_{0.5}CoO_2$ sample showed the existence of three different internal magnetic fields ($H_i^{\rm int}$) below $T_{N_1}$ [Mendels *et al.*, Phys. Rev. Lett. **94**, 136403 (2005)]. From these three $H_i^{\rm int}(T)$ curves, it was postulated that reorientation of AF coupled moments occurs at both $T_{N_2}$ and 29 K without direct experimental evidence. Recently the AF magnetic structure was determined at 8 K by a neutron scattering experiment using a single crystal of $Na_{0.5}CoO_2$ [Gašparović *et al.*, Phys. Rev. Lett. **96**, 046403 (2006)]: in the alternating arrangement of $Co^{3+}$ ($S = 0$) and $Co^{4+}$ ($S = 1/2$) chains along the $b$-axis, the neighbouring $Co^{4+}$ spins, which are parallel to the chain ($a$-axis), are coupled antiferromagnetically. In contrast to the results of $\mu^+$SR, $\chi_{ab}$ and $\rho_{ab}$ measurements, the $T$ dependences of the AF Bragg peaks indicate that there are no crucial changes in magnetic structure at $T_{N_2}$ and 29 K.

In order to solve the discrepancy concerning the nature of the AF phase, we measured the $T$ dependence of not only $H_i^{\rm int}$ but also the angle of $\mathbf{H}_i^{\rm int}$ relative to the $ab$-plane by means of $\mu^+$SR using single crystals of $Na_{0.5}CoO_2$. Here we clearly demonstrate the reorientation behaviour at both $T_{N_2}$ and 35 K.

The $\mu^+$SR experiments were performed on the M20 surface muon beam line at TRIUMF. Five crystals were arranged in a mosaic in an active-muon-veto sample holder with their $c$ axes parallel to the beam direction $z$ as defined in Fig. 1. Muon-spin rotation and relaxation spectra were obtained in zero applied field (ZF) with four positron detectors (backward (B), forward (F), up (U) and down (D)) arranged as shown in Fig. 1.

Figure 2 shows ZF-$\mu^+$SR time spectra and their Fourier transforms (FTs) at 2.1 K, 20 K, 40 K and 60 K for the crystals of $Na_{0.5}CoO_2$. The top spectrum was obtained in SR mode by U and D counters ($A_0\,{}^xP_z(t)$), while the bottom spectrum was obtained in NSR mode by B and F counters ($A_0\,{}^zP_x(t)$). Here $A_0$ is the empirical maximum muon decay asymmetry, ${}^mP_n(t)$ is the muon spin polarization; $m$ is the direction of $\mathbf{S}_\mu(0)$ and $n$ denotes the direction of $\mathbf{H}_i^{\rm int}$. A clear oscillation due to quasi-static $\mathbf{H}_i^{\rm int}$ is observed in all four spectra, unambiguously establishing the existence of coherent magnetic order in the sample.

The FTs of the ZF-spectra indicate that there are at least five oscillatory signals in $A_0\,{}^xP_z(t)$ and two in $A_0\,{}^zP_x(t)$; four peaks and one shoulder around 2.1 MHz at 20 K, clearly showing the anisotropic nature of the magnetic order. Indeed the ZF-$\mu^+$SR spectra were well fitted by a combination of five oscillatory signals with a common phase and a slowly relaxing non-oscillatory signal:

$$A_0\,{}^mP_n(t) = \sum_{i=1}^{5} {}^mA_{n,i}\,\cos(\omega_i^\mu t + \phi_n)\,\exp\left[-\frac{\sigma_i^2 t^2}{2}\right] + {}^mA_{n,\rm tail}\,\exp(-\lambda_{\rm tail}\,t)$$

where $\{m, n\} = \{x \text{ or } z\}$, $\phi_n$ is the initial phase of the precession, ${}^mA_{n,i}$ are the asymmetries, $\sigma_i$ ($i = 1{-}5$) are Gaussian relaxation rates, and $\omega_i^\mu$ are the muon Larmor frequencies of the five signals. The angle ($\theta_i$) between $\mathbf{H}_i^{\rm int}$ and the $ab$-plane is defined by ${}^xA_{z,i}/\,{}^zA_{x,i} = \tan\theta_i$.

Figure 3 shows that the Fourier transform spectrum of $A_0\,{}^xP_z(t)$ depends strongly on $T$ below 85 K: above 50 K, the spectrum consists of two sharp peaks; for $15 \le T < 50$ K it splits into up to five peaks; and below 15 K the peak around 1.6 MHz is dominant, with two or three side-peaks. This behaviour is similar to that observed for $K_{0.49}CoO_2$ crystal platelets [Sugiyama *et al.*, Phys. Rev. Lett. **96**, 037206 (2006)].

Figures 4(a)–(d) show the $T$ dependence of the muon precession frequencies $\nu_i = \omega_i^\mu/2\pi$, the asymmetries ${}^xA_i$ and the angle $\theta_i$, together with $\chi(T)$. Like the Fourier spectra shown in Fig. 3, the five $\nu_i(T)$ curves exhibit a complex $T$ dependence. As $T$ increases from 2 K, $\nu_3$, $\nu_4$, and $\nu_5$ monotonically decrease and disappear around $T_{N_2}$, 75 K and $T_{N_1}$, respectively. Meanwhile, $\nu_1$ decreases with increasing $T$ and reaches its minimum around 35 K, above which it rises again, exhibiting a broad maximum around 65 K, and finally disappears at $T_{N_1}$. The $\nu_2(T)$ curve shows a similar behaviour: $\nu_2$ appears suddenly around 15 K, reaches a minimum at $T_{N_2}$ and has a broad maximum at 65 K. The overall $T$ dependences of $\nu_i$ are quite similar to those reported using a powder sample [Mendels *et al.*,

*op. cit.*]

The dominant signal at low $T$ is ${}^xA_3$, but as $T$ increases, ${}^xA_3$ decreases and disappears at $T_{N_2}$. Above $T_{N_2}$, ${}^xA_1$, ${}^xA_2$ and ${}^xA_5$ are dominant instead. The signal with the highest $\nu$, i.e., ${}^xA_5$, has a small amplitude below $T_{N_2}$. In order to explain the ${}^xA_i(T)$ curves, one could consider changes in muon sites, and a situation whereby the population of $\mu^+$ at each site is entirely changed at $T_{N_2}$. Such behaviour is very unlikely to occur at low $T$ especially in oxides. The angle $\theta_1$ decreases gradually from 90° as $T$ increases from 2 K, almost reaches 0 around 35 K, and then rapidly recovers up to 90° at ∼50 K, above which $\theta_1$ is independent of $T$. The $\theta_2(T)$ curve behaves similarly, but has its minimum around $T_{N_2}$. The minimum in the $\nu_1(T)$ ($\nu_2(T)$) curve thus indicates a rotation of $\mathbf{H}_1^{\rm int}$ ($\mathbf{H}_2^{\rm int}$). The angle $\theta_3$ of the dominant signal below $T_{N_2}$ decreases slowly from ∼80° to ∼70° with increasing $T$ from 2 K to $T_{N_2}$. Angle $\theta_5$ looks almost $T$ independent and varies between 30° and 40° up to $T_{N_1}$. The $T$ dependence of $\theta_4$ is unclear above $T_{N_2}$, because the signal is very weak (${}^xA_4 \sim 0$). Ignoring the values around 10 K, the $\theta_4(T)$ curve is roughly similar to the $\theta_5(T)$ curve.

The three main signals (corresponding to $\mathbf{H}_1^{\rm int}$, $\mathbf{H}_2^{\rm int}$, and $\mathbf{H}_3^{\rm int}$) are almost perpendicular to the *ab*-plane, although $\mathbf{H}_1^{\rm int}$ and $\mathbf{H}_2^{\rm int}$ rotate rapidly by ∼90° at 35 K and $T_{N_2}$. The two minor signals (corresponding to $\mathbf{H}_4^{\rm int}$ and $\mathbf{H}_5^{\rm int}$) are found to be canted by about 30° relative to the *ab*-plane. Since the initial phase is almost 0 for the all signals, the five signals obviously suggest the existence of five inequivalent muon sites in the $Na_{0.5}CoO_2$ lattice. Among them, the $\mathbf{H}_5^{\rm int}$ signal probably corresponds to the AF signal detected by neutron experiments, because of the lack of rotation and its order-parameter-like $T$ dependence of $\nu_5$ below $T_{N_1}$ [Gašparović *et al., op. cit.*].

At 8 K (in the charge-order state), it is reported that $Co^{4+}$ is located at the same position in adjacent $CoO_2$ planes but $Co^{4+}$ spins are coupled antiferromagnetically along both *a*- and *c*-axis (see Fig. 5(a)) [Gašparović *et al., op. cit.*]. According to the dipole field calculation shown in Figs. 5(b) and (c), the muons at sites No. 2 and 5 with $z = 0.075$ experience $\mathbf{H}_i^{\rm calc}$ with $\Theta_i^{\rm calc} \sim 30$ and 40°, whereas the muons at site No. 3 experience $\Theta_3^{\rm calc} = 90°$ in the whole $z$ range ($0.075 \le z \le 0.25$). Making comparison between $\mathbf{H}_i^{\rm int}$ and $\mathbf{H}_i^{\rm calc}$, the measured five $\mathbf{H}_i^{\rm int}$ at 1.8 K are assigned as follows:

$\mathbf{H}_1^{\rm int}$: site No. 3 with $z$=0.25,
$\mathbf{H}_3^{\rm int}$: site No. 3 with $z$=0.075,
$\mathbf{H}_4^{\rm int}$: site No. 2 with $z$=0.075, and
$\mathbf{H}_5^{\rm int}$: site No. 5 with $z$=0.075.

Here we assume that the stable muon sites are either at $z = 0.075$ (in the vicinity of the $CoO_2$ plane and bound to oxygen) or at $z = 0.25$ (Na vacancies).

The origin of the dynamic changes in $\mathbf{H}_i^{\rm int}$ and $\theta_i$ at $T_{N_2}$ is most likely to be caused by the change in the stable muon sites due to the charge-order. Note that, above $T_{N_2}$ (without the charge-order), site No. 1 becomes electrostatically equivalent to site No 6, site No. 2 to site No. 4, and site No. 3 to site No. 5 and 7 (see Fig. 5(a)). Actually, only three $\mathbf{H}_i^{\rm int}$ are observed above $T_{N_2}$. In order to explain the whole $T$ dependences of $\mathbf{H}_i^{\rm int}$ and $\theta_i$, however, we need a more accurate dipole field calculation, and such attempt is in progress.

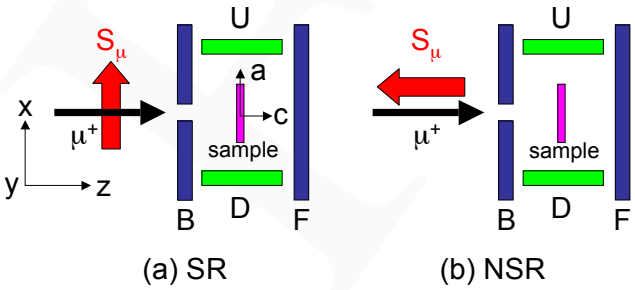


Fig. 1. Geometry of the $\mu^+$SR experiment: four counters (backward (B), forward (F), up (U) and down (D)) detect decay positrons emitted in the $-z$, $+z$, $+x$ and $-x$ directions, respectively. The initial muon spin direction $\mathbf{S}_\mu(0)$ is in the $+x$ direction ($\parallel \hat{\mathbf{a}}$ of the crystals) for spin-rotated (SR) mode (a) or in the $-z$ direction ($\parallel \hat{\mathbf{c}}$) for non-spin-rotated (NSR) mode (b). Thus if the internal magnetic field ($\mathbf{H}_i^{\rm int}$) is parallel to $\hat{\mathbf{c}}$, only U and D counters will detect a muon spin oscillation, and that only in SR mode; but if $\mathbf{H}_i^{\rm int} \parallel \hat{\mathbf{a}}$, only B and F counters in NSR mode will show an oscillatory signal.

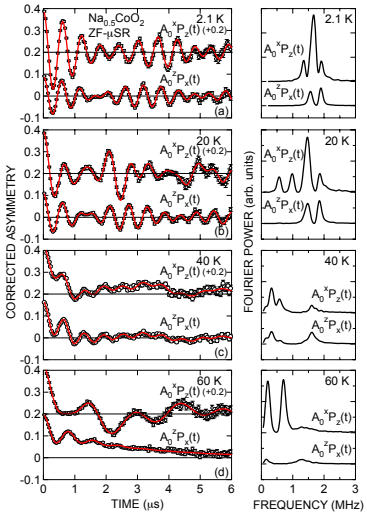


Fig. 2. ZF-$\mu^+$SR time spectra at (a) 2.1 K, (b) 20 K, (c) 40 K, and (d) 60 K for $Na_{0.5}CoO_2$ crystals. Top: $A_0\,{}^xP_z(t)$, bottom: $A_0\,{}^zP_x(t)$. Top spectrum is offset by 0.2 for display clarity. Solid lines represent fits using the equation. The right panel shows Fourier transforms of the ZF time spectra.

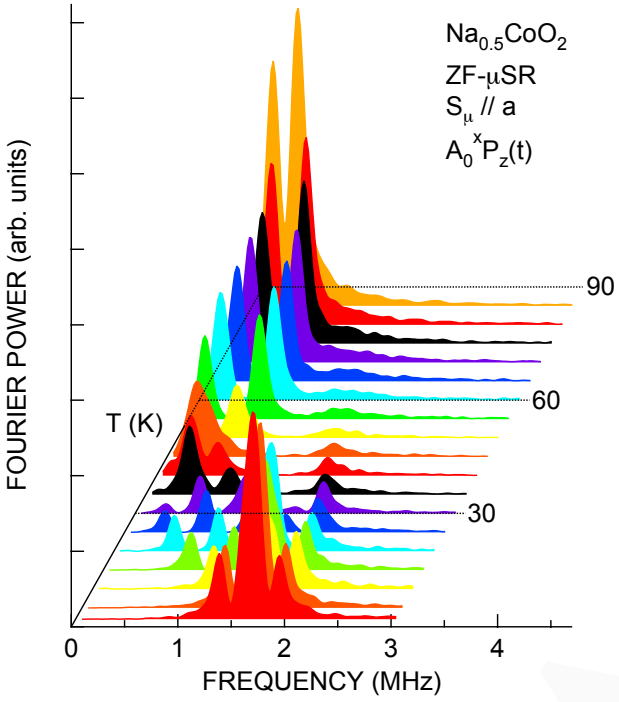


Fig. 3. Temperature dependence of the Fourier transform of the ZF-$\mu^+$SR time spectrum $A_0\,{}^xP_z(t)$ for $Na_{0.5}CoO_2$.

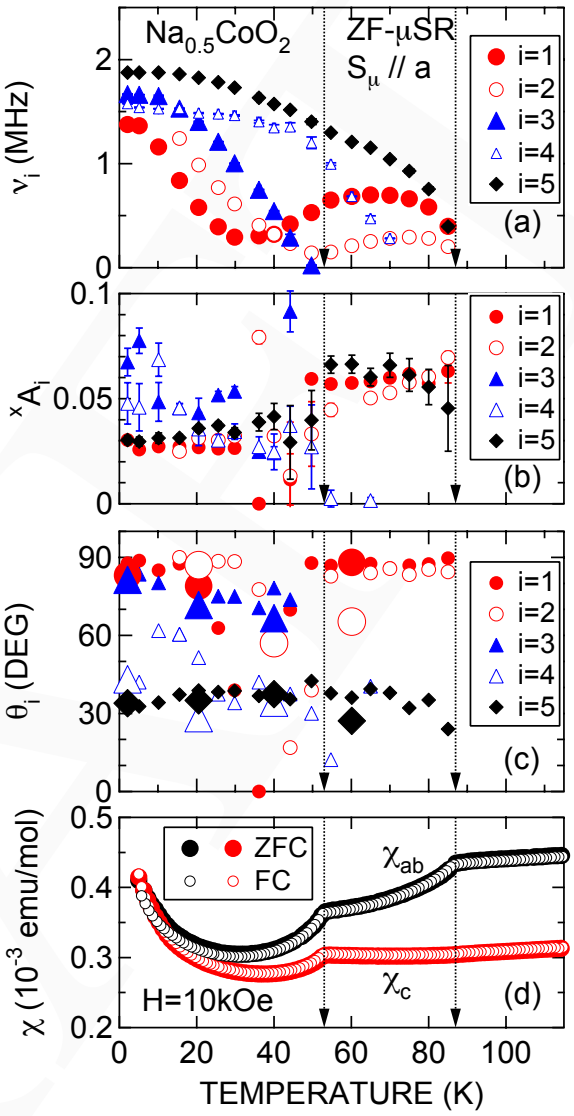


Fig. 4. $T$ dependences of (a) muon precession frequencies $\nu_i$, (b) asymmetries ${}^xA_i=\sqrt{{}^xA_{x,i}^2 + {}^xA_{z,i}^2}$, (c) angle $\theta_i$ between $\mathbf{H}_i^{\rm int}$ and the $ab$-plane, and (d) $\chi_{ab}$ and $\chi_c$ for $Na_{0.5}CoO_2$. In (c), large symbols represent data estimated from $A_0\,{}^xP_z(t)$ and $A_0\,{}^zP_x(t)$, whereas small symbols represent data estimated from $A_0\,{}^xP_z(t)$ and $A_0\,{}^xP_x(t)$; here $A_0\,{}^xP_x(t)$ appears as $\mathbf{S}_\mu(0)$ and is not 90° but 80–85° relative to $z$ direction in SR mode.

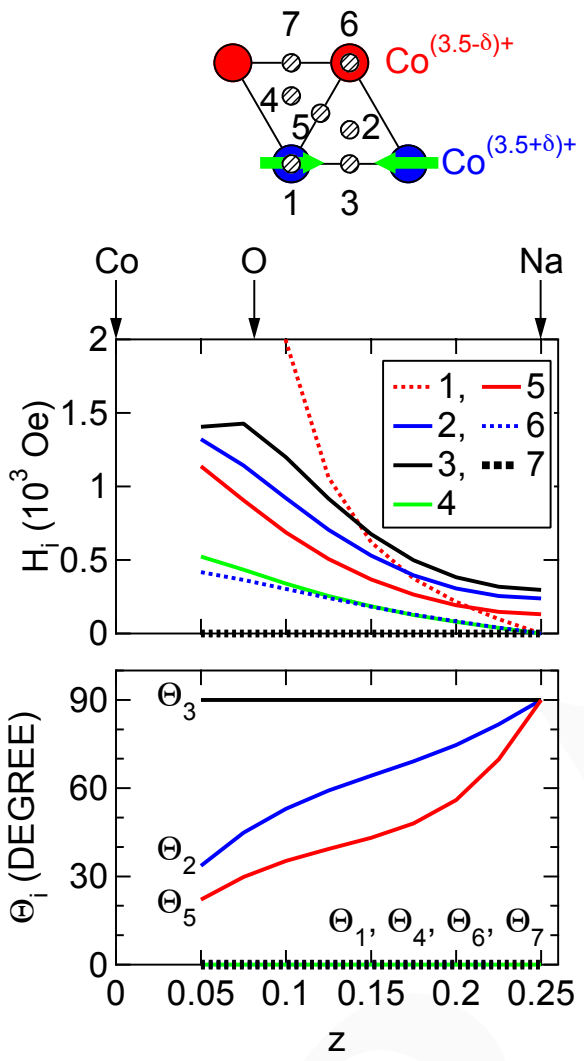


Fig. 5. The result of the dipolar field calculation for possible muon sites using the magnetic moment of $Co^{3.5+\delta}$ $\hat{\mathbf{m}}_{Co} = (\pm 1\ \mu_B,\ 0,\ 0)$. (a) muon sites, (b) the relationship between $z$ and calculated internal magnetic fields $\mathbf{H}_i^{calc}$, and (c) calculated angles $\Theta_i^{calc}$.

**Experiment 1082**
**Muonium defect energies in SiGe alloys**
*(P.J.C. King, Rutherford Appleton Lab; R.L. Lichti, Texas Tech)*

The aim of Expt. 1082 is to determine ionization energies of both the $Mu_{BC}$ and $Mu_T$ centres in $Si_{1-x}Ge_x$ bulk alloys as a function of alloy composition $x$. These results would provide a test of theoretical predictions for the energies of thermodynamic defect levels of hydrogen and for the valence band alignments across the full alloy composition range. A simple band-alignment model suggests that the $Mu_{BC}$ ionization energy may have a maximum near the Σ (Si-like) to L (Ge-like) crossover at alloy composition $x = 0.85$, and that the hole ionization energy for $Mu_T$ should decrease linearly with $x$, becoming zero near $x = 0.9$. This experiment has therefore focused on high-Ge content alloys, with several samples being available with alloy compositions from $x = 0.84$ to $x = 0.974$. Samples were in the form of single crystals cut from Czochralski-grown boules, generally [100] in orientation and nominally undoped, but with native defects giving p-type carrier concentrations in the region of $10^{14} - 10^{15}$ cm$^{-3}$. High transverse field measurements were performed using HiTime on M15 to observe the temperature-dependence of neutral state and diamagnetic amplitudes.

Following earlier studies [King *et al.*, J. Phys.: Cond. Matt. **17**, 4567 (2005)] on the alloy dependence of hyperfine parameter for the neutral species performed for $x \leq 0.77$, the present studies confirm the linear variation with $x$ of $Mu_{BC}$ isotropic hyperfine parameter component into the high-Ge alloy region. Figure 1(a) shows a Fourier spectrum in the frequency region of the diamagnetic and $Mu_{BC}$ $\nu_{12}$ and $\nu_{34}$ lines from $Si_{0.103}Ge_{0.897}$ at 5 K. Several samples showed asymmetric $Mu_{BC}$ line amplitudes as observed here. For $Mu_T$, hyperfine parameter values were again observed to be suppressed below those expected for a linear dependence of this parameter with $x$. In some cases $Mu_T$ lines were observed to be split, as shown for $Si_{0.148}Ge_{0.852}$ at 25 K in Fig. 1(b) – the two peaks here correspond to hyperfine parameter values of around 2003 MHz and 2126 MHz (compared with pure Si and Ge values of 2005 MHz and 2360 MHz respectively at this temperature).

Figure 2 shows low-temperature diamagnetic and paramagnetic asymmetries from $Si_{0.103}Ge_{0.897}$. These were produced from time-domain fits to the two $Mu_{BC}$ lines (the $Mu_{BC}$ asymmetry shown is the total for both lines), and a single line fitted to the $Mu_T$ signal (in order to get an estimate of its asymmetry variation – more detailed fits using more than one component to allow for line splitting are in progress). Both $Mu_T$ and $Mu_{BC}$ show similar amplitude temperature dependences below 50 K, and their disappearance at this temperature is marked by the beginning of a rise in the diamagnetic amplitude. Figure 3 shows the diamagnetic signal asymmetry up to room temperature. Above 100 K two components are visible in the diamagnetic signal, one fast-relaxing (relaxation rates of between 1 $\mu s^{-1}$ and 10 $\mu s^{-1}$) the other slow-relaxing (relaxation rates between 0.06 $\mu s^{-1}$ and 0.3 $\mu s^{-1}$). The fast-relaxing component amplitude peaks at around 150 K; full diamagnetic asymmetry is reached above approximately 225 K. A conversion of both paramagnetic species to diamagnetic is clearly happening over this temperature range, most likely due to $Mu_{BC}$ ionization possibly together with a T to BC site change followed by ionization.

In $Si_{0.16}Ge_{0.84}$, the rise in diamagnetic asymmetry occurs around 40 K higher in temperature than in $Si_{0.103}Ge_{0.897}$, but is similarly accompanied by the appearance of a fast-relaxing component – the total diamagnetic asymmetry for $Si_{0.16}Ge_{0.84}$ is shown in Fig. 3 alongside the $Si_{0.103}Ge_{0.897}$ data. In the $Si_{0.16}Ge_{0.84}$ case, the paramagnetic species are both visible to higher temperatures than in $Si_{0.103}Ge_{0.897}$. However, they disappear in the transverse field data at different temperatures, $Mu_T$ being visible to around 70 K and $Mu_{BC}$ to around 130 K. There is a peak in the $Mu_{BC}$ signal amplitude at around 65 K, suggesting that a site change of $Mu_T$ to $Mu_{BC}$ may be occurring here, followed by a $Mu_{BC}$ ionization occurring at a higher temperature than in $Si_{0.103}Ge_{0.897}$.

More detailed data analysis is ongoing to properly map out and quantify the paramagnetic species' behaviour over this high-Ge alloy region.

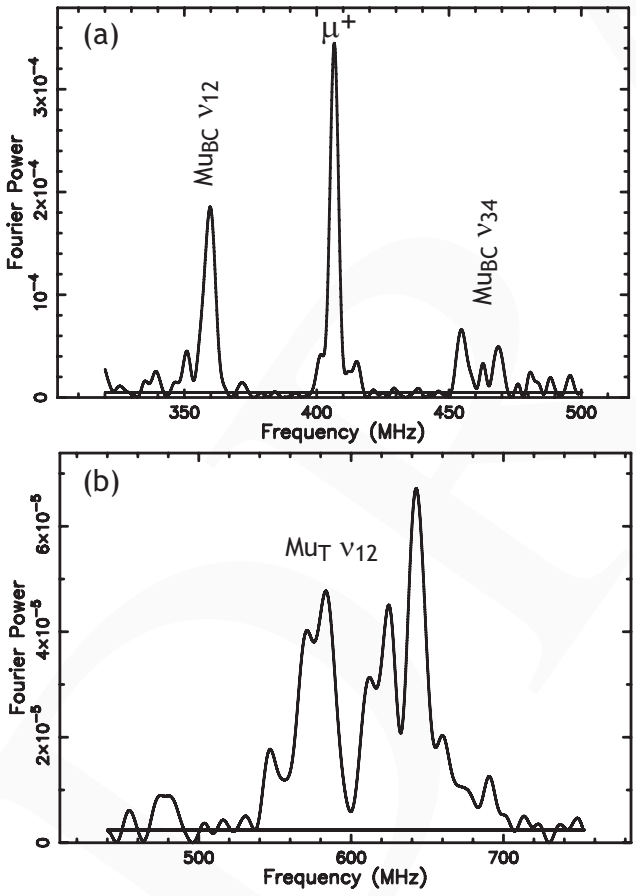


Fig. 1. Fourier plots showing (a) asymmetrical $Mu_{BC}$ lines at 5 K from $Si_{0.103}Ge_{0.897}$, and (b) split $Mu_T$ line from $Si_{0.148}Ge_{0.852}$ at 25 K.

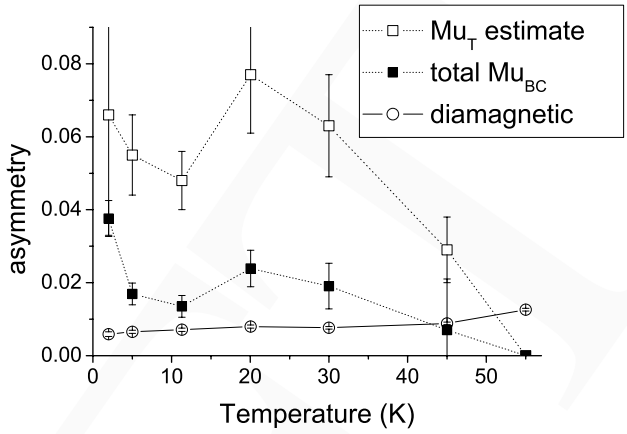


Fig. 2. Low-temperature signal asymmetries for $Si_{0.103}Ge_{0.897}$.

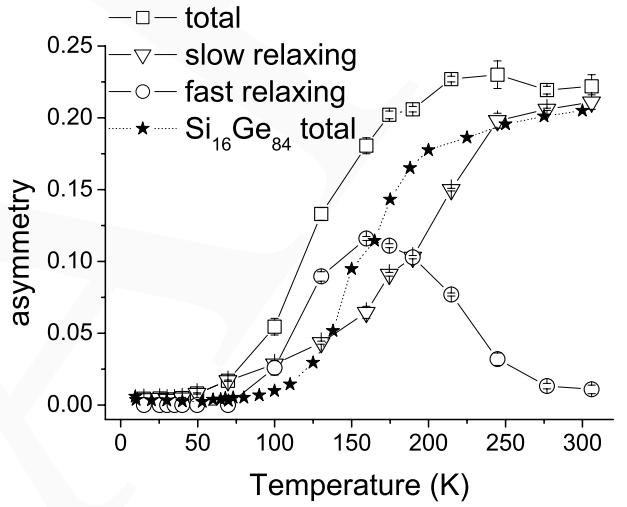


Fig. 3. Temperature dependence of diamagnetic signal components for $Si_{0.103}Ge_{0.897}$ together with the total diamagnetic asymmetry for $Si_{0.16}Ge_{0.84}$.

**Experiment 1083**
**Static and dynamic properties of multipoles in *f*-electron systems**
*(T.U. Ito, JAEA/Tokyo IT; W. Higemoto, R.H. Heffner, JAEA)*

The intermetallic binary alloy $PrPb_3$ crystallizes into the $AuCu_3$-type cubic structure. The crystalline electric field (CEF) ground state of $PrPb_3$ is believed to be a nonmagnetic $\Gamma_3$ doublet which carries quadrupole degrees of freedom. This compound exhibits a second-order phase transition at $T_Q$ (= 0.4 K in zero field) ascribed to antiferroquadrupolar (AFQ) ordering. Recently, the investigation of a field-induced dipole moment by neutron diffraction revealed that the AFQ ordering has remarkable characters [Onimaru *et al.*, Phys. Rev. Lett. **94**, 197201 (2005)]. The arrangement of quadrupole moments in the AFQ phases is not a simple alternating structure, but a periodically modulated

structure. In addition, the AFQ ordering phase on the high temperature side possibly has an incommensurate ordering structure, which seems generally improbable for quadrupolar ordering. The mechanism of such an exotic AFQ ordering is still an open question.

We have performed muon Knight shift measurements on $PrPb_3$ to elucidate the novel AFQ ordering and local electronic states. To the best of our knowledge, no microscopic measurements with a local magnetic probe have been carried out on $PrPb_3$, except for our $\mu$SR. We observed quite anisotropic muon Knight shifts in the temperature range much higher than $T_Q$. It is important to understand the nature of a paraquadrupolar state, ahead of the investigation of the novel AFQ ordering state. Here, we report on muon Knight shift studies of $PrPb_3$ above 2.5 K in the paraquadrupolar state.

A single crystalline sample of $PrPb_3$ was grown by the Bridgman method. The ingot was cleaved into several pieces with [001] cleavage plane and typical dimension $2 \times 2 \times 0.7$ mm$^3$. Transverse field (TF) $\mu$SR measurements were performed from 250 K down to 2.5 K at the M15 beam line. The HiTime spectrometer and a conventional $^4$He flow cryostat were used. The sample pieces were arranged in a rectangular shape with the approximate area of $8 \times 8$ mm$^2$ and the thickness of 0.7 mm. Positive muons were implanted into the sample with the initial spin direction perpendicular to the [001] direction of the crystal. A magnetic field of 2 T was applied along the [001] direction.

Two different muon spin precession frequencies were observed in the time differential TF-$\mu$SR spectrum. One can find two peaks in a typical FFT spectrum at 45 K shown in Fig. 1. The relative intensity of these two signals, 2:1, suggests that implanted muons sit midpoint between nearest-neighbour Pr ions. We hereafter assume this site as the crystallographically exclusive muon site. In such a case, a magnetic field along the [001] direction produces two inequivalent magnetic sites. The precession frequency $f_\perp$ of 2/3 signal corresponds to muon sites between Pr atoms adjoined along [100] and [010] directions while the frequency $f_\parallel$ of the remaining 1/3 signal comes from muons stopping between Pr atoms along the field direction [001].

The muon Knight shift was derived from the observed precession frequencies through $K_{\perp,\parallel} = (f_{\perp,\parallel} - f_0)/f_0 - K_{\mathrm{L,dem}}$, where $f_0$ is a zero-shift reference frequency and $K_{\mathrm{L,dem}}$ is the correction term for the Lorentz and demagnetization fields. An effective demagnetization factor was determined to be 0.572 from the Knight shift of a reference sample with well defined dimension. We show plots of the Knight shift $K$ versus the bulk susceptibility $\chi$ in Fig. 2. A linear scaling with $\chi$ is clearly seen above about 10 K. We obtained the hyperfine coupling constants $A_\perp = -1.08 \pm 0.32$ mT/$\mu_\mathrm{B}$ and $A_\parallel = 0.697 \pm 0.002$ T/$\mu_\mathrm{B}$ from the slope $K/\chi$. Under axial symmetry, the $A_\mathrm{s}$ values are expressed as follows,

$$\begin{aligned} A_\perp &= A^c_\perp - \frac{1}{2} A^{\mathrm{dip}}_{zz} \\ A_\parallel &= A^c_\parallel + A^{\mathrm{dip}}_{zz} \end{aligned}$$

where $A^c_\mathrm{s}$ and $A^{\mathrm{dip}}_{zz}$ designate the contact-coupling constant and the classical dipolar-coupling constant, respectively.

Supposing an isotropic contact hyperfine interaction, $A^c_\perp = A^c_\parallel$, we obtained unacceptably large dipolar-coupling constant $A^{dip}_{zz} = 0.465 \pm 0.002$ T/$\mu_\mathrm{B}$ compared with the result of a simple dipole calculation, 0.243 T/$\mu_\mathrm{B}$. We therefore accept anisotropy for the contact hyperfine interaction. Using the calculated dipolar-coupling constant, we obtain strongly anisotropic contact-coupling constants $A^c_\perp = 0.120 \pm 0.001$ T/$\mu_\mathrm{B}$ and $A^c_\parallel = 0.454 \pm 0.002$ T/$\mu_\mathrm{B}$. This anisotropy may be concerned with nonspherical distribution of the $4f$-electron remarkable below $\sim$46.7 K: excitation energy of the highest CEF level [Gross *et al.*, Z. Phys. **B37**, 123 (1980)]. The upturn in $K_\perp - \chi$ plot above 61 K possibly reflects thermal smearing of the anisotropy. The upturn in the $K - \chi$ plot below 10 K is likely due to the lowest-lying CEF level with excitation $\simeq$19.4 K [Gross *et al., op. cit.*]. The magnitude of $A^c_\mathrm{s}$ is as large as the dipolar-coupling constant $A^{\mathrm{dip}}_{zz}$, suggesting the strong hybridization between $4f$ and conduction electrons. This result is qualitatively consistent with a large electronic specific heat coefficient $\gamma \sim 1.5$ J/mol·K$^2$ [Morie *et al.*, J. Phys. Soc. Jpn. **75**, Suppl. 183 (2006)], and may be related to novel properties of the AFQ ordering state, where the quadrupole Kondo effect was discussed.

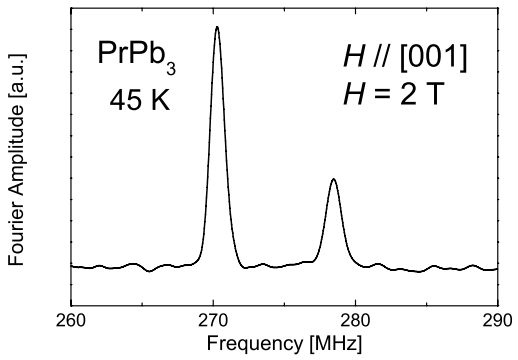


Fig. 1. Typical FFT spectrum at 45 K.

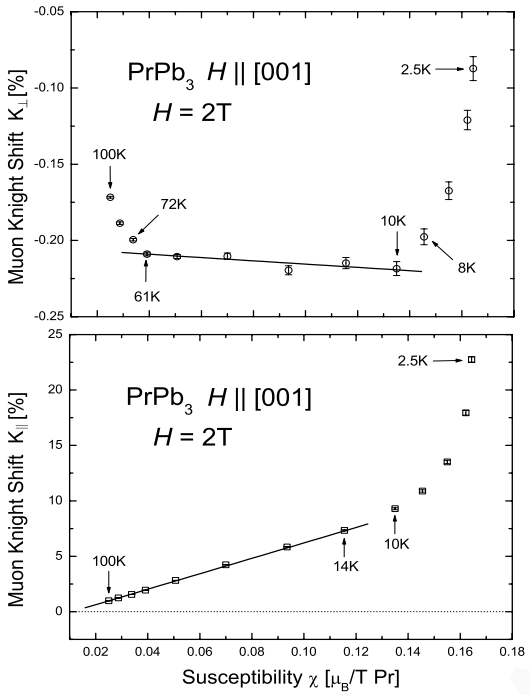


Fig. 2. $K$ versus $\chi$ plot.

**Experiment 1084**
**Searching for hidden magnetic order of the pseudogap state of the 214 cuprates by $\mu$SR and neutron scattering**
*(Y.J. Uemura, Columbia)*

The purpose of Expt. 1084 is to explore the possibility that the pseudogap state in the cuprate superconductors is associated with the spontaneous ordering of orbital currents in the copper-oxide planes. Throughout the years, several variations on this theme have been proposed, but largely dismissed due to the lack of corroborating experimental data. In the past few years, though, a handful of experiments have emerged which support the existence of a particular "circulating current" (CC) state, shown in Fig. 1, at temperatures below pseudogap temperature, $T^*$. In particular, researchers at the Laboratoire Léon Brillouin have published polarized neutron data on $YCa_2Cu_3O_{6+y}$ (123) which they contend are consistent with this CC state [Fauqué *et al.*, Phys. Rev. Lett. **96**, 197001 (2006)]. However, serious debate surrounds both the reproducibility and interpretation of these results, and further experiments are required.

To this end, we have performed a series of ZF-$\mu$SR measurements on various dopings of $La_{2-x}Sr_xCuO_4$ (214) in order to search for the time reversal symmetry breaking (TRSB) fields which would necessarily be associated with local currents in the copper oxide planes. We chose to search for these fields in 214 because several high-quality crystals were readily available and the wide doping range allowed us to examine non-pseudogap samples on the heavily overdoped side of the phase diagram, in addition to underdoped samples. Moreover, evidence for the existence of a CC phase in 214 would be more significant, as it would point towards a more general property of the cuprates rather than those particular to 123.

Zero field spectra were taken with the crystalline $c$-axis aligned parallel to the beam axis and the inital muon polarization direction rotated ∼45°. This geometry allowed us to search for spontaneous local fields parallel and perpendicular to the copper-oxide planes simultaneously, and reduce our experimental runtime. In order to maximize our sensitivity to TRSB fields, we performed our ZF-$\mu$SR measurements using the active-veto, ultra-low background insert for the LAMPF spectrometer on M20. We also used trim coils to adjust the total external field at the sample site to less than 50 mG.

The resultant spectra showed no sign of the precession which one would expect for a unique local field at the muon site. Instead, the spectra in each direction were well-described by a Gaussian function:

$$A(t) = A_0 e^{-\Delta^2 t^2},$$

where $\Delta$ is the relaxation rate and varies with temperature. This is what one expects for a Gaussian distribution of local fields from small, randomly oriented nuclear dipole moments.

The relaxation rates for three 214 crystals, with $x = 0.13$, 0.19 and 0.30, are shown in Fig. 2 as a function of temperature. The two sets of relaxation rates represent the root mean square field perpendicular and parallel to the copper-oxide planes. The rates are roughly temperature independent below 200 K for all three crystals. The decrease in relaxation above 200 K is ascribed to motional narrowing due to muon diffusion, as 200 K is comparable to the diffusion temperature seen in similar materials.

The important observation, however, is that the relaxation rates at a given temperature are roughly identical for all three crystals. This is significant since the pseudogap dominates the 13% sample ($T^* \sim 500$ K) and is non-existent in the 30% sample ($T^* \sim 0$ K). Thus, we are effectively crossing the pseudogap line along the Sr doping axis of the phase diagram. We can use this fact to put an upper limit on any possible currents associated with the pseudogap state, and ultimately compare with other experiments.

For example, the muon site for the 214 systems is known [Hitti *et al.*, Hyp. Int. **63**, 287 (1990)]. If we approximate the triangular current loops in Fig. 1 by

magnetic dipoles of size $n$ Bohr magnetons oriented perpendicular to the copper-oxide plane (as done previously), then the size of the local magnetic field at the muon site due to the 3 nearest current loops is

$$H = 0.135 n \gamma_\mu \,,$$

where $\gamma_\mu/2\pi = 0.135$ MHz/G.

If we say then that the relaxation rates for the different samples are the same within $\sim$0.01 $\mu s^{-1}$, then our data imply $n \leq 0.00012$, which is 2–3 orders of magnitude smaller than the moment reported by neutron scattering in 123. Thus, we have effectively eliminated the possibility that the CC state exists in these materials. This has profound consequences for the generality of the previously mentioned neutron results.

This work is ongoing, with similar measurements planned for other known pseudogap materials such as $La_{2-x}Ba_xCuO_4$ and $Bi_2Sr_2CaCu_2O_{8+\delta}$. The current results are currently being prepared for publication and will also be presented at the March meeting of the American Physics Society in Denver, CO.

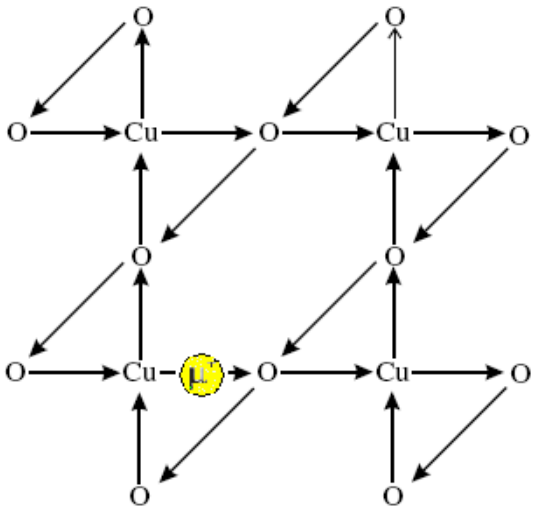


Fig. 1. The circulating current pattern proposed by Varma to explain recent polarized neutron scattering and ARPES data. Figure taken from Simon and Varma, Phys. Rev. Lett. **89**, 247003 (2002). The muon site is 2.1 Å above and below the copper-oxide plane at the position indicated by the yellow circle.

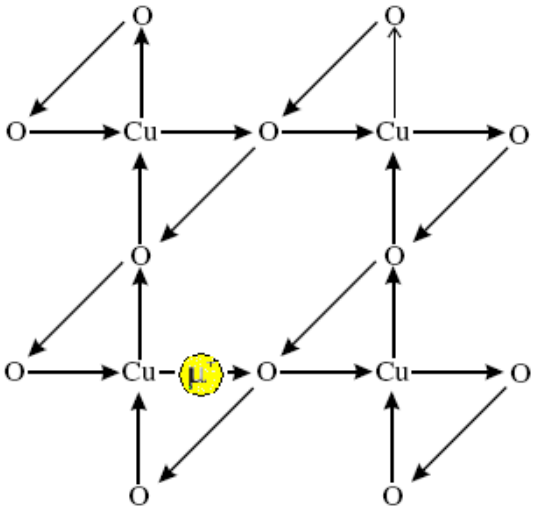


Fig. 2. The relaxation rates as a function of temperature for three 214 samples at dopings across the phase diagram. The upper data represent relaxation of the signal in the in-plane direction, and the lower is relaxation of the signal in the out-of-plane direction.

**Experiment 1085**
**$\mu$SR study of unconventional organic superconductor $\kappa$-(BEDT-TTF)$_4$Hg$_{2.89}$Br$_8$**
*(K. Satoh, Saitama)*

It is now widely accepted that the organic salts, $\kappa$-(BEDT-TTF)$_2X$ ($X$ = anion), can be regarded as band width-controlled superconductors at fixed band filling. In other words, the superconductivity in the $\kappa$-type salt is realized by pressurizing the Mott insulator. Among the $\kappa$-type salts, $\kappa$-(BEDT-TTF)$_4$Hg$_{2.89}$Br$_8$ [Lyubovskaya *et al.*, Pis'ma Zh. Eksp. Teor. Fiz. **46**, 149 (1987)] shows a unique incommensurate structural characteristic not seen in other $\kappa$-type salts. Due to this incommensurability, the electron filling is possibly shifted from the usual half-filled state of 2:1 salts, and therefore the kind of hole-doped state may be realized. $\kappa$-(BEDT-TTF)$_4$Hg$_{2.89}$Br$_8$ shows superconductivity at 4.2 K and the upper critical field of this salt is anomalously larger than the Pauli limit value. Further electrical resistance in the normal state shows linear dependence on temperature at low temperatures, which is characteristics of non-Fermi liquid properties. From these measurements, we consider that unconventional superconductivity is realized in $\kappa$-(BEDT-TTF)$_4$Hg$_{2.89}$Br$_8$. In order to clarify the superconducting properties of $\kappa$-(BEDT-TTF)$_4$Hg$_{2.89}$Br$_8$, we measured ZF-$\mu$SR to investigate whether the superconducting phase at ambient pressure violates the time-reversal symmetry or not. Moreover, we measured the temperature dependence of the muon Knight shift to investigate the microscopic magnetic property of $\kappa$-

(BEDT-TTF)$_4$Hg$_{2.89}$Br$_8$ in the normal state.

Zero field $\mu$SR spectra of $\kappa$-(BEDT-TTF)$_4$Hg$_{2.89}$Br$_8$ are fitted by the product of the temperature-independent Kubo-Toyabe function and the exponential function. Figure 1 shows the temperature dependence of the relaxation rate $\lambda$ of the exponential function. The relaxation rate $\lambda$ increases with decreasing temperature due to the development of the antiferromagnetic correlations at low temperatures. The relaxation rate $\lambda$ becomes almost temperature-independent below 10 K and no anomaly is found at the superconducting transition temperature, 4.2 K. This result suggests that the superconducting phase in $\kappa$-(BEDT-TTF)$_4$Hg$_{2.89}$Br$_8$ does not break the time-reversal symmetry. However, susceptibility of $\kappa$-(BEDT-TTF)$_4$Hg$_{2.89}$Br$_8$ decreases gradually below 4.2 K and the Meissner volume fraction at 2 K is about 10%. In order to clarify the superconducting phase with broken time-reversal symmetry in $\kappa$-(BEDT-TTF)$_4$Hg$_{2.89}$Br$_8$, zero-field $\mu$SR measurement below 2 K is desired.

Figure 2 shows the temperature dependence of the muon Knight shift of $\kappa$-(BEDT-TTF)$_4$Hg$_{2.89}$Br$_8$ at 6 T. The Knight shift obeys Curie-Weiss behaviour down to 2 K. Static magnetic susceptibility, however, shows a peak around 30 K and a sharp decrease at low temperatures. It is interesting to note that $1/T_1T$ measured by $^{13}$C NMR [Miyagawa, unpublished] also shows Curie-Weiss behaviour down to 10 K and does not show a maximum. The origin of the discrepancy between macroscopic measurements and microscopic measurements is not clear at present and further study is needed.

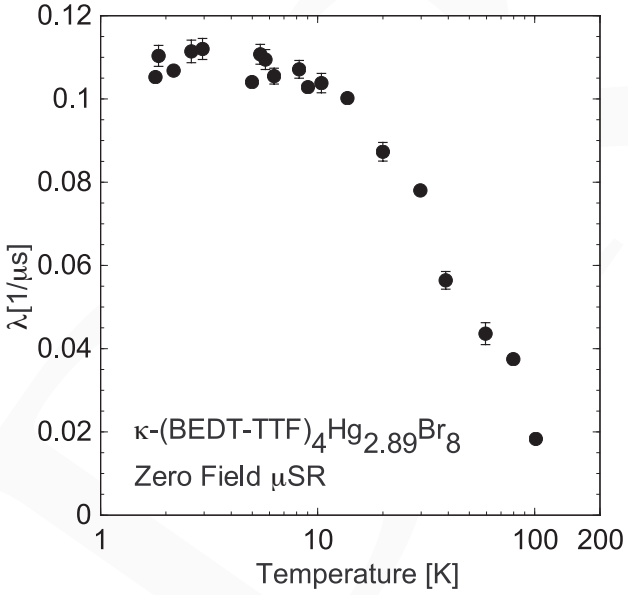


Fig. 1. Temperature dependence of the relaxation rate of $\kappa$-(BEDT-TTF)$_4$Hg$_{2.89}$Br$_8$. No anomaly was found at the superconducting transition temperature.

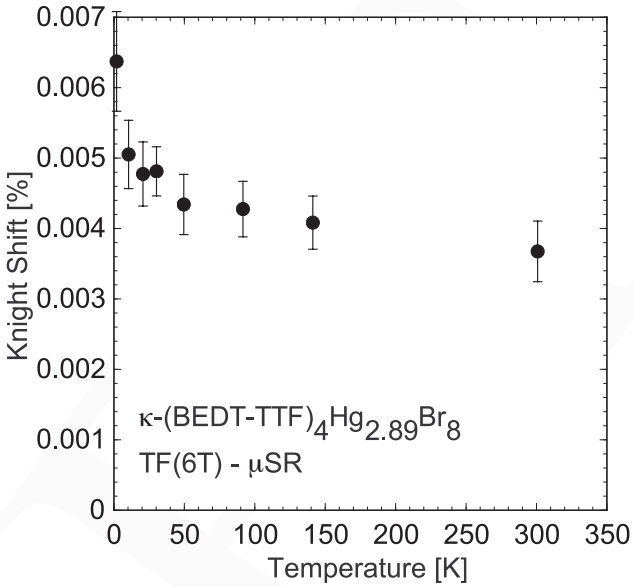


Fig. 2. Temperature dependence of muon Knight shift of $\kappa$-(BEDT-TTF)$_4$Hg$_{2.89}$Br$_8$. Magnetic susceptibility shows a peak around 30 K and the $K-\chi$ plot deviates from the linear relation at low temperatures.

**Experiment 1087**
**Spin freezing in 5% Sr doped La$_2$CuO$_4$**
*(W. Bao, Los Alamos National Lab.)*

The interest in the low doping region of La$_{2-x}$Sr$_x$CuO$_4$ is related to the proximity to antiferromagnetic and superconducting domains. $\mu$SR previously found a spin glass behaviour, not usually accounted for in the neutron scattering dynamic structure factor. Quasi-elastic spin fluctuations with energy scale smaller than the energy resolution of neutron spectrometers have been misinterpreted as static and attributed to long-range antiferromagnetic order.

We performed zero field (ZF) and longitudinal field (LF) measurements in the 5% doped La$_{2-x}$Sr$_x$CuO$_4$, in the same sample that we used in neutron scattering experiments. Weak transverse field runs (Fig. 1) already show the presence of a magnetic component developing somewhere below 250 K.

ZF-$\mu$SR data (Fig. 2) can be described by

$$A(t) = A_{\rm fast}e^{-\lambda_{\rm fast}t} + A\cos(2\pi ft)e^{-\lambda t}$$

where $\lambda$ and $\lambda_{\rm fast}$ are relaxation of the two magnetic signals with amplitudes $A$ and $A_{\rm fast}$. The non-oscillating part is unchanged up to 25 K, and with a very slow variation between 25 and 150 K. We ascribe this to the same magnetic component seen in weak transverse field runs.

The oscillating part, described by a frequency $f$, is proportional to the strength of static magnetic field at

the muon site. There is static magnetism in the sample below 5 K (Fig. 3). Frequency of the oscillating part at lowest temperature is similar to previous results obtained for 214 cuprates at dopings greater than 1–2%. This confirms a similar magnetic environment for muon in the spin glass like regime and spin density wave regime around 1/8 hole doping. Temperature dependence of the frequency of the oscillating signal is typical of a second order phase transition. Relaxation of the signal, proportional to magnetic field inhomogeneity, diverges around transition temperature.

LF-$\mu$SR data shows that both oscillating and non-oscillating components are completely decoupled by magnetic fields around 2 kG, at temperatures around 2 K. This indicates a static origin for both. The slow temperature dependence of the "fast" relaxing signal between 25 and 125 K can be understood if we believe that this is due to a phase with doping concentrations below 2%, but without long range magnetic order.

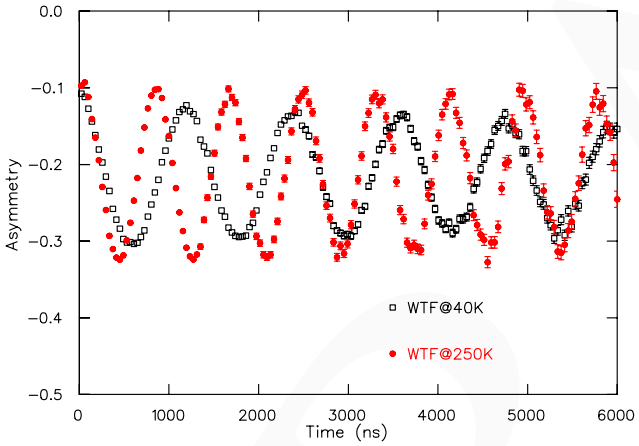


Fig. 1. Weak transverse field at 40 K and 250 K show existence of a high temperature magnetic component.

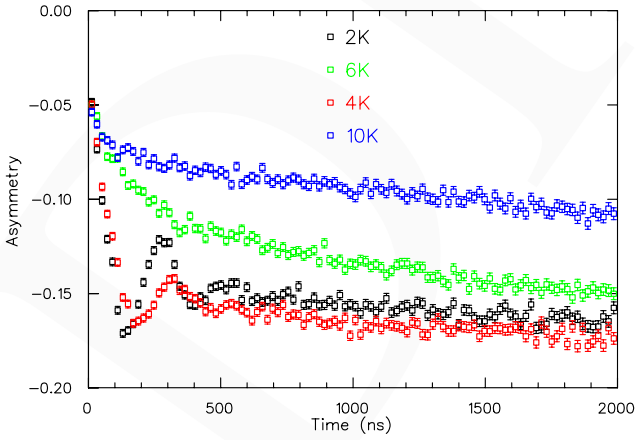


Fig. 2. Zero field $\mu$SR data.

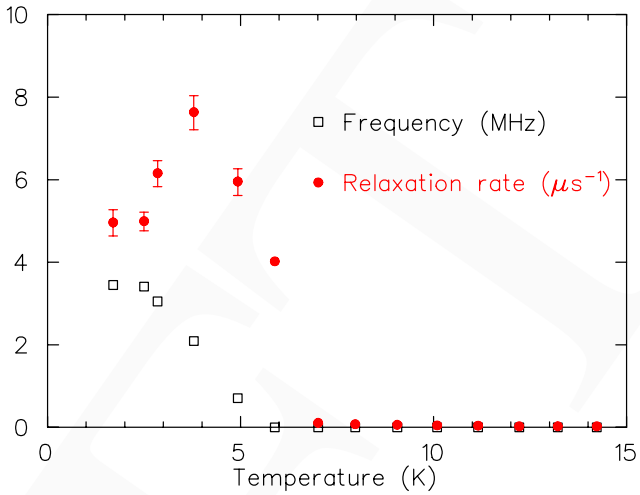


Fig. 3. Zero field $\mu$SR results: frequency and relaxation of the low temperature magnetism component.

**Experiment 1092**
**Electronic ground state of quasi-1D conducting $\beta$-vanadium bronzes**
*(S. Takeshita, R. Kadono, KEK-IMSS)*

As a quasi-one-dimensional (1D) conductor, $\beta$-$Na_{0.33}V_2O_5$ has been attracting much interest because it exhibits various phases separated by successive transitions from metal to insulator ($T_{MI} \sim 135$ K) and then to antiferromagnetic phase ($T_N \sim 24$ K) under ambient pressure, which occur besides Na ion site-ordering ($T_{Na} \sim 244$ K). More interestingly, it falls into a superconducting state below $T_c \sim 8$ K under a pressure of ~8 GPa [Yamauchi *et al.*, Solid State Science **7**, 874 (2005)]. It has been reported that metallic conductivity is observed in the resistivity measurement above $T_{MI}$, whereas density of states at the Fermi level is hardly observed in the ARPES measurement [Okazaki *et al.*, Phys. Rev. **B69**, 140506 (2004)]. While recent neutron diffraction [Nagai *et al.*, J. Phys. Soc. Jpn. **74**, 1297 (2005)] and NMR measurements [Itoh *et al.*, Phys. Rev. **B74**, 054434 (2006)] suggest the occurrence of a complex electronic state such as charge disproportion and/or spin density wave, more information would be required to elucidate the microscopic origin of those phases in more detail. We have performed high transverse field muon spin rotation (HTF-$\mu$SR) measurements on the M15 beam line using the Hi-Time spectrometer, where the direction of the external field ($H_{TF}$) was parallel to the $a^*$-axis (which is perpendicular to both the $b$ and $c$-axis).

Fourier amplitude of the HTF-$\mu$SR spectra under $H_{TF} = 60$ kOe collected over the paramagnetic region is shown in Fig. 1. The main signal component (C1) observed at 300 K splits into two components, C1 and C2, below $T_{Na}$. Below ~50 K, an additional component (C3) appears between C1 and C2. Therefore, we ana-

lyzed the obtained time spectra by using the following equation:

$$\begin{aligned} A(t) &= \sum_{i=1}^{m} A_i \exp(-\lambda_i t)\cos(\omega_i t + \delta), \\ m &= 1\ (T_{\rm Na} < T), \\ m &= 2\ (50\ {\rm K} < T < T_{\rm Na}), \\ m &= 3\ (30\ {\rm K} < T < 50\ {\rm K}), \end{aligned}$$

where $A_2$ is fixed to the average of values near $T_{\rm MI}$ because it hardly exhibits temperature dependence. Fractional yields of C2 and C3 (estimated from the ratio of $A_i$) are approximately 10% and 20%, respectively. The muon Knight shift is obtained as

$$K_i = \frac{\omega_i/\gamma_\mu - H_{\rm ext}}{H_{\rm ext}} - \left(\frac{4\pi}{3} - N\right)\chi,$$

where $\chi$ is the uniform susceptibility, and we adopted the demagnetization factor $N \sim 4\pi$, considering that the direction of $H_{\rm TF}$ is perpendicular to the sample plate.

The obtained muon Knight shift is plotted as a function of susceptibility in Fig. 2, where $K_i$ corresponds to that of the respective component C$i$. The C2 signal emerges below $T_{\rm Na}$, which is tentatively attributed to the Na site-ordering and associated differentiation of vanadium ions. The origin of the C3 signal is not clear at this stage due to the lack of detailed information, including its temperature dependence.

As shown in Fig. 3, the relaxation rate of the C2 signal ($\lambda_2$) exhibits a remarkable increase below $T_{\rm MI}$, which may be attributed to the broadening of local field distribution (i.e., hyperfine coupling constant). Considering that the muon hyperfine coupling constant is predominantly determined by magnetic dipolar interaction, the muon hyperfine coupling constant in the paramagnetic phase is expressed as follows:

$$A^\mu = \sum_i A_i^{\alpha,\beta} = \sum_i \frac{1}{r_i^3}\left(\delta_{\alpha,\beta} - \frac{3r_i^\alpha r_i^\beta}{r_i^2}\right),$$

where $r_i$ is the distance of the $i$-th V ion from muon. Upon the charge disproportion, the contribution of the nearby V ions to $A^\mu$ would vary from site to site according to the variation of local V states.

The hyperfine coupling constants estimated from the $K$-$\chi$ plot are summarized in the Table I, where $A_i^\mu$ corresponds to that of the respective C$i$ signal. It is clear that $A_1^\mu$ changes at $T = T_{\rm Na}$. This is understood by considering a slight shift of the muon position due to the change in the static electronic potential exerted by the nearby Na ions. Besides this, there is a possibility that the Na site-ordering leads to the change in the electronic state of V ions. Near $T_{\rm MI}$, no discernible change is observed for $A_1^\mu$, while $A_2^\mu$ does exhibit a slight change. The above difference between $A_1^\mu$ and $A_2^\mu$ has a good correspondence with that in the temperature dependence of $\lambda_i$, and thus it coherently indicates that the C2 signal probes a change in the electronic state of V ions associated with the MI transition.

In order to clarify the electronic states below $T_{\rm N}$ and behaviour of the C3 signal, we are planning to perform HTF-$\mu$SR measurements below $T_{\rm MI}$ in more detail. Additional HTF-$\mu$SR measurements for the sample with Na substituted by Ag ($\beta$-$Ag_{0.33}V_2O_5$) are also planned to investigate the universality of the present result among $\beta$-vanadium bronzes.

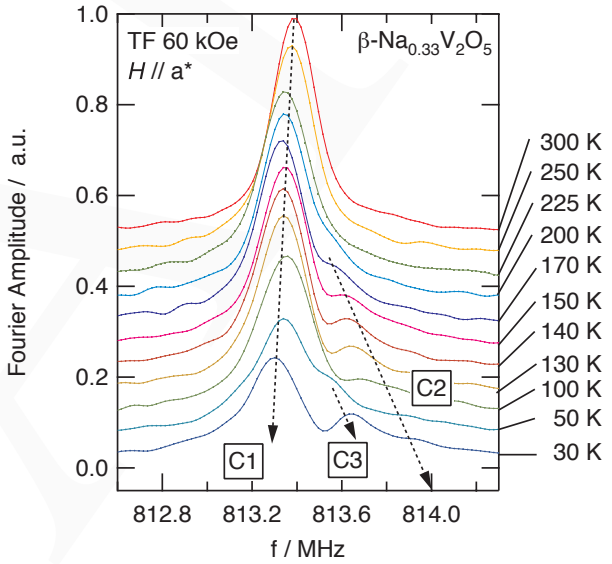


Fig. 1. Fast Fourier transform of TF-spectra under $H_{\rm TF}$ = 60 kOe in $\beta$-$Na_{0.33}V_2O_5$.

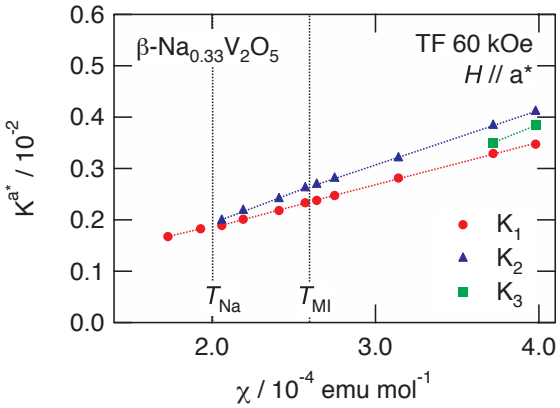


Fig. 2. $K$-$\chi$ plot for $\beta$-$Na_{0.33}V_2O_5$.

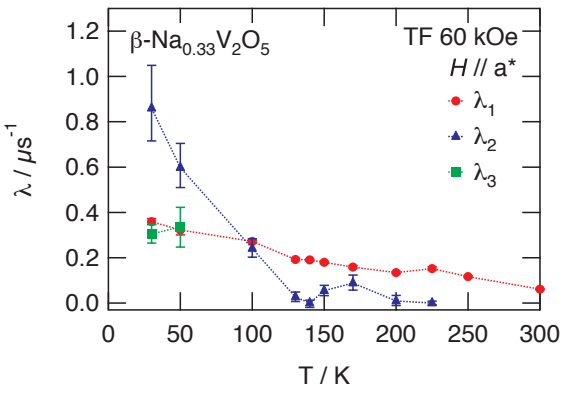


Fig. 3. Temperature dependence of the muon spin relaxation rate.

Table I. Hyperfine coupling constant in kG/$\mu_B$.

| | $T < T_{MI}$ | $T_{MI} < T < T_{Na}$ | $T_{Na} < T$ |
|---|---|---|---|
| $A_1^\mu$ | $46.0 \pm 0.8$ | $47.7 \pm 1.4$ | $\sim 41.4$ |
| $A_2^\mu$ | $59.3 \pm 0.3$ | $67.2 \pm 3.0$ | — |
| $A_3^\mu$ | $\sim 72.0$ | — | — |

**Experiment 1093**
**$\beta$-NMR investigation of magnetic multilayers**
*(Z. Salman, Oxford; R.F. Kiefl CIAR/UBC)*

Structures consisting of layers of ferromagnetic metal separated by spacer layers of a nonmagnetic metal have interesting and useful properties, particularly in regard to spintronic devices. For example, the coupling between the ferromagnetic layers oscillates between ferromagnetic (FM) and antiferromagnetic (AF) as a function of the thickness of the nonmagnetic spacer. This in turn leads to a giant magnetoresistance (GMR) effect whereby the resistance is a strong function of magnetic field. The dramatic increase in hard disk bit density over the last 20 years was made possible by the vast increase in sensitivity of read heads that incorporate GMR structures. Several theoretical models have been proposed to explain this behaviour but the models are difficult to test since few experimental methods are capable of directly probing the induced magentism in the non-magnetic layer.

In this experiment we are using depth resolved $\beta$-NMR to investigate the induced hyperfine fields in Ag/Fe magnetic multilayers. Recently we have taken data on the simplest structure of this type consisting of a layer of Fe (140 Å) followed by a layer of Ag (200 Å) grown expitaxially on a GaAs (001) single crystal substrate. There was also a protective cap of 40 Å of Au on top. Representative $\beta$-NMR spectra at room temperature and 3 different implantation energies are shown in Fig. 1. At full implantation energy (see Fig. 1a) most of the $^8$Li ends up in the GaAs substrate. The observed resonance fits well to a Lorentzian lineshape. The linewidth (4 kHz) is close to that observed in GaAs and is attributed to small nuclear dipolar fields from the Ga and As nuclei. Figures 1b and 1c show the spectra obtained with implantation energies 4.0 and 3.5 keV respectively. At these energies TRIM.SP Monte Carlo simulations predict about 50% of the Li stops in the Ag layer and about 5% in the Au capping layer. The remaining Li ends up in the Fe or is backscattering and does not contribute to the observed signal. The solid curves are fits to a model field distribution based on the RKKY model of hyperfine field oscillations in the Ag from the Fe. Note also there is a sharp peak near zero which is attributed to a small signal from the Au capping layer. The main result is that the induced fields in the Ag decrease away from the Ag/Fe interface according to an asymptotic power law $x^{-1.93(8)}$ in very good agreement with theoretical calculations based on RKKY theory. Also we find that the induced field at the Ag/Fe interface ($B_0 = 0.23(5)$ T) is in resaonable agreement with calculations for Li in Fe.

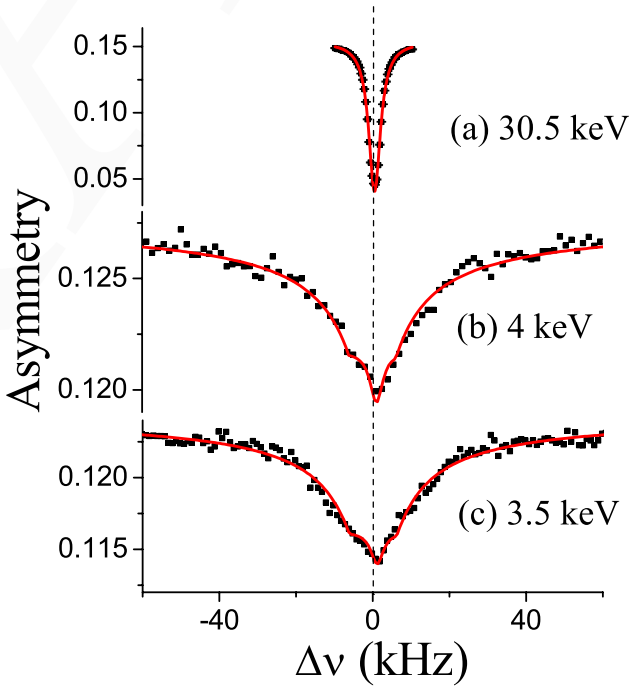


Fig. 1. $\beta$-NMR spectra measured at room temperature in the MML sample at an implantation energy (a) 30.5 keV, (b) 4 keV and (c) 3.5 keV. The solid red lines are best fit to the calculated lineshapes. All spectra frequencies are shown relative to the resonance frequency in the GaAs substrate measured at 4.1 T.

**Experiment 1094**
**$\beta$-NQR study of the phase transition in $SrTiO_3$ and related compounds**
*(M. Smadella, R.F. Kiefl, W.A. MacFarlane, UBC)*

All phase transitions in condensed matter (except Bose-Einstein condensation) arise because of interactions between the basic constituents of the system in question, e.g. spins, ions, electrons, etc. Near any surface or interface the symmetry of those interactions is broken and thus, in general, the phase transition (order parameter, transition temperature, etc.) must be altered to some extent. Unfortunately few experimental methods are able to probe local properties in a depth resolved manner. Recently we have developed the technique of depth resolved $\beta$-detected NMR and NQR for investigating local electronic, magnetic and structural properties on a nanometre scale.

In this experiment we investigate the surface effect on a well known phase transition in the ionic insulator strontium titanate, $SrTiO_3$ (STO). STO has a number of interesting and useful properties, and is perhaps best known for its use as a substrate for growing thin films. There is a second order structural phase transition at 105 K in the bulk; the high temperature phase is cubic whereas the low temperature phase is characterized by a small tetragonal distortion. The phase transition has been the subject of intense experimental investigation, and its bulk properties are well understood. However, much less is known about the behaviour close to a free surface or interface. Optical SHG has demonstrated that an enhancement of the transition temperature is present at the surface, with a change in the surface lattice geometry observed at approximately 150 K, but it is not clear how this temperature enhancement varies as a function of depth.

We have demonstrated that zero field spin relaxation and $\beta$-NQR of $^8$Li can be used as a probe of this near surface transition behaviour. The quadrupole moment of the $^8$Li nucleus couples to electric field gradients within the crystal lattice, and since these gradients are sensitive to the lattice geometry this makes the implanted $^8$Li a sensitive probe of the phase transition. Specifically, the $^8$Li occupies three equivalent sites in the cubic phase and, in the tetragonal phase, two of these sites are oriented such that field gradients cause fast precession of the $^8$Li nuclear spin. The signal from lithium stopping in either of these sites is therefore averaged to zero in the tetragonal phase, resulting in a decrease of the initial $\beta$-decay asymmetry to 1/3 of its value above the transition. The time dependence of the asymmetry at several temperatures is shown in Fig. 1, demonstrating a clear decrease in the initial asymmetry with decreasing temperature. This initial asymmetry is shown as a function of temperature in Fig. 2. As expected, the asymmetry is decreased to 1/3 of its high temperature value below the phase transition. It is also clear that the loss of asymmetry begins around 150 K, indicating that the tetragonal axis lattice constant begins to increase in some lattice sites at this temperature.

The $^8$Li nuclei are implanted into the sample by directing the particle beam on to the sample surface. As a result, there is a distribution of penetration depths of the $^8$Li into the sample. The data shown in Figs. 1 and 2 were taken using a 28 keV $^8$Li beam, and the stopping distribution for such a beam is shown in the inset of Fig. 2. Nearly all the $^8$Li occupy lattice sites within 400 nm of the sample surface, with a large fraction stopping within the first 200 nm. Thus the $^8$Li are sensitive to surface effects.

In conclusion, we have demonstrated that the small quadrupole moment of $^8$Li can be used as a sensitive probe of the local crystal symmetry. We have also confirmed that the structural phase transition near the surface of STO is shifted higher by about 50 K compared to the bulk. This establishes $\beta$-NMR and $\beta$-NQR developed here at TRIUMF as powerful tools to probe phase transitions near a surface. We suspect many other phase transitions will also be altered near a surface or interface, and we intend to continue this study both on STO and related materials. Additionally, the upcoming completion of the beam deceleration platform on the $\beta$-NQR spectrometer will provide us with the ability to vary the beam implantation energy, thus allowing us to study these transitions as a function of depth.

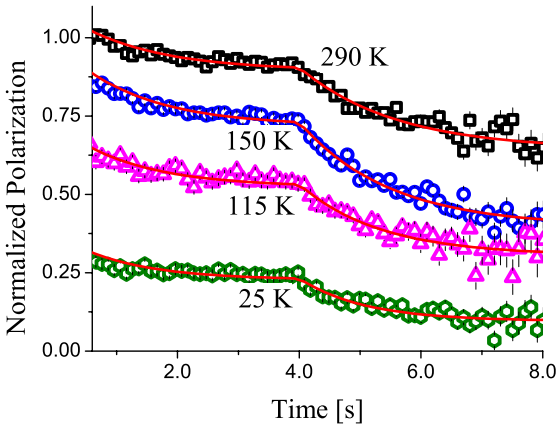


Fig. 1. Time dependence of the asymmetry at several temperatures. The solid lines are fits to a double exponential relaxation function.

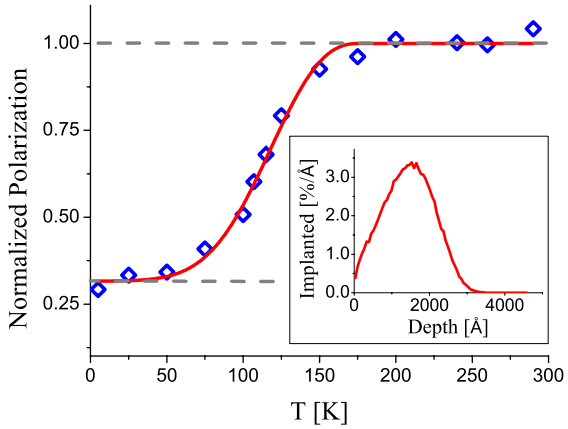


Fig. 2. Temperature dependence of the initial asymmetry. The solid line is a guide to the eye. The inset is the implantation profile of the 28 keV $^8$Li beam.

**Experiment 1095**
**Measurement of the London penetration depth in $NbSe_2$ using low energy polarized $^8$Li**
*(M. Hossain, R. Kiefl, UBC/TRIUMF)*

A fundamental property of any superconductor is the Meissner effect, whereby an external magnetic field is expelled below $T_c$. This is only strictly true deep inside the sample since, close to the surface, the London model predicts an exponential decay of the magnetic field where the decay length is called the London penetration depth ($\lambda_L$). Along with the coherence length ($\xi$), $\lambda_L$ is one of the two fundamental length scales in any superconductor. The absolute value of $\lambda_L$ along with its behaviour as a function of temperature and magnetic field is a sensitive probe of the superconducting state; i.e. the nature of the electron pairing and the elementary excitations from the condensate. Few experimental methods are capable of determining a precise value for $\lambda_L$. For example, in most superconductors, there are a wide range of published values. The reason for this is that most methods are fraught with systematic errors. Only $\mu$SR can be applied to a wide range of materials but conventional $\mu$SR can only be applied to the vortex state.

In this experiment, we are using the technique of low energy $\beta$ detected NMR to investigate the Meissner state of superconductors and in particular, to measure the absolute value of the $\lambda_L$. The beam energy is used to control the mean depth of implantation into the sample, which is on the same length scale as $\lambda_L$. Both the spin relaxation rate and the resonance spectrum depend on the local magnetic field and thus are sensitive to $\lambda_L$. However, the spin relaxation rate is much easier to measure, so we use this to monitor the local magnetic field near the surface. The technique should be applicable to most superconductors but as a first example we have chosen $NbSe_2$.

The $^8$Li nuclear spin relaxation rate $1/T_1$ in $NbSe_2$ was investigated as a function of magnetic field above and below the superconducting transition at $T_c$ = 7.0 K. In low field, $1/T_1$ is determined primarily by low frequency fluctuations of the host Nb nuclear spins, which are characterized by an exponential correlation time $\tau_c$. Typical raw data in the normal state at 8 K are shown in Fig. 1. The data are taken by delivering a long (4 s) pulse of $^8$Li and measuring the beta decay asymmetry (which is proportional to the polarization) as a function of time during and after the pulse. The fitting function is generated by convoluting the spin relaxation function with a square pulse shape. This complicates the fitting function but one obtains much higher statistics than with a conventional short pulse. The field dependence of the spin relaxation rate is shown in Fig. 2 and fits well to a Lorentzian as expected for an exponential correlation time. Given this, one expects the relaxation rate to increase below $T_c$ due to the Meissner effect. This is confirmed by the measured temperature dependence of $1/T_1$ (open diamonds in Fig. 3). In particular note the sharp upturn in $1/T_1$ below $T_c$. There is also a slight temperature dependence to $1/T_1$ above $T_c$ which is attributed to Korringa relaxation of the host nuclear spins (i.e. spin-flip scattering of electrons at the Fermi surface off the nuclear spins). We have shown previously that the direct Korringa relaxation of the $^8$Li is negligibly small at this temperature. The temperature dependence of $\tau_c$ was determined separately from measurements in the vortex state (see solid circles in Fig. 3). These measurements were taken in a much higher magnetic field applied perpendicular to the surface where the sample is in the vortex state and then scaled up to align with the normal state data at 8 K. Recall the average field is almost independent of temperature in the vortex state, so the observed T dependence of $1/T_1$ is attributed solely to changes in $\tau_c$. Note the small bump below $T_c$ for $1/T_1$ in the vortex state which we attribute to the Hebel-Slichter peak in the niobium $\frac{1}{T_1}$.

Finally, using a calculated implantation profile, assuming an exponential field distribution, and taking into account the temperature dependence of $\tau_c$, one can extract the absolute value of the London penetration depth in the Meissner state. The temperature dependence of $\lambda_L$ is shown in Fig. 4. These results confirm low energy $\beta$-NMR can be used to measure the absolute value of $\lambda_L$ in a superconductor. In addition, the experiment has shown that the spin relaxation rate of the $^8$Li in low fields is a sensitive monitor of the host nuclear spin dynamics which is also of interest in studies of superconductivity.

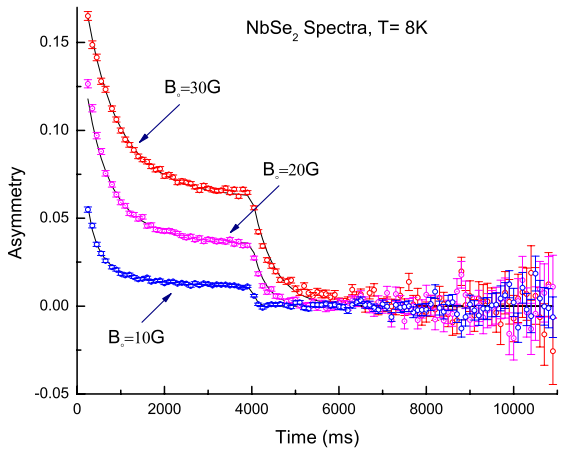


Fig. 1. Time differential spectra at various magnetic fields in the normal state of $NbSe_2$ at 8 K. The data were taken using a 4 s long pulse method.

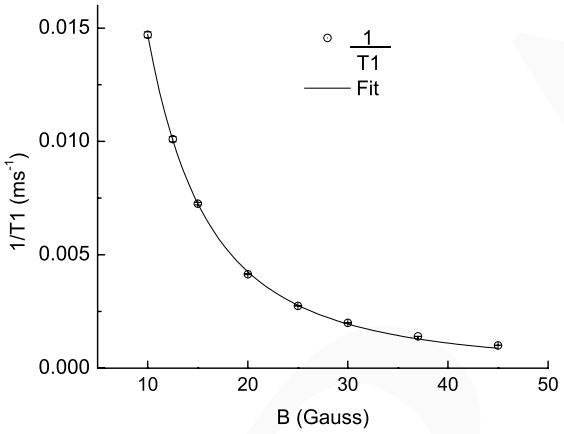


Fig. 2. Magnetic field dependence of the $^8$Li spin relaxation rate in the normal state of $NbSe_2$ at 8 K. The curve is a fit to a simple Lorentzian function.

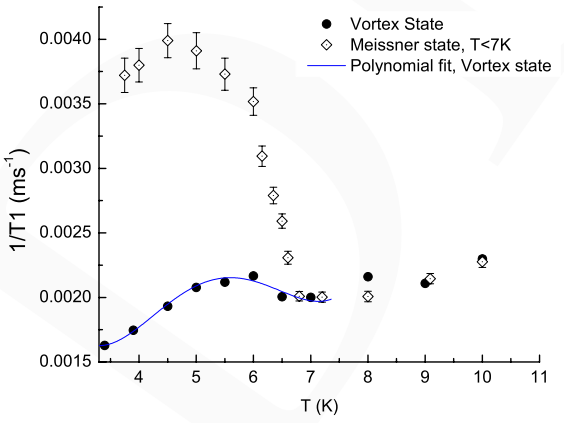


Fig. 3. Temperature dependence of the spin relaxation rate of $^8$Li in $NbSe_2$. The open diamonds are from data taken with the magnetic field of 30 G applied parallel to the surface so the sample remains in the Meissner state. The filled circles are derived from measurements in the vortex state where the magnetic field is applied perpendicular to the surface.

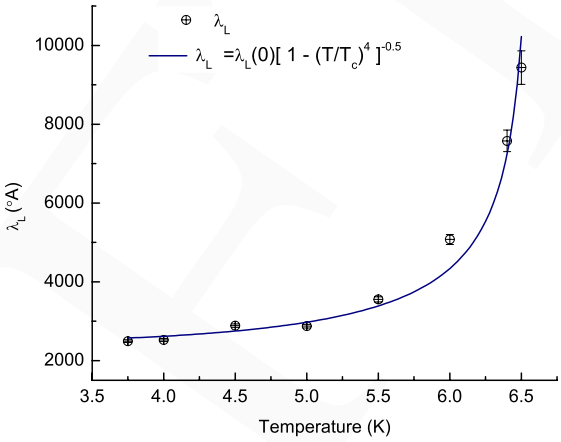


Fig. 4. London penetration depth as a function of temperature.

**Experiment 1099**

**Muonium and muoniated radicals formed in deep eutectic solvents**

*(B.M. McCollum, P.W. Percival, SFU)*

The term deep eutectic (DE) solvent refers to a mixture of a molecular compound with an ionic species such that the melting point of the mixture is much lower than that of either of the individual components. DE solvents are closely related to ionic liquids, which have gained much attention recently as "green" solvents, due to their favorable properties of low volatility, non-flammability, etc. There is very little published data on free radical chemistry in ionic liquids, and none on DE solvents. TRIUMF Expt. 1051 uses muonium to explore the former; this experiment, 1099, is concerned with the latter.

Our exploration of DE solvents in Expt. 1099 was motivated by two aspects of Expt. 945. On the one hand, some of the radicals we have characterized are structurally related to imidazolium salts, which comprise a major class of ionic liquids and whose chemistry has been studied by one of our collaborators, Dr. Jason Clyburne, Canada Research Chair in Environmental Studies and Materials at Saint Mary's University, Halifax. On the other hand, we are seeking a novel solvent for our mechanistic study of the azulene to naphthalene conversion reaction. The transverse-field $\mu$SR spectrum shows up to six radicals, but to identify them we need to analyze the very complex muon LCR spectrum (each radical has as many as eight inequivalent

protons, each giving rise to a unique resonance). The difficulty is compounded by the relatively weak signals. The principal problem is that only about 30% of thermalized muons form muonium (and hence muoniated radicals) in the commonly used hydrocarbon solvents. It is hoped that a suitable non-reactive DE solvent can be found that generates a higher muonium fraction and hence more intense radical signals.

To date we have been successful in detecting muonium signals in a neat DE solvent, and radical signals in a different DE solvent as well as in an inert DE solvent containing a radical precursor as solute. The muonium signal decayed rather quickly (exponential time constant <0.5 $\mu$s), and until further experiments are performed it is not possible to say if this is due to chemical reaction with the components of the solvent mixture (choline chloride and urea), reaction with an impurity, or spin relaxation (perhaps accentuated by the high viscosity). Nevertheless, detection of muonium was sufficient grounds to proceed with experiments to detect muoniated radicals. This requires high magnetic fields (3–30 kG), and the apparatus used is not compatible with the low fields (5–10 G) used for muonium detection.

Muoniated radicals have been detected in DE solvents by both TF-$\mu$SR and LCR under two different scenarios. In the first, muonium reacted directly with one component (hydroquinone) of the DE mixture. This is evident from the pair of radical precession frequencies shown in the upper spectrum of Fig. 1. The muon hyperfine constant (450 MHz) is typical for a dihydroxycyclohexadienyl radical. In the second example hydroquinone was dissolved in an unreactive DE solvent. The same muoniated radical product is formed, as evident from the characteristic CHMu resonance seen in the LCR spectrum shown in the lower part of Fig. 1.

Although these results do not show any enhanced muonium fractions, they establish the feasibility of using DE solvents in muonium chemistry studies. Future research directions include a systematic study of muonium decay kinetics and specific radical investigations, such as the azulene problem mentioned above.

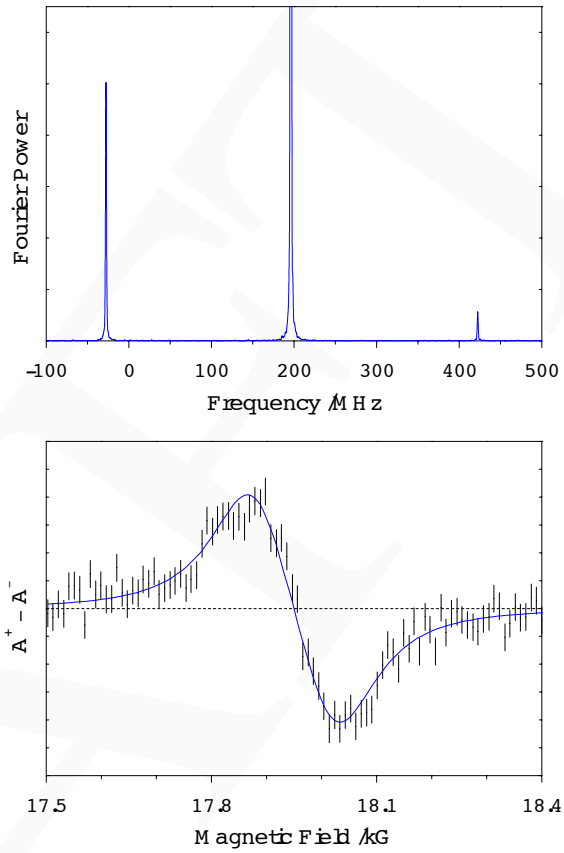


Fig. 1. $\mu$SR spectra obtained from hydroquinone in a deep eutectic solvent. Upper: Fourier power TF-$\mu$SR spectrum showing a pair of radical precession signals at –27.5 MHz and +422.5 MHz. Lower: Muon LCR spectrum showing the resonance due to the CHMu group of a muoniated cyclohexadienyl radical.

**Experiment 1100/1041**
**Nature of the quantum critical transition in electron-doped superconducting films of $Pr_{2-x}Ce_xCuO_4$**
*(H. Saadaoui, R. Kiefl, W.A. MacFarlane, UBC)*

One of the key questions about the phase diagram of high-$T_c$ cuprate superconductors vs. charge-doping is the occurrence and nature of quantum critical points, i.e. phase transitions at zero temperature, which are thought to control the electronic properties of the material over a wide range of temperature and doping, and may hold the key to the origin of the unconventional superconductivity. In Expt. 1100, we are studying the electron-doped family of cuprates ($Pr_{2-x}Ce_xCuO_4$), which can be prepared as high quality thin films, but not readily as macroscopic crystals. For comparison, we have also studied the canonical hole-doped cuprate $YBa_2Cu_3O_7$. This also provides an important control measurement for Expt. 1041 which will be run

when the deceleration capability is completed on the $\beta$-NQR spectrometer. In our preliminary experiments on $Pr_{2-x}Ce_xCuO_4$ and $YBa_2Cu_3O_{7-\delta}$, we measured the magnetic field distribution in the vortex state near optimal dopings.

**Optimally doped $Pr_{2-x}Ce_xCuO_4$**

Our measurements were taken on a $c$-axis oriented $Pr_{2-x}Ce_xCuO_4$ (PCCO) film ($x = 0.15$ and $T_c \sim 20$ K) of 300 nm thickness, epitaxially grown by pulsed-laser deposition on a $SrTiO_3$ substrate. We carried out the experiment on the high-field $\beta$-NMR platform, where a beam of $^8Li^+$ with kinetic energies ranging from $E = 30$ to 1 keV was implanted into a thin overlayer of Ag (40 nm thick) evaporated onto the PCCO. By stopping in the Ag layer, we measure a field distribution due to the emergence of the magnetic field lines from the vortex lattice of the superconducting layer. The measurements were carried out in the vortex state by applying magnetic fields $B > B_{c1}$. Measurements of the temperature dependence of the $\beta$-NMR resonance showed a dramatic broadening in the vortex state (below $T_c$) as shown in Fig. 1a. The FWHM vs. temperature displayed in Fig. 1b is temperature independent above the transition where the broadening is due to Ag nuclear dipolar fields. The broadening increases dramatically below $T_c$, indicating a larger magnetic field inhomogeneity due to the formation of flux vortices. However, the lineshape is symmetric or even has a negative skewness, which is inconsistent with the positive skewness expected for a regular triangular or square vortex lattice.

A disordered lattice may lead to a symmetric or negatively skewed field distribution [Divakar *et al.*, Phys. Rev. Lett. **92**, 237004 (2004)]. On the other hand, it is also possible that the vortex lattice is molten near the surface [De Col *et al.*, Phys. Rev. Lett. **96**, 177001 (2006)]. The extent of superconductivity in the phase diagram is relatively well-established. The symmetry of the superconducting ground state is more elusive, but also established in many systems. However, it has proven very difficult to follow the evolution of magnetism with doping. To determine whether $Pr_{2-x}Ce_xCuO_4$ at this doping is magnetic, we measured the resonance in the normal state at $T = 30$ K and superconducting state at $T = 5$ K, at different applied fields. The FWHM of the field distributions as a function of applied field is plotted in Fig. 1c. The additional field dependent broadening apparent above $T_c$ indicates another nonsuperconducting source of magnetic inhomogeneity, such as might be expected from some form of magnetic freezing in the PCCO. The FWHM at 4.1 T plotted in the inset of Fig. 1b against temperature clearly shows the existence of such magnetic broadening in the normal state.

Measurements of the field distribution for other dopings and other applied fields are planned in order to follow the evolution of magnetism and superconductivity, seeking evidence of a quantum phase transition. More samples of different dopings ranging from underdoped to overdoped will be studied next.

**Optimally doped $Ba_2Cu_3O_{7-\delta}$**

Our measurements on PCCO proved to be unusual as the asymmetry of the field distribution does not show the known features of a regular vortex lattice. For completeness, we needed to confirm these results by performing control experiments on the well-studied $Ba_2Cu_3O_{7-\delta}$ (YBCO). For this purpose, we have measured the field distribution in a 120 nm Ag overlayer on an optimally doped YBCO crystal ($\sim$1 mm thick, $T_c = 89$ K). Such systems have been studied by low-energy $\mu$SR and revealed the emergence of a regular vortex lattice in the superconducting state [Niedermayer *et al.*, Phys. Rev. Lett. **83**, 3932 (1999)]. Here, we measured the resonance by stopping the $^8Li^+$ in the Ag in an applied field of 516 G. We find an asymmetric lineshape (see Fig. 2a) with a noticeable positive skewness as expected. The FWHM in Fig. 2b broadens with $T$ smaller than $T_c$ because of the inhomogeneity of internal fields in YBCO. The FWHM should decrease at higher applied fields as the vortices are packed more tightly (with spacing decreasing as $1/\sqrt{B}$). However, the substantial broadening at high applied fields is inconsistent with this, suggesting that existing models for the field distribution in a normal metal overlayer need to be modified to include the superconductor/metal interface effects.

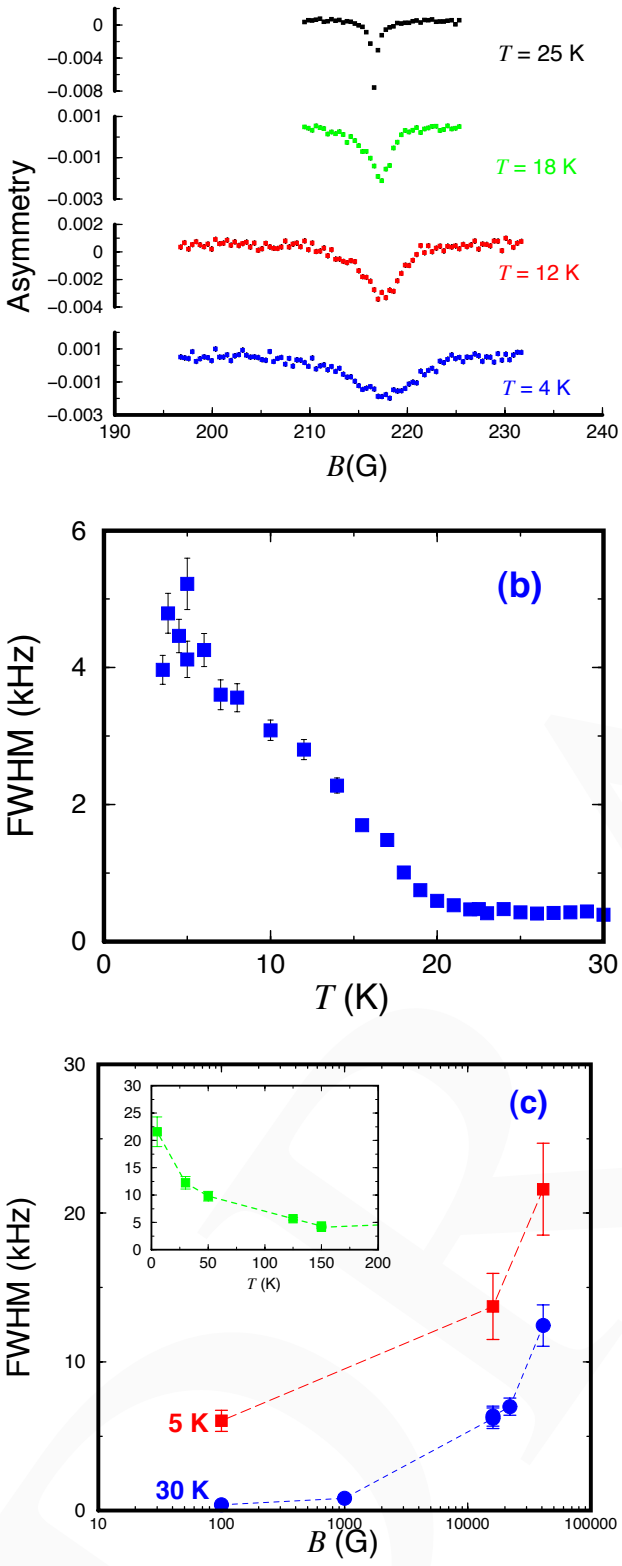


Fig. 1. (a) The $\beta$-NMR resonance of the PCCO vortex state measured in a longitudinal applied field of 216 G. Inset: the profile of $^8Li^+$ beam of 5 keV energy stopping into Ag simulated using TRIM code. (b) The FWHM of Lorentzian fits of the resonance. (c) FWHM vs. $B$ at temperatures 30 K and 5 K. Inset: FWHM vs. $T$ in an external field of 4.1 T.

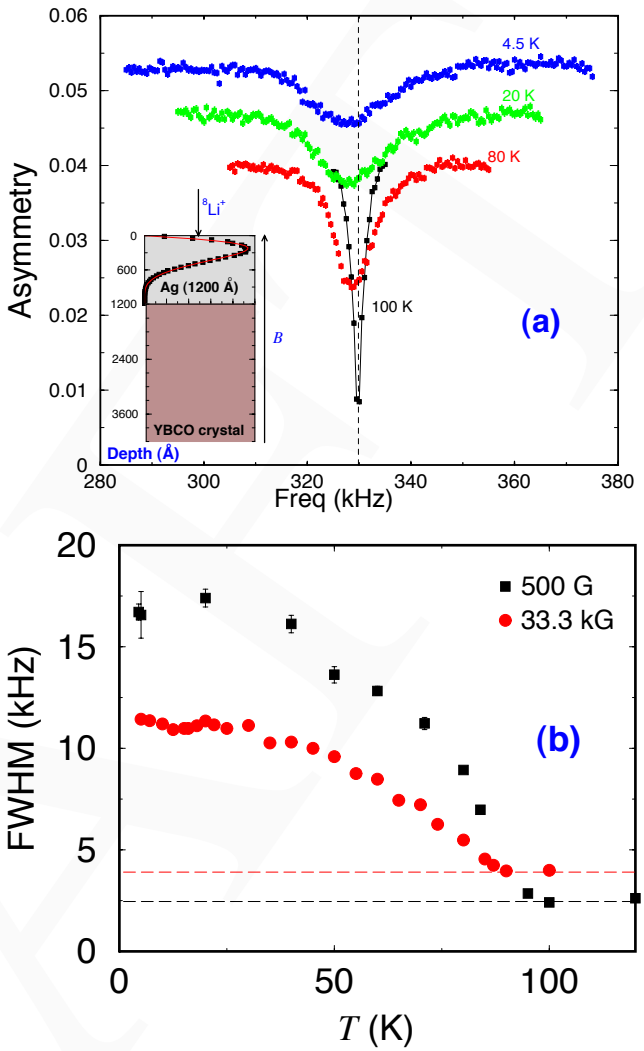


Fig. 2. (a) The $\beta$-NMR resonance in Ag/YBCO measured in a magnetic field $B_{ex}$ of 516.7 G applied along YBCO $c$-axis. Inset: the profile of $^8Li^+$ beam of 8 keV energy stopping into Ag simulated using TRIM code. (b) The temperature dependence of the FWHM extracted from Lorentzian fits of $\beta$-NMR data at 516 G and 33.3 kG.

### Experiment 1101
### $\mu$SR study of the spin singlet state in two-dimensional system $SrCu_2(BO_3)_2$

*(G.M. Luke, McMaster)*

Low-dimensional spin systems with spin-singlet ground states have attracted considerable study over the past 15 years. These systems are interesting for a number of reasons, including possible relevance to high temperature superconductivity and the existence of novel ground states. $SrCu_2(BO_3)_2$ is a quasi-two-dimensional spin system with a spin-singlet ground state. The unit cell is tetragonal and the structure is characterized by layers consisting of $Cu^{2+}$, $O^{2-}$ and $B^{3+}$ running perpendicular to the $c$-axis. These layers

are separated from each other by planes composed of $Sr^{2+}$ ions. All $Cu^{2+}$ sites have localized spin $S = 1/2$ moments and one nearest neighbour with which they form dimeric units, while each of these units is surrounded by four orthogonal dimers.

We grew single crystals of $SrCu_2(BO_3)_2$, $SrMg_{0.05}Cu_{1.95}(BO_3)_2$, $Sr_{0.96}La_{0.04}Cu_2(BO_3)_2$, and $Sr_{0.95}Na_{0.05}Cu_2(BO_3)_2$ in floating zone image furnaces at Tokyo and McMaster University following slightly different procedures. We then performed 5 T transverse field (TF) $\mu$SR measurements on the pure and doped $SrCu_2(BO_3)_2$ samples to investigate the presumed non-magnetic spin singlet ground states in these systems. The samples were mounted in a low-background apparatus with the $c$-axis parallel to the incoming muon momentum (and the external field). In this high field experiment, the measurements of the muon precession frequency signal in our samples and a reference material ($CaCO_3$) were taken simultaneously to allow for a precise determination of the frequency shift.

Implanted positive muons reside at sites which are minima in the electrostatic potential. Generally in oxides, muons are hydrogen-bonded to $O^{2-}$ ions, roughly 1 Å away. Figure 1 shows a fast Fourier transform of the transverse field muon precession signal measured in an applied magnetic field $B = 5$ T $\parallel \hat{c}$ at $T = 20$ K. Two peaks are clearly visible which correspond to two magnetically inequivalent muon sites in $SrCu_2(BO_3)_2$; we associate these with the two magnetically inequivalent oxygen sites in the system. To take these two muon sites into account, this 5 T TF data was fit to the following function:

$$\begin{aligned} P(t) &= A_1 \exp^{-\lambda_1 t} \cos(\omega_1 t + \phi_1) \\ &\quad + A_2 \exp^{-\lambda_2 t} \cos(\omega_2 t + \phi_2) \,. \end{aligned}$$

The frequency shift is the fractional difference between the applied field and the local field at the muon site, and it is proportional to the local spin susceptibility. We see that for one of the muon sites the frequency shift roughly follows a Curie-Weiss temperature dependence for $T > 4$ K (Fig. 2a), with the precise value of the Curie constant depending on the temperature range being fit. This is in contrast to $^{11}$B-NMR frequency shift measurements [Kodama *et al.*, J. Magn. Mag. Mat. **272-276**, 491 (2004)]. In that case, the authors applied a field of 7 T perpendicular to the [1 –1 0] direction and observed a decrease in the frequency shift below the singlet formation temperature of 15 K. The lack of a similar decrease in our $\mu^+$ frequency shift for this site indicates the presence of a larger local field than expected in the singlet regime. The fundamental difference between the two frequency shifts is that in our case there is a muon present in the system, which means the larger local field is likely the result of a muon perturbation effect. More specifically, it seems that the muon has locally broken a spin singlet bond and created at least two quasi-free spins. These spins are then polarized by the applied field which leads to our observed frequency shift. As this appears to be a strong effect, it then seems reasonable to associate this muon site with the oxygen site in the Cu-O-Cu superexchange path.

The shift at the other muon site is considerably smaller and negative (see inset of Fig. 2a). In this case, the frequency shift follows the temperature-dependence of the bulk susceptibility reasonably well, indicating the lack of any strong muon perturbation. For this reason, this site likely corresponds to the $O^{2-}$ ion out of the Cu-O-Cu superexchange path.

In the doped samples, three frequency peaks were observed in the FFTs instead of two as in the case of the pure sample. For this reason, the data were fit to the same functional form as before, but three exponentially-damped cosine terms were included instead of two. The frequency shifts calculated from this fit are given in Fig. 2b-d; the shifts for all three doped samples examined appear to be essentially equivalent. The upper and lower branches are remarkably similar to the two branches in the pure case, but the middle branch is new and so it seems is due to the dopants.

In one situation, we are substituting non-magnetic Mg in for the Cu sites. It is well known that this leads to the direct breaking of spin singlets, as some Cu spins no longer have a nearest neighbour Cu with which to form a dimer. In the other two cases, we are substituting La or Na in for the Sr sites. These are both forms of charge doping, with each La introducing one electron into our system and each Na introducing one hole. Each electron or hole introduced by doping is expected to break a singlet pair and make a localized spin-1/2. Resistivity measurements performed by Liu *et al.* on La and Na-doped polycrystalline samples verify the localized nature of these carriers. The breaking of singlets by the different dopants is supported by dc susceptibility measurements performed on our single crystals with an applied field $H = 1$ kG $\parallel$ ab plane. All three doped samples had much larger Curie tails than the pure sample, indicating the presence of many more free spin-1/2 Cus in the singlet regime. We have calculated the fraction of free spins from this data; the results are shown in Table I. In all the doped cases, the fraction of free spins is at least five times as great as in the pure case, but still lower than what we expect considering the concentration of our starting materials. This is likely due to difficulties involved in doping this system and suggests that our doping concentrations should be viewed as nominal values.

With these insights, it then appears there are three distinct possibilities for muons in the doped samples. The muon can stop at the sites either in or out of the superexchange path as before. If the muon stops at the site in the superexchange path, it will break the singlet and create two quasi-free spins in close proximity. However, in some cases the singlet will already be broken due to the dopants and then the muon will have no singlet to break. In this case, the muon will only be in close proximity to one quasi-free spin and so a smaller frequency shift will be measured with decreasing temperature, giving us the middle branch. In fact, Fig. 2b-d shows that this middle branch gives about half the shift of the upper branch.

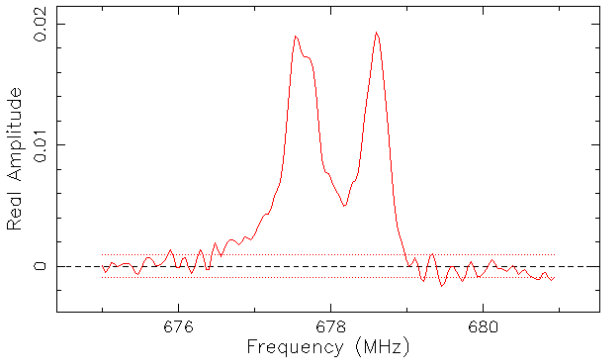


Fig. 1. Fast Fourier transform of precession signal for $SrCu_2(BO_3)_2$ measured in an external magnetic field $B = 5$ T $\parallel \hat{c}$ at 20 K. The two peaks correspond to two magnetically inequivalent muon sites.

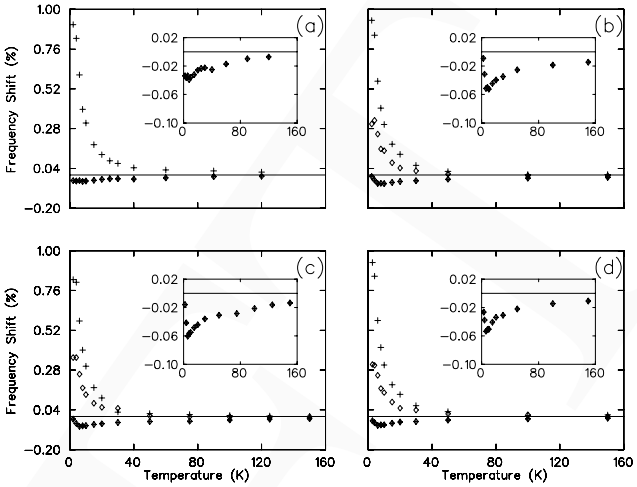


Fig. 2. Frequency shifts vs. temperature measured in an applied field of 5 T for: (a) $SrCu_2(BO_3)_2$, (b) $Sr_{0.96}La_{0.04}Cu_2(BO_3)_2$, (c) $SrMg_{0.05}Cu_{1.95}(BO_3)_2$, and (d) $Sr_{0.95}Na_{0.05}Cu_2(BO_3)_2$. The insets show the temperature dependence of the frequency shift for the muon site outside of the superexchange path.

Table I. Estimated fraction of free spin 1/2-Cus by fitting susceptibility data with $H = 1$ kG $\parallel$ ab plane.

| Sample | Fraction of Cu free spins |
|---|---|
| $SrCu_2(BO_3)_2$ | 0.06 |
| $SrMg_{0.05}Cu_{1.95}(BO_3)_2$ | 0.95 |
| $Sr_{0.96}La_{0.04}Cu_2(BO_3)_2$ | 0.53 |
| $Sr_{0.95}Na_{0.05}Cu_2(BO_3)_2$ | 0.29 |